Numerical and Theoretical Studies of Physics Beyond the Standard Model

Ulrik Ishøj Søndergaard

August 1, 2013

Centre for Cosmology and Particle Physics Phenomenology (CP³-Origins),

Department of Physics, Chemistry and Pharmacy (FKF),

University of Southern Denmark (SDU)
Campusvej 55
DK-5230 Odense M

Supervisor: Francesco Sannino
Co-supervisor: Claudio Pica

A dissertation submitted to the University of Southern Denmark for the degree of Doctor of Philosophy

Publications

U. I. Sondergaard, C. Pica, and F. Sannino, "S-parameter at Non-Zero Temperature and Chemical Potential," *Phys.Rev.*, vol. D84, p. 075022, 2011.

A. Hietanen, C. Pica, F. Sannino, and U. I. Sondergaard, “Orthogonal Technicolor with Isotriplet Dark Matter on the Lattice,” *Phys.Rev.*, vol. D87, p. 034508, 2013.

Copies of the publications are included in the end of this thesis.

Abstract

The Standard Model of particle interactions triumphed when the discovery of the Higgs boson was announced by the CMS and ATLAS collaboration at the Large Hadron Collider July 4th, 2012. The Standard Model has been very successful, but has limitations as well as some aesthetic problems. Many of these problems are related to the Higgs field. By replacing the Higgs sector of the Standard Model with a new strongly coupled sector some of these problems can be solved. These new strong interactions are referred to as Technicolor interactions.

In this thesis we present results from lattice studies of two concrete Technicolor models, the SO(4) fundamental Minimal Walking Technicolor (MWT) model and the SU(3) sextet MWT. After motivating this type of models by discussing some experimental constraints, we present results from our numerical investigations of their spectra. Our results disfavor the existence of an infrared fixed point in either model.

This thesis also contain a presentation of our attempt to accelerate Monte Carlo simulations of lattice gauge theories, by performing the calculations on graphics processing units (GPUs). We discuss several optimizations and test the performance using as test cases SU(2) gauge theories with Wilson fermions transforming in the fundamental and adjoint representation.

Resumé

Partikelfysikkens Standardmodel triumferede da opdagelsen af Higgs bosonen blev annonceret af CMS og ATLAS sammenslutningerne ved Large Hadron Collider den 4. juli 2012. Standardmodellen har været meget succesful, men har sine begrænsninger og skønhedsfejl. Mange af disse problemer er relateret til Higgsfeltet. Ved at erstatte Standardmodellens Higgssektor med en ny stærkt vekselvirkende sektor kan nogle af disse problemer løses. Disse nye stærke vekselvirkninger kaldes Technicolor interaktioner.

I denne afhandling præsenterer vi resultater fra studier af to konkrete Technicolor modeller formuleret på et gitter: SO(4) fundamental Minimal Walking Technicolor (MWT) modellen og SU(3) sekstet MWT modellen. Efter at motivere modeller af denne type ved at diskutere nogle eksperimentelt fastsatte begrænsninger, præsenterer vi resultater fra vores numeriske undersøgelser af deres spektre. Vores resultater antyder, at spontant, globalt symmetribrud finder sted i begge modeller.

Denne afhandling indeholder også en præsentation af vores forsøg på at accelerere Monte Carlo simuleringer af gitterfeltteorier ved at udføre beregninger på grafikprocessorer (GPU'er). Vi diskuterer forskellige optimeringer og tester ydelse på en SU(2)-model med Wilson fermioner i den fundamentale og adjungerede repræsentation af gaugegruppen.

Preface

The work presented in this thesis has bene done primarily at the Centre for Cosmology and Particle Physics Phenomenology (CP^3-Origins). I have been around the center since its establishment by the Danish National Research Foundation in 2009. I have seen how CP^3-Origins has developed into an extraordinarily dynamic research center under the direction of my supervisor Francesco Sannino. The energetic environment provided by CP^3-Origins has attracted many bright students and strong researchers to come to University of Southern Denmark. This includes my co-supervisor Claudio Pica who made CP^3-Origins an attractive place to study and research gauge theories on the lattice. I would like to thank both Francesco Sannino and Claudio Pica for providing great advise and inspiring discussions.

All the staff and students at CP^3-Origins have contributed to the inspiring atmosphere. Lately I have had many interesting discussions with Ari Hietanen and for that I am thankful.

Finally, I would like to direct my love and gratitude to my wife Sara and my daughter Liv for their love and patience.

Ulrik Ishøj Søndergaard

Contents

Contents **5**

1 Introduction **9**

1.1 A new strong sector 10

Minimal Walking Technicolor models 14

2 Gauge Theories on a Lattice **15**

2.1 Path Integral Representation of Fermionic Matter 15

2.2 Gauge Interactions 16

2.3 Lattice formulation 17

3 Approaching physics from the lattice **19**

3.1 Mass shifts from finite size 20

3.2 Continuum limit 22

3.3 Chiral limit 22

Hyperscaling in mass deformed conformal gauge theories 23

4 GPU accelerated Hybrid Monto Carlo algorithm **24**

4.1 Inversion of the fermion matrix 24

Even-odd preconditioning 25

4.2 Quasi-Minimal Residual algorithm 27

Breakdown of the QMR algorithm 28

Minimizing the Quasi-Residual 29

4.3 Mixed Precision Solvers 30

4.4 GPU implementation and optimization 31

Spinor linear algebra . . . 31
Coalesced memory access . . . 32
Packing the gauge links . . . 33
SU(2) gauge links . . . 33
On-the-fly construction of represented gauge links . . . 33
Reduction of spilling . . . 34
4.5 Performance of SU(2) lattice gauge theories on GPU . . . 35
4.6 Summary and outlook . . . 39

5 SO(4) Fundamental Minimal Walking Technicolor with Wilson fermions 40
5.1 Introduction . . . 40
5.2 Chiral symmetry breaking pattern . . . 40
Baryonic diquarks . . . 42
Mesons . . . 42
Phenomenology of the scalar diquarks . . . 43
5.3 Perturbative estimates of the SO(N) conformal window . . . 44
5.4 Delineation of the lattice phase diagram . . . 46
5.5 The spectrum of SO(4) MWT . . . 47
Numerical simulations . . . 47
Results at fixed lattice spacing . . . 49
5.6 Finite size effects . . . 53
Domain walls . . . 55

6 SU(3) Sextet Minimal Walking Technicolor with Wilson fermions 59
6.1 Strong coupling expansion . . . 59
Motivation . . . 59
Introduction . . . 60
Character expansion . . . 60
The partition function to $\mathcal{O}\left((\beta/6)^{10}\right)$ . . . 62
Plaquette expectation value to $\mathcal{O}\left((\beta/6)^{4}\right)$ . . . 63
6.2 Hopping parameter expansion . . . 64
6.3 Plaquette expectation value in SCE and HPE . . . 66
6.4 Bulk phase and delineation of the lattice phase diagram . . . 67
6.5 The spectrum of SU(3) sextet technicolor . . . 70

Numerical simulations 71
Results 71
Finite size effects 76
Chiral limit 77
Continuum extrapolation 81

7 Summary and outlook 83

Appendix A Construction of hadrons in SO(4) 85

Vector mesons and baryons 86

Bibliography 88

Notation, conventions and abbreviations

In this thesis all results and calculations are performed in natural units

$$\hbar = 1 = c\,.$$

Similarly,when presenting results from lattice calculations it will always be in units of lattice spacing a such that the correct dimensions are recovered.

ABBREVIATIONS

BSM Beyond Standard Model

ChPT Chiral Perturbation Theory

ETC Extended Technicolor

FCNC Flavor Changing Neutral Current

HPE Hopping Parameter Expansion

SCE Strong Coupling Expansion

SM Standard Model

TC Technicolor

WChPT Wilson Chiral Perturbation Theory

Introduction

1

The Standard Model(SM) of particle interactions is very successful in describing almost all observations in the realm of particle physics. The model is guided by the gauge principle which means that interaction terms are forced by making certain symmetries local. One example is the symmetry between the quarks of different color. The localization of this symmetry forces the 8 gluons in the theory along with the interactions among quarks and gluons. This sector of the standard model is referred to as the Strong Interactions and is described by Quantum Chrome Dynamics(QCD).

Even though the gauge principle has served as a guide to the construction of the Standard Model, not all interaction terms are derived from this. This has to do with the Higgs field, which is a special ingredient in the SM since it is a scalar field. All remaining fields, the quarks, leptons and neutrinos are all fermions. The existence of a scalar field allows for the existence of renormalizable interactions of Yukawa type. That is, interactions between the Higgs field and two fermionic fields. All the matter fields are listed in table 1. The gauge principle does not demand the Yukawa interactions, but they are there nonetheless. This poses a problem of aesthetic nature[1]. Especially since the Yukawa interactions adds to the SM a large number of independent numerical constants distributed over several orders of magnitude.

Another problem of aesthetic character also arises as a consequence of a scalar field in the Standard Model. The Higgs mass receive severe quantum corrections and develops power low dependence on the scale at which new physics occur. Now, if no new physics where to be expected then this would not be a problem. However, gravity provides a universal regulator, the Planck scale $\Lambda \sim 10^{19}$ GeV.

Already it seems that the scalar Higgs field is stirring up a bit of trouble. And it does not end here. Perturbative renormalization tells us that the Higgs quartic coupling becomes negative

---

[1] Aesthetics is matter of opinion. Here, the only opinion taken into account is that of the author

at very high scales. If we were to trust this all the way to the Planck scale we would conclude that the Universe is in a metastable state[1, 2, 3].

Of course the Higgs has a role to play. It is needed in order too give mass to the Standard Model particles. In particular to the Z and the W bosons, but also the quarks and leptons. In total, three massless degrees of freedom are needed to provide the longitudinal components of the massive gauge bosons. An additional degree of freedom must acquire a vacuum expectation value in order to provide a mass scale.

A simpler, but very similar picture, is the Ginzburg-Landau model of superconductivity. In superconductivety we deal only with one gauge boson, the photon, and it is given a mass by a complex scalar field. In this case the angular part of the field provides the longitudinal photon component and the radial part acquires an expectation value. This is the spontaneous breakdown of the U(1) gauge symmetry of electromagnetism.

In the Higgs sector of the standard model, the symmetry breaking pattern is different. The weak and hypercharge gauge group $\mathrm{SU}(2)_\mathrm{L} \otimes \mathrm{U}(1)_\mathrm{Y}$ is broken to the electromagnetic $\mathrm{U}(1)_\mathrm{EM}$. The initial symmetry had 3+1 generators whereas the $\mathrm{U}(1)_\mathrm{EM}$ only has one. According to to the Goldstone theorem[4] this gives rise to exactly the three massless degrees of freedom needed for the longitudinal components of the Z and W bosons. The Higgs vacuum expectation value $v = 246$ GeV provides the mass scale.

1.1 A NEW STRONG SECTOR

In this section we will briefly describe how a new strong sector, referred to as Technicolor, can replace the fundamental Higgs. A Higgsless Standard Model would in fact break electroweak symmetry by the formation of a quark condensate $\langle \bar{q} q \rangle \neq 0$ mediated by Strong interactions. The associated Nambu-Goldstone bosons[4, 5], the *pions*, would provide the longitudinal components of the W's and Z. The masses of the W and Z would be proportional to the pion decay

Name	Symbol	$\mathrm{U}(1)_\mathrm{Y}$	$\mathrm{SU}(2)_\mathrm{L}$	$\mathrm{SU}(3)_\mathrm{S}$	Spin
3× Left handed quarks	$q_\mathrm{L} = (u_\mathrm{L}\ d_\mathrm{L})$	$\frac{1}{6}$	□	□	$\frac{1}{2}$
3× Right handed up-type quarks	u_R	$\frac{2}{3}$	1	□	$\frac{1}{2}$
3× Right handed down-type quarks	d_R	$-\frac{1}{3}$	1	□	$\frac{1}{2}$
3× Left handed leptons	$l_\mathrm{L} = (e_\mathrm{L}\ \nu_\mathrm{L})$	$-\frac{1}{2}$	□	1	$\frac{1}{2}$
3× Right handed leptons	e_R	-1	1	1	$\frac{1}{2}$
1× Higgs	H	$\frac{1}{2}$	□	1	0

Table 1: Standard Model matter field content

constant f_π. In fact it would replace the vacuum expectation value of the Higgs field in the expression for the mass

$$M_{\mathrm{W\,or\,Z}} \sim g v \to g f_\pi \,, \tag{1.1}$$

where g is the weak gauge coupling. The problem with this picture is that $f_\pi \simeq 93$ MeV whereas $v \simeq 246$ GeV so the Z and W's would be much too light. Early versions of Technicolor[6, 7] was therefore to a certain extend scaled up versions of QCD. This picture has changed today.

In the 1970's, when Technicolor(TC) was developed, the top quark had not been discovered yet and was not expected to be nearly as heavy as it turned out to be. Technicolor was therefore not intended to give mass to fermions. Today the framework in which the origin of fermion masses is explained is called *Extended* Technicolor (ETC). The ETC interactions couples to both ordinary SM fermions and to techniquarks. The ETC gauge group is supposed to break down to the ordinary Technicolor group at some scale Λ_{ETC}. The SM fermion mass terms in a low energy effective theory will be non-renormalizable four fermion operators suppressed by Λ^2_{ETC}.

$$m_{\text{SM fermion}} \sim g^2_{\mathrm{ETC}} \frac{\langle \bar{q}_{\mathrm{TC}} q_{\mathrm{TC}} \rangle |_{\Lambda_{\mathrm{ETC}}}}{\Lambda^2_{\mathrm{ETC}}} \,. \tag{1.2}$$

$\langle \bar{q}_{\mathrm{TC}} q_{\mathrm{TC}} \rangle |_{\Lambda_{\mathrm{ETC}}}$ is the technifermion condensate evaluated at the ETC scale. At this point Technicolor is facing a problem. Four fermion interactions involving only SM fermions will also appear with same appearant suppression by the ETC scale. This will give rise to flavor changing neutral currents (FCNC) which are highly constrained experimentally[8]. This means that the ETC scale must be $\sim 10^3$ TeV or higher. If Technicolor is simply a scaled up version of QCD, the Top quark would be too light due to the Λ^2_{ETC} suppression.

This led to the idea of Walking Technicolor[9, 10] models in which the dynamics is not QCD-like, but rather quasi conformal. This means that the coupling runs very slowly, i.e. *walks*, between the TC scale and the ETC scale. The techniquark condensate would then be power law enhanced by renormalization effects between the TC and the ETC scale

$$\langle \bar{q}_{\mathrm{TC}} q_{\mathrm{TC}} \rangle |_{\Lambda_{\mathrm{ETC}}} = \langle \bar{q}_{\mathrm{TC}} q_{\mathrm{ETC}} \rangle |_{\Lambda_{\mathrm{TC}}} \left(\frac{\Lambda_{\mathrm{ETC}}}{\Lambda_{\mathrm{TC}}} \right)^{\gamma^*} \,. \tag{1.3}$$

γ^* is the anomalous dimension of the fixed point governing the dynamics in the walking region. That is, the fixed point at the critical number of flavors N^*_{f} where the model develops an infrared fixed point. The flavor content of the walking model will be slightly lower[2] but the dynamics in the walking region is assumed to resemble that of the nearby fixed point.

---

[2] Actually the pure Technicolor model might be conformal, but driven away from conformality by ETC induced four fermion interactions. This is referred to as *ideal walking*[11].

This is different from QCD-like theories where the condensate enhancement is only logarithmic.

We have now seen how Technicolor has adapted to survive the constraints on FCNCs. Another assassination attempt on the Technicolor idea came from electroweak precision constraints. Experiments like LEP I, LEP II, LHC and Tevatron can measure electroweak precision parameters and infer stringent and somewhat model independent constraints on new physics. This discussion can be rather lengthy, but we will only touch briefly on the subject to motivate the choice of models that we study.

In the above mentioned collider experiments, the external fermions are light compared to the Z mass. As a consequence the $q^\mu q^\nu$ part of the propagators are suppressed in processes involving the electroweak gauge bosons. This means in turn that direct corrections from beyond the Standard Model (BSM) are suppressed. In other words the so called *oblique corrections* will be the dominating effect from new physics. Oblique corrections are electroweak gauge boson vacuum polarization effects. A classic review is the one by Peskin and Takeuchi[12] and some original work on the subject is [13, 14, 15]. There are many ways for experiments to estimate, or rather constrain, the size of the oblique BSM corrections.

Consider the weak mixing angle θ_w. At tree level this is simply determined by the the ratio between the Z and the W masses.

$$\cos^2\theta_{\rm W} = \frac{M_{\rm W}^2}{M_{\rm Z}^2} = 0.2233 \qquad \text{(def. 1)}. \tag{1.4}$$

In fact we could promote this relation to be the *defining* relation of the renormalized mixing angle. This is referred to as the on shell scheme. However there are equally good definitions. For instance

$$\sin 2\theta_w = \sqrt{\frac{4\pi\alpha_{\rm SM^*}(M_{\rm Z}^2)}{\sqrt{2}G_{\rm F}M_{\rm Z}^2}} \qquad \text{(def. 2)}. \tag{1.5}$$

where $\alpha_{\rm SM^*}(M_{\rm Z}^2)$ is the fine structure constant calculated at the $M_{\rm Z}$ scale from SM contributions to the running. $G_{\rm F}$ is the Fermi constant which can be measured very precisely from muon lifetime.

Several other definitions could be chosen. Had we known all the the relevant corrections to these quantities we could calculate one from the other and the weak mixing angle would be highly overdetermined. This is exactly the point. The discrepancy between various determinations of this quantity tells us something about the size of the corrections we do not know. In this way we can parametrize our ignorance of the BSM corrections. For instance, the difference between the two definitions above gives

$$\cos^2\theta_{\mathrm{W}}^{\mathrm{def\,1}} - \cos^2\theta_{\mathrm{W}}^{\mathrm{def\,2}} = \frac{\alpha c^2}{c^2 - s^2}\Bigg[-\frac{1}{2}\underbrace{16\pi\Big(\Pi'_{33}(0) - \Pi'_{3Q}(0)\Big)}_{\equiv S} + c^2\underbrace{\frac{4\pi}{s^2c^2M_Z^2}\big(\Pi_{33}(0) - \Pi_{3Q}(0)\big)}_{\equiv T} \\ + \frac{c^2 - s^2}{4s^2}\underbrace{16\pi\big(\Pi'_{11}(0) - \Pi'_{33}(0)\big)}_{\equiv U}\Bigg], \tag{1.6}$$

where $c \equiv \cos\theta_{\mathrm{W}}$, $s \equiv \sin\theta_{\mathrm{W}}$ and $\Pi_{XY}(q^2)$ is the coefficient in front of the metric in the vacuum polarization amplitude $\Pi^{\mu\nu}_{XY}(q^2) = \Pi_{XY}(q^2)g^{\mu\nu} + \Delta_{XY}(q^2)\frac{q^\mu q^\nu}{q^2}$. The X, Y takes values $1, 2, 3, Q$ where $1, 2, 3$ relates to the generators of $\mathrm{SU_L}(2)$ and Q to the generator of a linear combination of '3' and hypercharge. S, T and U are the Peskin-Takeuchi parameters. They are all finite and they provide a parametrization of the oblique SM and BSM effects on electroweak precision observables. The SM contributions to S, T and U can be calculated leaving the unknown BSM corrections as parameters which are then experimentally constrained. Note that the Peskin-Takeuchi parametrization is not unique.

The S parameter is particularly sensitive to Technicolor extensions of the Standard Model. The Gfitter project[16] provides a global analysis of the electroweak precision constraints on S, T and U. They find that an S parameter above ~ 0.3 is incompatible with data regardless of the value of the T parameter. The U parameter is not very sensitive to new physics and is projected away in this analysis. The T parameter is a measure of isospin violation and since isospin symmetry is broken in the Standard Model a complete ETC theory must violate isospin and therefore give contributions to the T parameter. In this thesis ETC models will not be discussed, but the bound on $S \lesssim 0.3$ will be present nonetheless. This bound on the S parameter is to be interpreted as the difference upon *replacing* the Higgs sector with a Technicolor sector. Thus we need to subtract the Higgs contribution before adding the TC contribution. We refer to a recent paper [17] for a detailed discussion of this issue. To get an intuition about the interpretation of the S parameter we can have a look at the result in perturbation theory. A 1-loop evaluation was done by Peskin and Takeuchi in [14]

$$S_{\text{1-loop}} = \frac{N_{\mathrm{f}}d[r]}{12\pi}, \tag{1.7}$$

where $d[r]$ is the dimension of the representation of the gauge group under which N_{f} degenerate fermions transform. Note that the definition used here uses the zero external momentum limit when evaluating the vacuum polarization amplitudes. In other papers[18, 19, 20] the external momentum is kept as a parameter. This computation can not be trusted outside the

Bank-Zaks regime with an infrared fixed point at small coupling. However, this naive computation suggests an interpretation of the S parameter as a measure of the size of the TC sector. Consequently when picking candidate technicolor models, one should choose so called *minimal* models. That is, models with a minimal choice of technicolor charged matter. We can use the 1-loop calculation (1.7) as a naive guide in our choice of models, but a full non-perturbative calculation of the S parameter is required once the models have been selected. Such non-perturbative evaluations in lattice gauge theories have been performed by Boyle et al.[21], DeGrand[22] and the LSD collaboration[23].

On the lattice, many different scales are present and it is important to evaluate the S parameter in the correct regime. For instance, the computation will necessarily be performed at finite external momentum, but also temperature will enter the problem. In [20] we have suggested a suitable generalization of the definition of the S parameter and evaluated it in perturbation theory.

Minimal Walking Technicolor models

We have now discussed how we should pick candidate technicolor models. This can be summarized very briefly

Minimal Our models should have a minimal amount of TC matter to survive constraints from electroweak precision measurements.

Walking Our models must have walking dynamics in order to explain the top quark mass while not violating the experimental bounds on flavor changing neutral currents.

Appearantly, these two ideas is at some tension with one another, since more TC fermion flavors are needed to get close to an IR fixed point and walking dynamics. To meet both demands, models with fermion matter in higher representations of the technicolor gauge group is an attractive option[24]. In this thesis we will present non-perturbative lattice studies of two models of Minimal Walking Technicolor (MWT). The SO(4) fundamental MWT and the SU(3) sextet MWT. Both models have two technifermion flavors.

Before discussing our findings in chapter 5 and 6 we will briefly introduce the lattice action (chapter 2) and how findings in a lattice gauge theory can be related to the physical system (chapter 3). In chapter 4 a more technical presentation is given of how graphics processing units (GPUs) can be used to accelerate lattice simulations. Finally, in chapter 7 we summarize and discuss future perspectives.

Gauge Theories on a Lattice

2

A thorough introduction to the euclideanized path integral and various discretisation techniques can be found in many good textbooks like [25, 26]. To exhaust this subject is beyond the scope of this report. We will however summarize very briefly the formulation of fermions on a spacetime lattice.

2.1 PATH INTEGRAL REPRESENTATION OF FERMIONIC MATTER

Disregarding the 125 GeV Higgs resonance observed at the LHC[27, 28] , which might or might not be a fundamental object, all elementary matter fields observed in nature are fermionic. The models analysed in our work are those of technicolor interacting fermionic matter, so we can deploy techniques which have been developed for the analysis of QCD. The generating functional of the Greens functions, i.e. the path integral, will involve integration over anticommuting fields.

$$\{\psi_a, \psi_b\} = 0\,, \tag{2.1}$$

where a and b indexes the fermionic degrees of freedom. They could for instance represent flavors. (2.1) is the Grassman algebra. The Grassman algebra makes integration quite trivial since power series of functions over Grassman variables will terminate at first order. The only integration rules needed are therefore

$$\int d\psi = 0 \qquad \text{and} \qquad \int d\psi\psi = 1\,. \tag{2.2}$$

The integration measure $d\psi$ is to be regarded as a Grassman variable as well. As a consequence the generic Gaussian integral can be written as

$$\int d\chi_1 \cdot \ldots \cdot d\chi_N d\psi_1 \cdot \ldots \cdot d\psi_N e^{-\chi_a M_{ab} \psi_b} = \det M\,, \tag{2.3}$$

where χ_a and ψ_a, $a = 1,...,N$ are Grassman variables. Note that the corresponding bosonic gaussian integral is

$$\int d\phi_1 \cdot ... \cdot d\phi_N e^{-\frac{1}{2}\phi_i M_{ij}\phi_j} = \frac{(2\pi)^{N/2}}{\sqrt{\det M}}. \tag{2.4}$$

Indeed, the generating functional for the fermionic techni quark degrees of freedom will be of gaussian type. We can evaluate the correlation functions through integrals of the type

$$\int D\chi D\psi \prod_i^L \psi_{a_i} \prod_j^L \chi_{a_j} e^{-\chi_a M_{ab}\psi_b}, \tag{2.5}$$

where $D\psi$ is shorthand for $d\psi_1 \cdot ... \cdot d\psi_N$. The products involve some subset of the Grassman variables. The integral can be reexpressed as

$$(-1)^{L(L-1)/2} \det M \sum_{\{P\}} (-1)^{\sigma_P} \prod_{i,j}^L \left(M^{-1}\right)_{a_i b_{P_j}}. \tag{2.6}$$

σ_P is the sign associated with the permutation P arising when commuting the Grassman variables. The actual correlation functions are normalised by $Z = \int D\chi D\psi e^{-\chi_a M_{ab}\psi_b} = \det M$. In particular

$$\langle \psi_a \chi_b \rangle = \frac{\int D\chi D\psi \prod_i^L \psi_{a_i} \prod_j^L \chi_{a_j} e^{-\chi_a M_{ab}\psi_b}}{\int D\chi D\psi e^{-\chi_a M_{ab}\psi_b}} = \left(M^{-1}\right)_{ab}. \tag{2.7}$$

This is all we need to know about generating functionals of fermionic variables. We can now write down the fermion action explicitly and introduce gauge interactions.

2.2 GAUGE INTERACTIONS

The continuum action of interest to us have the form

$$S = -\int d^4x \left(\frac{1}{4g^2} \mathrm{Tr}\, F^{\mu\nu} F_{\mu\nu} - \bar{q}(i\not{D} - m)q \right). \tag{2.8}$$

where

$$F_a^{\mu\nu} = \partial^\mu A_a^\nu - \partial^\nu A_a^\mu + g f_{abc} A_b^\mu A_c^\nu, \tag{2.9}$$

is the field strength tensor of the (techni) gluon field and f_{abc} is the structure constants of the Gauge group. $\not{D}$ is the covariant derivative contracted with the Dirac γ matrices

$$\not{D} = \gamma^\mu (\partial_\mu + i g A_\mu^i \tau_{\mathrm{R}}^i), \tag{2.10}$$

where τ_{R}^i, $i = 1,...,d[G]$ is the generators of representation R of the gauge group. The Minkowski space path integral is

$$Z = \int DAD\bar{q}Dq e^{iS}. \tag{2.11}$$

Source terms can be added for the gluonic and both fermionic fields in order to use Z as a generating functional. At this point we define a corresponding field theory living in euclidean space-time by making the substitution $(x_0 \to -ix_0,\, A_0 \to iA_0)$. This implies that

$$\int d^4x \,\mathrm{Tr}\, F^{\mu\nu}F_{\mu\nu} \to i\int d^4x \,\mathrm{Tr}\, F^{\mu\nu}F_{\mu\nu}\,, \tag{2.12}$$

$$\int d^4x \bar{q}(i\not{D} - m)q \to -i\int d^4x \bar{q}(\not{D} + m)q\,, \tag{2.13}$$

and we can define the euclidean action as

$$S_{\mathrm{E}} = \int d^4x \left(\frac{1}{4g^2}\,\mathrm{Tr}\, F^{\mu\nu}F_{\mu\nu} + \bar{q}(\not{D} + m)q\right). \tag{2.14}$$

such that $S = iS_{\mathrm{E}}$ and $Z = \int DAD\bar{q}Dqe^{-S_{\mathrm{E}}}$. We notice that we could formally integrate out the fermion fields using the Grassman gaussian integral formula (2.3), but before doing that we will briefly discuss the discretisation of the action to a hypercubic space-time lattice.

2.3 LATTICE FORMULATION

There are many discretisation strategies, but in our work we have used the Wilson prescription exclusively.

The Wilson lattice action is

$$S_{\mathrm{E,L}} = \sum_{j,x,y} \bar{q}(x)D(U,x,y)q(y) + \beta\sum_{\Box}\left[1 - \frac{1}{N_{\mathrm{c}}}\mathrm{Tr}U_{\Box}\right]. \tag{2.15}$$

$D(U,x,y)$ is the Wilson-Dirac matrix which is a particular choice of discretization of the Dirac operator + the fermion mass term. $U_{\Box}$ is the plaquette operator constructed from the product of four matrices $U_\mu(x)$ associated with the links between adjacent lattice sites. $U_\mu(x)$ has the interpretation as the parallel transport of the gauge field from site x to the μ-neighbour site.

$$U_\mu(x) = \exp\left(ig\int_x^{x+a\hat{\mu}} dz_\mu A_\mu(x)\right) \tag{2.16}$$

We note that in the continuum limit, that is $a \to 0$ we recover the continuum (euclidean) action

$$S_{\mathrm{E,L}} \xrightarrow{\text{Continuum}} \int d^4x \left(\frac{1}{4g^2}F^{\mu\nu}F_{\mu\nu} + \bar{q}(\not{D} + m)q\right). \tag{2.17}$$

When formulating the fermion action on the lattice there will always be some compromise involved. The Nielsen-Ninomiya theorem[29] tells us that it is impossible, on a lattice, to formulate a chirally and translationally symmetric, real bilinear fermion action which is local and *doubler*-free. Doublers are extra fermion degrees of freedom arising in the continuum limit of a naively discretized fermion action.

What we are looking for is exactly a lattice action with the above mentioned properties, but since this is not possible we must settle for a compromise. When using Wilson fermions we have sacrificed chiral symmetry. Therefore, putting the bare fermion mass term to zero in the action will not correspond to zero physical quark mass. The Wilson prescription introduces additive renormalization, which must be compensated by shifting the bare quark mass to a negative value. For each value of the coupling β there is a critical bare mass $m_{\mathrm{C}} < 0$ which exactly cancels the additive renormalization. This critical mass can be estimated in perturbation theory[30], but it is necessary to do a scan in the bare mass m_0 calculating the physical quark mass in order to get the correct non-perturbative value. The Wilson prescription has the advantage that it is fairly simple to implement and the fact that it is strictly local makes it numerically *light*.

3

Approaching physics from the lattice

It is in the nature of the lattice approach that simulations are performed at:

1. Finite volume.
2. Non-zero lattice spacing.
3. Non-zero quark mass.

All of which are aspects in which the simulated system differ from the physical system we ultimately aim to study. These issues has of course been given a lot of attention through the years, but since we are using Wilson fermions a relevant discussion is [31]. The non-zero quark mass is actually a true feature of QCD, so in lattice QCD only the lattice spacing and finite volume differ from the physical system. However, due to limited computing resources, for many years it has not been possible to simulate quarks as light as the Up and Down. Studying lattice technicolor, we are interested in the zero quark mass limit.

In this chapter, the discussion will be directed towards spectrum calculations in the chirally broken phase. Usually, when computing the spectrum, the volume is chosen to be *large enough* while extrapolations are used in order to probe the continuum (zero lattice spacing) limit as well as the chiral (zero quark mass) limit. The volume is large enough if the hadron fits inside the system along with the associated cloud of virtual particles. Often this requirement is rephrased in terms of the Compton wavelength $\lambda = 1/m_{\text{Hadron}}$ by demanding the linear extent L of the system to be much greater than the Compton wavelength of the pion.

Another concern regarding the finite extent of the lattice is that the system can undergo a deconfinement phase transition if L is decreased below the quark confinement length scale.

This can be observed through the breaking of center symmetry via the Polyakov loop observable. In this chapter we will assume our system to be in the confining phase.

3.1 MASS SHIFTS FROM FINITE SIZE

In the following it is assumed that our lattice has dimensions $L^3 \times T$ in lattice units where T is the temporal extent and is assumed to be large. Periodic boundary conditions are imposed. A central formula for the mass shift of hadronic states in a quantum field theory was derived by Lüscher [32] in 1986. In his paper he remarks that finite size effects are quite insensitive to the ultraviolet regulator.

Let $m_i(L)$ denote the mass of particle i at lattice size L. The mass shift is defined as

$$\Delta m_i(L) = m_i(L) - m_i\,, \quad \text{where} \quad m_i = \lim_{R\to\infty} m_i(R)\,. \tag{3.1}$$

We will describe the approach of $m_i(L)$ to m_i in the $L \to \infty$ limit keeping all other (bare) parameters fixed. The formula derived by in [32] holds to all orders in perturbation theory and possibly also beyond. In [32] scalar field theories with a mass gap is considered. This can be seen as an effective theory for the mesons.

The euclidean propagator has the form

$$\langle \phi(x)\phi(0)\rangle = \int \frac{d^4p}{(2\pi)^4} e^{ipx} G(p)\,, \tag{3.2}$$

where

$$G(p)^{-1} = p^2 + m^2 - \Sigma(p)\,. \tag{3.3}$$

At the mass pole $p^2 = -m^2$ the normalization of ϕ is chosen such that $\Sigma(p) = 0 = \frac{\partial}{\partial p^\mu}\Sigma(p)$. At finite volume (keeping the temporal dimension infinite) the momentum integral becomes a momentum sum

$$\int \frac{d^4p}{(2\pi)^4} \longrightarrow L^{-3} \sum_{\mathbf{p}} \int \frac{dp^0}{2\pi}\,, \tag{3.4}$$

where $\mathbf{p} = \frac{2\pi}{L}\mathbf{n}$, $\mathbf{n} \in \mathbb{Z}^3$. Also the irreducible self energy will be different at finite volume

$$\Sigma(p) \longrightarrow \Sigma_L(p)\,. \tag{3.5}$$

If we are at large L the mass shift Δm will be small, and we can expand the pole equation in this value

$$G_L(im(L), \mathbf{0})^{-1} = 0 = -2m\Delta m(L) - \Sigma_L(\hat{p}) - i\frac{\partial}{\partial p^0}\Sigma_L(\hat{p})\Delta m(L) + \mathcal{O}\left(\Delta m(L)^2\right)\,, \tag{3.6}$$

giving the expression

$$\Delta m(L) = -\frac{\Sigma_L(\hat{p})}{2m + i\frac{\partial}{\partial p^0}\Sigma_L(\hat{p})} + \mathcal{O}\left(\Delta m(L)^2\right), \tag{3.7}$$

where $\hat{p} = (im, \mathbf{0})$ is the infinite volume pole. We expect that the difference between $\Sigma_L(\hat{p})$ and $\Sigma(\hat{p})$ is small. In fact it can be shown that to any order in perturbation theory

$$\Sigma_L(\hat{p}) - \Sigma(\hat{p}) = \mathcal{O}\left(e^{-\sqrt{3}m/2}\right), \tag{3.8}$$

$$\frac{\partial}{\partial p^0}\Sigma_L(\hat{p}) - \frac{\partial}{\partial p^0}\Sigma(\hat{p}) = \mathcal{O}\left(e^{-\sqrt{3}m/2}\right). \tag{3.9}$$

After quite some work the final asymptotic formula for the mass shift becomes

$$\Delta m(L) = -\frac{3}{16\pi m^2 L}\left[\lambda^2 e^{-\sqrt{3}m/2} + \frac{m}{\pi}\int_{-\infty}^{\infty} dy e^{-\sqrt{m^2+y^2}L} F(iy) + \mathcal{O}\left(e^{-\tilde{m}}\right)\right], \tag{3.10}$$

where $\tilde{m}$ is larger than m and λ is the cubic coupling. $F(x)$ is the elastic forward scattering amplitude with x being the crossing variable. The careful proof of this formula is quite long and will not be recited here. The details can be found in [32].

If we consider the scalar field theory discussed above an effective theory for the pions of our gauge theory in the chirally broken regime, the cubic coupling λ will be zero since the pions are pseudoscalars. Furthermore the mass can be directly translated into the pion mass m_{PS} and the forward scattering amplitude F is also that of the pions. Chiral perturbation theory tells us that $F = -\frac{m_{\text{PS}}^2}{f_{\text{PS}}^2}$ to leading order.

Inserting this in the asymptotic formula (3.10) we get

$$\Delta m_\pi(L) \simeq m_{\text{PS}} \frac{3}{8\pi^2 m_{\text{PS}} L} \frac{m_{\text{PS}}^2}{f_{\text{PS}}^2} \cdot \frac{2}{\pi}\int_{-\infty}^{\infty} dy e^{-\sqrt{m_{\text{PS}}^2+y^2}L} \tag{3.11}$$

to leading order in chiral perturbation theory and to order $e^{-\tilde{m}L}$. The last part is a modified Bessel function

$$\frac{2}{\pi}\int_{-\infty}^{\infty} dy e^{-\sqrt{m_{\text{PS}}^2+y^2}L} = K_1(m_{\text{PS}}L). \tag{3.12}$$

For large $m_{\text{PS}}L$ this goes as

$$K_1(m_{\text{PS}}L) \simeq \frac{e^{-m_{\text{PS}}L}}{\sqrt{m_{\text{PS}}L}}. \tag{3.13}$$

If the regime being probed is not close enough to the infinite volume limit the behaviour might differ somewhat[33]. Also in [31] a different relation than (3.11) is observed. Their results for SU(3) with Wilson fermions in the fundamental representation on $L = 10, 12, 14, 16$ and 24 suggests a dependence on L in physical units[3] rather than $m_{\text{PS}}L$.

---

[3] The scale is set using the Sommer radius.

3.2 CONTINUUM LIMIT

Finding the continuum limit of a physical quantity computed on the lattice is a major challenge. Simulating a lattice theory at a very small cutoff length scale while retaining a large enough volume is numerically very demanding. The final leap from lattice measurements to a continuum prediction is based on extrapolation. In our work we have not made use of any of the improvement schemes available that can accelerate the approach to the continuum limit. We use the standard Wilson prescription for the fermion action which solves the fermion doubler problem by introducing a double derivative term in the fermion action

$$\gamma^{\mu}\partial_{\mu} \longrightarrow \frac{1}{2}\left(\gamma^{\mu}\partial_{\mu}^{\mathrm{FW}} + \gamma^{\mu}\partial_{\mu}^{\mathrm{BW}} - r a \partial^{\mathrm{FW}\mu}\partial_{\mu}^{\mathrm{BW}}\right). \tag{3.14}$$

Here $\partial_{\mu}^{\mathrm{FW}}$ and $\partial_{\mu}^{\mathrm{BW}}$ denotes the forward and backward derivatives. r is a parameter which we will usually set to unity. a is the lattice spacing. The double derivative term will vanish linearly with a so that the correct continuum limit is reached. The term gives a mass $\propto 1/a$ to the unwanted fermion degrees of freedom sitting at the edges of the Brillouin zone, but it also breaks chiral symmetry explicitly.

Although the lattice regulator was put in place in order to study strongly coupled gauge models non-perturbatively, lattice perturbation theory can be used to gain confidence in the existence of the correct continuum limit. Indeed it has been shown to all orders in perturbation theory[34, 35] that all terms diverging as $a \to 0$ cancel. The remaining leading correction from the lattice cutoff is $\mathcal{O}(a)$. Consequently a linear extrapolation towards the chiral limit should be reasonable if the lattice spacing is small enough.

3.3 CHIRAL LIMIT

The last limit that we have yet to discuss is the chiral limit. This work has focused on two models of technicolor where we observe chiral symmetry breaking in both cases. Therefore it is natural to discuss the chiral limit in the framework of chiral perturbation theory. The issue is certainly a non-trivial one as can be read in the notes from a "Panel discussion on chiral extrapolation of physical observables"[36] in 2002. In particular it is noted that using normal chiral perturbation theory, the coefficient of the chiral log in the pion mass is fixed by the value of the pion decay constant which can be determined independently.

$$\frac{m_{\mathrm{PS}}^{2}}{m_{q}} = A\left[1 + \frac{A m_{q}}{16\pi^{2} N_{\mathrm{f}} f_{\mathrm{PS},0}^{2}} \log\left(\frac{A m_{q}}{\Lambda^{2}}\right)\right] + \mathcal{O}(m_{q}). \tag{3.15}$$

Fitting to lattice data from the JLQCD collaboration a very different value for the pion decay constant $f_{\mathrm{PS},0}$ is found by fitting this coefficient compared to the value found by looking directly in that channel. Also the coefficient of the chiral log in the pion decay constant should be, but is not, consistent with one value of $f_{\mathrm{PS},0}$ since

$$\frac{f_{\mathrm{PS}}}{f_{\mathrm{PS},0}} = 1 - \frac{A N_{\mathrm{f}} m_q}{32\pi^2 f_{\mathrm{PS},0}^2} \log\left(\frac{A m_q}{\Lambda^2}\right) + \mathcal{O}(m_q)\,. \tag{3.16}$$

In the panel discussion[36] it was suggested that the QCD data used in the fits were simply not close enough to the chiral limit.

Although the data could not provide a consistent value of $f_{\mathrm{PS},0}$ within chiral perturbation theory, it is possible to achieve nice fits to lattice data by letting the chiral log coefficients be varied independently.

A possible explanation is that lattice artefacts cannot be neglected in the derivation of the effective Lagrangian. For Wilson fermions a chiral expansion has been carefully developed[37, 38, 39, 40, 41]. At order a^2 at next-to-leading order in the chiral expansion, the effective Lagrangian contains more parameters (3 for Wilson fermions). Consequently, the pion decay constant $f_{\mathrm{PS},0}$ is no longer overdetermined by the chiral fits to m_{PS}^2 and f_{PS}.

Hyperscaling in mass deformed conformal gauge theories

If chiral symmetry is not spontaneously broken in the model under consideration then we will expect an approach towards the massless limit which is characterized by a critical exponent, the anomalous dimension γ which is universal for the entire spectrum. This is referred to as hyperscaling relations. A discussion of the hyperscaling relations in mass deformed conformal gauge theories can be found in [42]. Here the derivation of the hyperscaling relations will not be given although they follow quite simply from a scaling hypothesis. The relations relevant in our work are

$$m_{\mathrm{PS}} = A m^{\frac{1}{1+\gamma}} \quad , \quad m_{\mathrm{V}} = B m^{\frac{1}{1+\gamma}} \quad \text{and} \quad F_{\mathrm{PS}} = C m^{\frac{1}{1+\gamma}}\,. \tag{3.17}$$

Later in this project we will perform fits to the spectral data from our lattice simulations using both the predictions from Wilson chiral perturbation theory and the above hyperscaling relations.

GPU accelerated Hybrid Monto Carlo algorithm

4

The growth in computational peak performance compared to price is rapid and has been so for many years. This is true for both high-end supercomputers as well as personal computers. Modern cutting-edge computing units have multiple computing cores and in order to harness their full potential one must properly parallelize the tasks given to them. Of course, some problems are more suited for parallel architectures than others. Fortunately, the numerical investigation of lattice gauge theories represents a task which is well suited for a very high degree of parallelism. Graphics processing units (GPUs) admits very high parallelism even compared to todays multi-core CPUs. Therefore they might make a better choice as the hardware to drive modern lattice gauge theory computations. In this chapter we demonstrate how one can tailor a state-of-the-art software suite for modern lattice simulations[43] with fermions in higher representations to run with high performance on GPUs. In particular we will demonstrate how SU(2) lattice gauge theories with fermions in the fundamental or adjoint representation is implemented, and we will perform benchmark tests and compare with performance on an Intel Xeon CPU cluster.

4.1 INVERSION OF THE FERMION MATRIX

The Wilson fermion action is

$$S_f(U,q,\bar{q}) = \sum_f \sum_{x,y} \bar{q}_f(x) D(x,y) q_f(y) \,, \tag{4.1}$$

with f running over fermion flavors. The Wilson-Dirac matrix $D(x,y)$ is given by

$$\begin{aligned}\sum_y D(x,y)q(y) &= (4+m_0)q(x) \\ &\quad -\frac{1}{2}\sum_\mu \Big[(1+\gamma_\mu)U^\dagger_{R\mu}(x-\hat{\mu})q(x-\hat{\mu}) \\ &\qquad\qquad + (1-\gamma_\mu)U_{R\mu}(x)q(x+\hat{\mu})\Big].\end{aligned} \tag{4.2}$$

U_R are the gauge links in the representation R. Without the subscript the representation is fundamental.

As discussed in chapter 2 the fermionic part of the action is Gaussian and it can be formally integrated out using formula (2.3) yielding a determinant. This determinant can in turn be expressed, using formula (2.4), as a functional integral over scalar fields termed *pseudofermions*

$$(\det D)^{N_f} = \int \mathscr{D}\phi\mathscr{D}\bar{\phi}\exp\left[-\phi^\dagger D^{-N_f}\phi\right]. \tag{4.3}$$

To simulate the theory we use the Hybrid Monte Carlo (HMC) algorithm[44]. Numerically the most demanding part of the algorithm is the inversion of Dirac operator, i.e, solving x from the following equation

$$Dx = \phi. \tag{4.4}$$

There are multiple algorithms available, but the most efficient ones are Krylov subspace inverters. We use the Quasi-Minimal Residual Algorithm (Alg. 1) to solve Eq. (4.4).

Even-odd preconditioning

Due to the nearest-neighbor type interactions of the fermions on the lattice it is possible to precondition the linear system (4.4). We will not go into too many details with this procedure, but merely outline the strategy.

If the vectors in the linear system (4.4) have all degrees of freedom corresponding to the even lattice sites in the upper half and the odd lattice sites in the lower half then we can write the system using a block matrix notation

$$\begin{pmatrix} \frac{1}{\kappa}\mathbb{1} & -D_{\mathrm{EO}} \\ -D_{\mathrm{OE}} & \frac{1}{\kappa}\mathbb{1} \end{pmatrix}\begin{pmatrix} x_{\mathrm{E}} \\ x_{\mathrm{O}} \end{pmatrix} = \begin{pmatrix} \phi_{\mathrm{E}} \\ \phi_{\mathrm{O}} \end{pmatrix} \tag{4.5}$$

Note that $\kappa = \frac{1}{2m_0+8}$ is the Hopping parameter and that we have scaled out a factor of $\frac{1}{2}$. Writing out the two equations yield

$$\frac{1}{\kappa}x_{\mathrm{E}} - D_{\mathrm{EO}}x_{\mathrm{O}} = \phi_{\mathrm{E}}\,, \tag{4.6}$$

$$\frac{1}{\kappa}x_{\mathrm{O}} - D_{\mathrm{OE}}x_{\mathrm{E}} = \phi_{\mathrm{O}}\,. \tag{4.7}$$

Applying D_{EO} to the second equation gives

$$\frac{1}{\kappa} D_{\mathrm{EO}} x_{\mathrm{O}} - D_{\mathrm{EO}} D_{\mathrm{OE}} x_{\mathrm{E}} = D_{\mathrm{EO}} \phi_{\mathrm{O}} . \tag{4.8}$$

$D_{\mathrm{EO}} x_{\mathrm{O}}$ can be isolated from the first equation and inserted in the above. This gives

$$\left(\frac{1}{\kappa^2} - D_{\mathrm{EO}} D_{\mathrm{OE}} \right) x_{\mathrm{E}} = \chi_{\mathrm{E}} , \tag{4.9}$$

where $\chi_{\mathrm{E}} = \frac{1}{\kappa} \phi_{\mathrm{E}} + D_{\mathrm{EO}} \phi_{\mathrm{O}}$. The linear system 4.9 is called the even-odd preconditioned system. It is practical to solve this system rather than the unpreconditioned one since the convergence of the iterative solver is faster.

For all simulations in our work we use even-odd preconditioning. For the benchmark tests of our GPU implementation (section 4.5) it is specified when even-odd preconditioning is used.

Algorithm 1 Quasi-Minimal Residual Algorithm

```
$x_0 :=$ initial guess
$r_0 := \phi - D x_0$
$\gamma_1 := |r_0|$
$w_1 := v_1 := r_0 / \gamma_1$
$w_0 := v_0 := \beta_1 := \delta_1 := 0$
for m=1,2... until $|\gamma_m| < \varepsilon |b|$ do
    { LANCZOS BIORTHOGONALIZATION }
    $\alpha_m = (w_m, A v_m)$
    tmp1 := $D v_m - \alpha_m v_m - \beta_m v_{m-1}$
    tmp2 := $D^\dagger w_m - \alpha_m^* w_m - \delta_m^* w_{m-1}$
    $\delta_{m+1} := |(\mathrm{tmp1}, \mathrm{tmp2})|^{\frac{1}{2}}$
    $\beta_{m+1} := (\mathrm{tmp1}, \mathrm{tmp2}) / \delta_{m+1}$
    $v_{m+1} := \mathrm{tmp1} / \beta_{m+1}$
    $w_{m+1} := \mathrm{tmp2} / \delta_{m+1}$
    { UPDATE QR FACTORIZATION OF MATRIX $T_m$ }
    for $i = 1, 2, ..., m-1$ do
        $t_m := \Omega_i t_m$ { $\Omega_i$ are Givens rotations (4.17), $t_k$ are columns of $T_m$}
    end for
    Construct $\Omega_m$ using (4.18)
    $t_m := \Omega_m t_m$
    $\gamma_{m+1} := -s_m \gamma_m$
    $\gamma_m := c_m \gamma_m$
    { NEXT ITERATE }
    $p_m := (v - t_{m-2,m} p_{m-2} - t_{m-1,m} p_{m-1}) / t_{mm}$
    $x_m = m_{m-1} + \gamma_m p_m$
end for
```

4.2 QUASI-MINIMAL RESIDUAL ALGORITHM

The algorithm 1 is based on the Lanczos Biorthogonalization procedure which builds a pair of biorthogonal basis $\{v_j\}$, $\{w_j\}$, $j = 1, \ldots, m$ for the Krylov subspaces $\mathscr{K}_m = \text{span}\{v_1, Dv_1, \ldots, D^{m-1}v_1\}$ and $\mathscr{K}_m^* = \text{span}\{w_1, D^\dagger w_1, \ldots, (D^\dagger)^{m-1}w_1\}$. Here D is the matrix defining the linear system to be solved.

In Alg. 1 the coefficients α_j,β_j and δ_j are computed. These can be arranged into a tridiagonal $m \times m$ matrix T_m

$$T_m = \begin{pmatrix} \alpha_1 & \beta_2 & & \\ \delta_2 & \alpha_2 & \ddots & \\ & \ddots & \ddots & \beta_m \\ & & \delta_m & \alpha_m \end{pmatrix}. \tag{4.10}$$

T_m is the oblique projection of D onto $\mathscr{K}_m$ orthogonal to $\mathscr{K}_m^*$,

$$DV_m = V_m T_m + \delta_{m+1} v_{m+1} e_m^\dagger \equiv V_{m+1} \overline{T}_m \quad , \quad \overline{T}_m = \begin{pmatrix} T_m \\ \delta_{m+1} e_m^T \end{pmatrix}, \tag{4.11}$$

where V_m is a matrix with column vectors v_j, $j = 1, ..., m$. Similarly $T_m^\dagger$ is the oblique projection of $D^\dagger$ onto $\mathscr{K}_m^*$ orthogonal to $\mathscr{K}_m$,

$$D^\dagger W_m = W_m T_m^\dagger + \beta_{m+1} w_{m+1} e_m^\dagger, \tag{4.12}$$

Now, since we define the first vector v_1 to be a multiple of the first residual r_0, we can calculate the residual of some approximate solution $x_m = x_0 - V_m y$ by

$$\phi - Dx = V_{m+1}\left(\beta e_1 - \overline{T}_m y\right) \quad \text{if} \quad v_1 = \beta r_0 .$$

The game is now to choose y in order to minimize the residual. This problem would have been greatly simplified had the vectors $v_1, ..., v_m$ been orthogonal. In that case the minimizer y of

$$\left\| V_{m+1}\left(\beta e_1 - \overline{T}_m y\right)\right\|$$

would have coincided with the minimizer y of

$$\left\| \beta e_1 - \overline{T}_m y \right\| . \tag{4.13}$$

This is the kind of minimization problem that arizes in the Generalized Minimal Residual (GMRES) algorithm and similar Arnoldi based algorithms. In the QMR algorithm the fact that

$v_1, \ldots, v_m$ are not orthogonal is ignored and the approximate solutions are simply chosen to minimize (4.13) which is referred to as the *quasi-residual.* We will deal with this minimization problem shortly.

An important advantage of this algorithm compared to the GMRES algorithm is that the number of system-sized vectors needed to be stored does not increase with the dimension of the Krylov subspace.

From a practical point of view the QMR algorithm is attractive also because it is possible to use the γ_5 hermiticity of the fermion matrix to save the $D^\dagger$ operation.

If one replaces in the initialisation of algorithm 1 the assignment of w_1 with

$$v_1 := \frac{v_1}{\sqrt{(v_1, \gamma_5 v_1)}} \tag{4.14}$$

$$w_1 := \gamma_5 v_1 \,, \tag{4.15}$$

then the Lanczos biorthogonalization can be achieved using only the D_m operation. The scaling of v_1 is to maintain $(v_i, w_j) = \delta_{ij}$. When this is in place biorthogonalization can be achieved efficiently by noting that the temporary variables in algorithm 1 obey

$$\text{tmp2} = \gamma_5 \text{tmp1} \,.$$

Notice also that the scalars entering the QMR algorithm will be real in this case.

Breakdown of the QMR algorithm

The Lanczos biorthogonalization in algorithm 1 breaks down if $\delta_{m+1} = |(\text{tmp1}, \text{tmp2})|^{\frac{1}{2}}$ is zero or very close to. This can happen for one of two reasons:

Lucky breakdown One of the vectors tmp1 or tmp2 are zero. In this case an exact solution to the linear system has been found.

Serious breakdown tmp1 and tmp2 are orthogonal. In this case the current iterate is not an exact solution to the linear system. Some procedure to deal with this scenario must be put in place. There are several options. One of them is to implement so called look-ahead algorithms which will allow the QMR to skip the problematic Lanczos step and move on. However this will greatly increase the complexity of the algorithm. It is noted in [45] that it is often more convenient to restart the iterative process.

Minimizing the Quasi-Residual

We have seen that finding the approximate solution in the QMR algorithm involved finding the minimizer y of the quasi-residual 4.13. This is a fairly simple task. The technique uses so called Givens rotations to rotate away the subdiagonal entries of the tridiagonal $\overline{T}_m$ matrix. Consider the case of $m = 4$

$$\overline{T}_m = \begin{pmatrix} \alpha_1 & \beta_2 & & \\ \delta_2 & \alpha_2 & \beta_3 & \\ & \delta_3 & \alpha_3 & \beta_4 \\ & & \delta_4 & \alpha_4 \\ & & & \delta_5 \end{pmatrix} \xrightarrow{\Omega_1} \begin{pmatrix} t_{11}^{(1)} & t_{12}^{(1)} & t_{13}^{(1)} & \\ & t_{22}^{(1)} & t_{23}^{(1)} & \\ & \delta_3 & \alpha_3 & \beta_4 \\ & & \delta_4 & \alpha_4 \\ & & & \delta_5 \end{pmatrix} \xrightarrow{\Omega_2} \begin{pmatrix} t_{11}^{(2)} & t_{12}^{(2)} & t_{13}^{(2)} & \\ & t_{22}^{(2)} & t_{23}^{(2)} & t_{24}^{(2)} \\ & & t_{33}^{(2)} & t_{34}^{(2)} \\ & & \delta_4 & \alpha_4 \\ & & & \delta_5 \end{pmatrix}$$

$$\xrightarrow{\Omega_3} \begin{pmatrix} t_{11}^{(3)} & t_{12}^{(3)} & t_{13}^{(3)} & \\ & t_{22}^{(3)} & t_{23}^{(3)} & t_{24}^{(3)} \\ & & t_{33}^{(3)} & t_{34}^{(3)} \\ & & & t_{44}^{(3)} \\ & & & \delta_5 \end{pmatrix} \xrightarrow{\Omega_4} \begin{pmatrix} t_{11}^{(4)} & t_{12}^{(4)} & t_{13}^{(4)} & \\ & t_{22}^{(4)} & t_{23}^{(4)} & t_{24}^{(4)} \\ & & t_{33}^{(4)} & t_{34}^{(4)} \\ & & & t_{44}^{(4)} \\ & & & \end{pmatrix}. \tag{4.16}$$

The k^{th} rotation will have the form

$$\overline{\Omega}_k = \begin{pmatrix} 1 & & & & & & \\ & \ddots & & & & & \\ & & 1 & & & & \\ & & & \cos\theta_k & \sin\theta_k & & & \\ & & & -\sin\theta_k & \cos\theta_k & & & \\ & & & & & 1 & & \\ & & & & & & \ddots & \\ & & & & & & & 1 \end{pmatrix}, \tag{4.17}$$

where the first $\cos\theta_k$ appears in the k^{th} diagonal element, and the angle of rotation is given by

$$\cos\theta_k = \frac{t_{kk}^{(k-1)}}{\sqrt{\left(t_{kk}^{(k-1)}\right)^2 + \delta_{k+1}^2}} \quad , \quad \sin\theta_k = \frac{\delta_{k+1}}{\sqrt{\left(t_{kk}^{(k-1)}\right)^2 + \delta_{k+1}^2}}. \tag{4.18}$$

Here $t_{00}^{(0)} = \alpha_1$. Conventionally the product of all the Givens rotations are denoted by Q

$$Q = \Omega_m \Omega_{m-1} \cdots \Omega_1 , \tag{4.19}$$

and the product of $\overline{T}_m$ with Q is called the $\overline{R}$ such that

$$\overline{T}_m = Q^\dagger \overline{R}, \tag{4.20}$$

This decomposition of $\overline{T}_m$ is a so called QR factorization. Clearly Q is unitary and it follows that

$$\left\| \beta e_1 - \overline{T}_m y \right\|_2 = \left\| \beta Q e_1 - \overline{R} y \right\|_2 . \tag{4.21}$$

The minimum as well as the minimizer of the right hand side is easy to find. Note that the $(m+1) \times m$ matrix $\overline{R}$ only has zeros on the bottom row so we can write

$$\overline{R} = \begin{pmatrix} & R & \\ 0 & \cdots & 0 \end{pmatrix}, \tag{4.22}$$

where R is an $m \times m$ matrix. This means that the minimizer of (4.21) solves the linear upper triangular system

$$g - Ry = 0, \tag{4.23}$$

where g denotes the fist m components of $\beta Q e_1$. The quasi-residual is then the $(m+1)^{\text{th}}$ component of $\beta Q e_1$.

4.3 MIXED PRECISION SOLVERS

The single precision floating point operations are faster than double precision operations, e.g., a single precision Dirac operator is about three times faster than a double precision Dirac operator. Therefore it is advantageous to use mixed precision solvers. The strategy is to invert the system to single precision and then update the solution and residual in double precision. Then repeating the single precision inversions until the desired precision is reached. One way of implementing this is written in algorithm 2, where double precision variables are indicated by a hat. This is called *defect correction* and is the method we employ. There are alternative update methods like *reliable updates*[46, 47].

A disadvantage of mixed precision solvers are that they are difficult to use as multi-shift solvers, but for our purposes, simulating doublets of fermions with the HMC algorithm, this is not a serious issue.

Algorithm 2 Mixed-Precision Quasi-Minimal Residual

```
$\hat{x} :=$ initial guess
$\hat{r} := \hat{\phi} - \hat{A}\hat{x}$
while $|\hat{r}_k| > \hat{\varepsilon}|\hat{b}|$ do
    $r := \hat{r}$
    $p := \hat{r}$
    $x := 0$
    Use Algorithm 1 to solve $x = D^{-1} r$ to precision precision $\varepsilon$
    $\hat{x} := \hat{x} + x$
    $\hat{r} := \hat{b} - \hat{A}\hat{x}$
end while
```

4.4 GPU IMPLEMENTATION AND OPTIMIZATION

The GPU code was implemented by modifying a parallel lattice code HiRep[43]. It is a generic code which can simulate any number of colors, number of fermion flavors, and fermion representation. This makes it ideal for studying theories beyond the Standard Model.

The GPU version of the code was programmed using the CUDA framework. The implementation of the code required writing of all the computationally intense parts in CUDA-kernels. Since the inversion of the Dirac operator is by far the most computationally demanding part, the most effort were put into the Dirac operator. This involves writing all the linear algebra routines with spinor fields as CUDA-kernels. The actual inverters need not be changed since they operate on a higher level and need not know where the linear algebra is carried out. Even though the gauge update is not very demanding a factor of two roughly was achieved by implementing it on the GPU. Thus it removes a lot of memory transfer between the host machine and the GPU, which is relatively slow and otherwise constitutes a bottleneck.

Spinor linear algebra

The implementation of almost all of the linear algebra operations of spinors are trivial since spinor fields are just vectors of complex numbers. Each operation on the individual complex components are simply distributed to individual CUDA threads. The exceptions being the summations needed in the inner product of two spinor fields along with variants of that like the γ_5 inner product. To implement these we used a temporary spinor field to store individual components $s^i_{\text{tmp}} = s^{i*}_1 \cdot s^i_2$ and then performed the summation using parallel reduction. We found that optimizing the global summation kernel did give a performance enhancement well worth the effort. One of the optimizations that proved rewarding was to do the first parallel reduction step already in the kernel calculating the product of complex numbers.

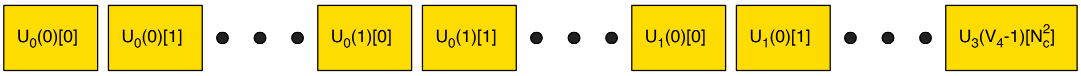

(a) Uncoalesced memory layout of gauge field

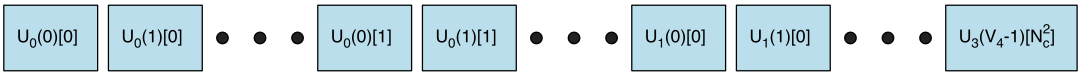

(b) Coalesced memory layout of gauge field

Figure 1: The ordering of the gauge field variables as it was before (a) and as it was changed to (b) in order to accommodate coalesced memory access. Here the index in square brackets refers to the indices of each gauge link matrix. Here we have used as an example a fundamental gauge link having N_c^2 entries.

Coalesced memory access

In the CUDA programs, special consideration has to be put into the organization of memory. The granularity of the GPU memory controller is 64 or 128 bytes. If one double precision number of 8 bytes is accessed, the controller loads 64 bytes and discards 56 bytes. However, if threads in a half warp (16 threads on the Tesla C2070) load consecutive memory addresses only one load is performed. This is called coalesced memory access.

In the Dirac operation and the gauge update, the objects being read from memory are gauge link matrices and Dirac spinors. The memory layout of the gauge links has been totally reordered in this implementation in order to ensure coalesced memory access. The old and the new memory layout can be seen from figure 1. Before the reordering the link matrices $U_\mu(x)$ was stored in a natural order as $U_0(0), U_0(1) \ldots U_3(V_4-1)$, where V_4 is the lattice 4-volume. In other words, all entries in a gauge link matrix was stored at consecutive memory addresses.

In our implementation the ordering starts with first gauge component of first link matrix $U_0(0)[0]$, then first gauge component of the second link matrix $U_0(1)[0]$ as shown in figure 1b. This means that a single gauge link matrix is not localized in memory. Now, when the thread 0 is operating on link matrix $U_0(0)$, thread 1 on $U_0(1)$ etc., they will be read in a coalesced manner from the global memory.

Coalescing the memory access increases the performance by about an order of magnitude. This probably makes it the most significant optimization step.

Packing the gauge links

The performance bottleneck of GPU calculations is usually the memory transfer bandwidth from global memory to the local memory. The actual computations on GPU take up only a small fraction of the total time. To increase the Compute-to-Global-Memory-Access ratio (CGMA) one can pack the global memory data to decrease the amount of data transfer. The unpacking then requires more computations, but typically an overall performance enhancement is achieved. This is indeed what we observe as well. Another advantage of the packing of memory is that bigger lattices will fit in the memory of each GPU. This is important since communication between different GPU units will have to pass through the host and is therefore very slow. Our implementation does not yet have support for multi-GPU scaling.

SU(2) gauge links

An SU(2) gauge link matrix is a 2 × 2 complex matrix meaning that 8 real numbers will have to be stored in memory if no packing is done. Clearly, there are potential for significant packing since in principle the information could be stored in a real 3-vector in the algebra.

However, since the mapping between 3 degrees of freedom an SU(2) matrix requires trigonometric functions, which are slow on GPU, we have decided to store the matrices in following format with four degrees of freedom

$$U = a_0 I + i \sum_{k=1}^{3} \sigma_k, \tag{4.24}$$

where σ_i are the Pauli matrices and a_0, a_1, a_2, a_3 satisfy

$$\sum_{\mu=0}^{3} a_\mu = 1. \tag{4.25}$$

Note that one cannot just store three of a_μ and solve the fourth using Eq. 4.25, since the sign would be unknown. This, of course, is nothing but the familiar identification of the group elements with unit quarternions.

On-the-fly construction of represented gauge links

When simulating gauge models with fermions transforming under other representations than the fundamental, a represented gauge field enters the fermion action (4.2). In the original CPU version of the HiRep code[43] this represented gauge field is constructed explicitly and stored in memory. It is possible to work out a mapping from the fundamental gauge matrices U to the represented ones U_{R}. The explicit mappings relevant in our work are

$$\text{SU}(2)\text{ adjoint:} \qquad U^{ab}_{\text{Adj}} = \frac{1}{2}\operatorname{Tr}\left[\tau^a U \tau^b U^\dagger\right] , \tag{4.26}$$

$$\text{SU}(3)\text{ sextet:} \qquad U^{ab}_{\text{S}} = \operatorname{Tr}\left[T^a_{\text{S}} U T^b_{\text{S}} U\right] . \tag{4.27}$$

In the above $\tau^a = \sigma^a/2$ are the generators of the fundamental representation of SU(2) and T^a_{S} constitute a basis for the sextet representation. These are given by

$$\begin{pmatrix} 1 & 0 & 0 \\ 0 & 0 & 0 \\ 0 & 0 & 0 \end{pmatrix}, \begin{pmatrix} 0 & 0 & 0 \\ 0 & 1 & 0 \\ 0 & 0 & 0 \end{pmatrix}, \begin{pmatrix} 0 & 0 & 0 \\ 0 & 0 & 0 \\ 0 & 0 & 1 \end{pmatrix}, \begin{pmatrix} 0 & \frac{1}{\sqrt{2}} & 0 \\ \frac{1}{\sqrt{2}} & 0 & 0 \\ 0 & 0 & 0 \end{pmatrix}, \begin{pmatrix} 0 & 0 & \frac{1}{\sqrt{2}} \\ 0 & 0 & 0 \\ \frac{1}{\sqrt{2}} & 0 & 0 \end{pmatrix}, \begin{pmatrix} 0 & 0 & 0 \\ 0 & 0 & \frac{1}{\sqrt{2}} \\ 0 & \frac{1}{\sqrt{2}} & 0 \end{pmatrix}.$$

The traces are over fundamental gauge indices.

The advantages of representing the gauge field on the fly are similar to those obtained by the packing of the gauge field. 1) the memory transfer from global to local memory is reduced thereby increasing the CGMA ratio. 2) The amount of allocated memory is reduced allowing bigger lattices to fit on one GPU.

Reduction of spilling

One of the limitations of GPUs is the number of registers. In large kernels, like the Dirac operator kernel, all the variables and intermediates will often not fit in the available registers. In this case the content of the registers need to be transferred to local memory. This is is referred to as spilling. Clearly, if the gauge group is small, like SU(2), the Dirac operator will not need as many registers as is the case for larger gauge groups. This is of cause also depending on the representation of the fermions.

To alleviate the spilling it is possible to spread the calculations over more computing threads. The downside of this procedure is often that the same variables need to be loaded multiple times from memory. For the SU(3) sextet model we have not managed to avoid the spilling, but for SU(2) with fundamental fermions the spilling could be avoided altogether[4] while in the case of adjoint fermions the spilling was drastically reduced. However, even small amounts of spilling have severe impact on performance.

In the double precision Dirac operator kernels we calculated only one component of each spinor pr. thread. This increases the memory transfer from the optimal since we need to load the same gauge link multiple times and the spinor twice. This means that the achieved memory bandwidth will be sub-optimal since multiple transfers of the same variable will only be

---

[4] When even-odd preconditioning is used a small amount of spilling is introduced. The impact of this is discussed in section 4.5.

Number of GPUs	1
Number of CUDA cores	448
CUDA core frequency	1.15 GHz
Memory bandwidth	144 GiB/s
Memory	6 GB GDDR5

Table 2: Nvidia Tesla C2070 Specifications

Number of cores	4
Clock frequency	2.66 GHz
Memory bandwidth	32 GiB/s
Instruction set	64 bit
L2 cache	4×256 KB
L3 cache	8 MB

Table 3: Intel Nehalem-EP CPU (X5550) Specifications

counted once. However, even with this downside taken into account, the spilling reduced Dirac kernel is faster than the one allowing the spilling.

The single precision Dirac operator kernels only require half the registers. This means that dividing the calculation into one spinor component pr. thread would be redundant. In fact, spreading out the calculation will in this case decrease performance due to unnecessary memory access.

With the next generation GPU cards, like the Nvidia Tesla K20, with more registers these optimization efforts will be redundant and the potential memory bandwidth can be exhausted even in the double precision kernels. Also, more registers might allow for spilling free Dirac operator kernels with bigger groups like SU(3).

4.5 PERFORMANCE OF SU(2) LATTICE GAUGE THEORIES ON GPU

To test our implementation we have performed various speed measurements on Nvidia Tesla C2070 GPUs. The specifications can be found in table 2. For comparison we have tested the CPU version on a computer cluster equipped with X5550 Intel Nahelem CPUs. The specifications of the CPUs can be found in table 3. Each node in the cluster has two CPUs. The Intel X5550 CPUs do not represent the cutting edge of modern CPUs. However, the Nvidia Tesla C2070 is not the fastest GPU on the market either, so we believe that the comparison is not unreasonable.

The performance of the Dirac operation on the GPU is summerized in figure 2. Here the achieved memory throughput is plotted at different lattice sizes. Figure 2a shows the performance when the fermions are in the fundamental representation and figure 2b shows the results when the fermions are in the adjoint representation. In both figures results for both single and double precision versions are displayed. For comparison we have also shown the performance achieved without the packing of the gauge fields and on-the-fly construction of the adjoint gauge field. The performance enhancement is clearly visible with fundamental fermions.

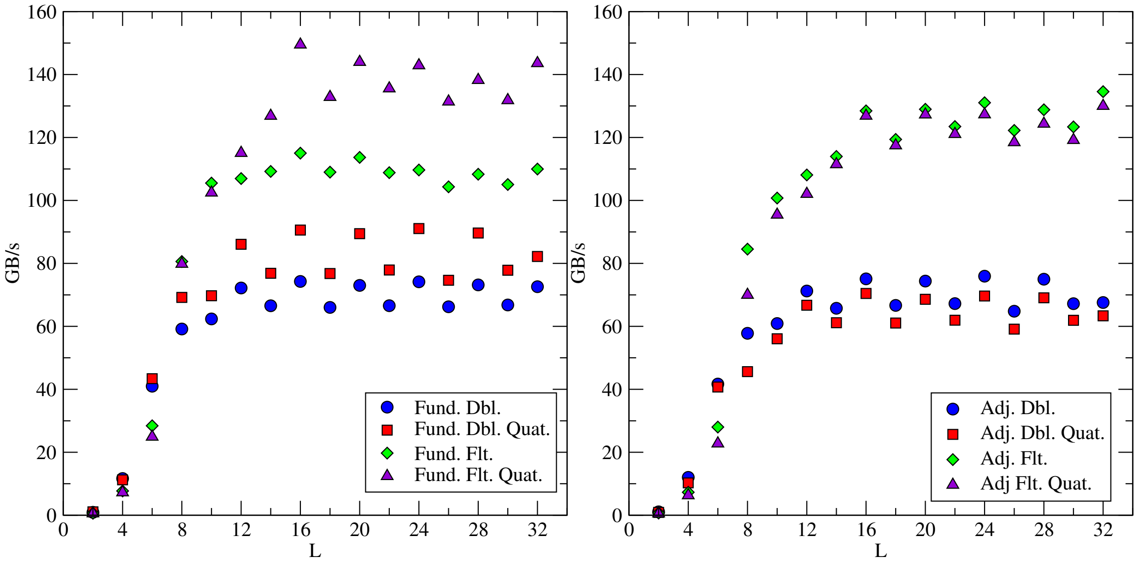

(a) Fermions in the fundamental representation.

(b) Fermions in the adjoint representation.

Figure 2: The memory throughput in the SU(2) Dirac operator with a) fermions in the fundamental representation and b) fermions in the adjoint representation. Where "Quat." is indicated in the legend the gauge fields have been stored using 4 real numbers and are represented on-the-fly. The tests have been carried out on lattices of size L^4.

However, with adjoint fermions the memory throughput is slightly smaller when the packing and on-the-fly representation is implemented, but since the packed gauge field occupies less memory a similar memory throughput means faster execution of the Dirac operator.

Notice from figure 2a that in the Dirac operation in single precision with fundamental fermions the memory throughput is roughly at the maximum theoretical value. This means that the actual computations are almost instantaneous.

Figure 3 shows a similar test with even-odd preconditioning enabled. In this case the performance is not as great in terms of memory bandwidth. There is no striking reason why this is so. In the case of the double precision Dirac operator kernels with even-odd preconditioning we were unable to remove all the spilling from the registers. However, with more work this could probably be achieved. Even though the memory throughput is below the unpreconditioned Dirac operation, the even-odd preconditioned Dirac operator will perform better in an actual simulation where iterative inversion of the Dirac operator is carried out.

Figure 4 shows the reduction in the time it takes to perform a Dirac operation upon packing the gauge field in a four component, quaternion format and representing the gauge field on the fly. As can be seen in the figure, a roughly 40 % reduction in time consumption is achieved in single precision with fermions in the fundamental representation and about 35 % in double

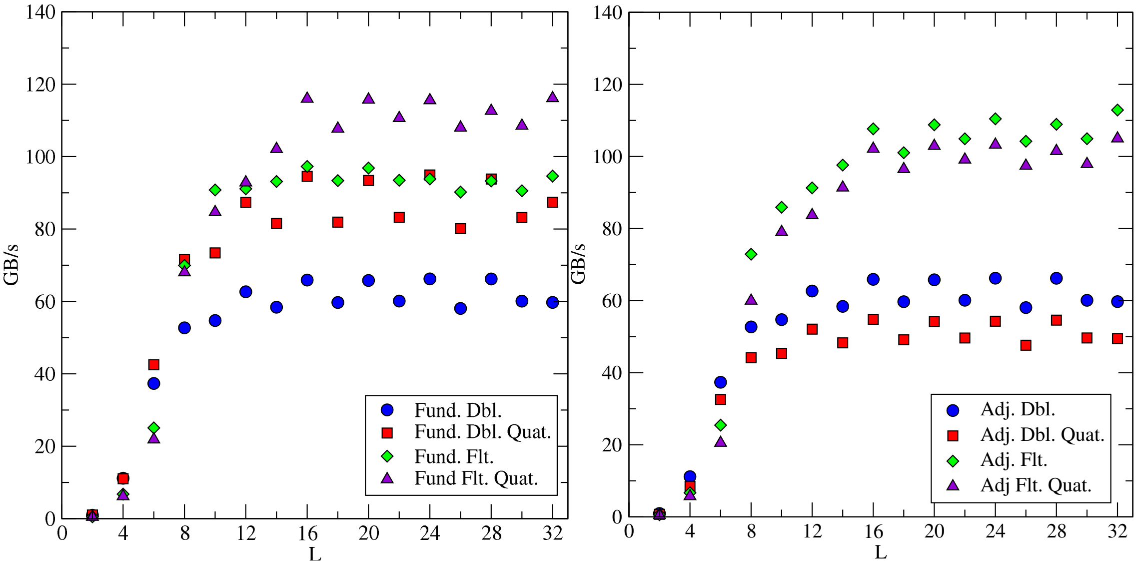

(a) Fermions in the fundamental representation. ***(b)*** Fermions in the adjoint representation.

Figure 3: The memory throughput in the SU(2) Dirac operator with even-odd preconditioning. Where "Quat." is indicated in the legend he gauge fields have been stored using 4 real numbers and are represented on-the-fly.

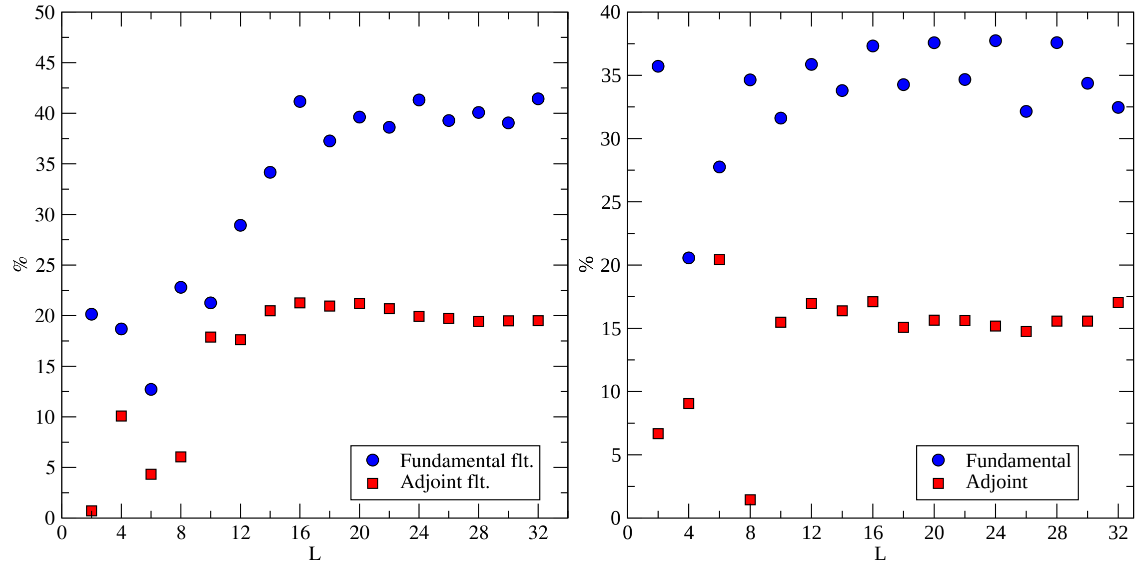

(a) Single precision. ***(b)*** Double precision

Figure 4: The relative reduction in the time it takes to perform a Dirac operation when the SU(2) gauge field is packed as unit quaternions and the gauge field is represented on-the-fly.

precision. With adjoint fermions the gain is somewhat smaller with about 20 % time reduction in single precision and about 15 % in double precision.

This might contradict the expectations since in the transfer of the represented gauge field is saved when representing the adjoint gauge field on-the-fly. Evidently this is not the case indicating also that the memory bandwidth is not the only component limiting the computational speed.

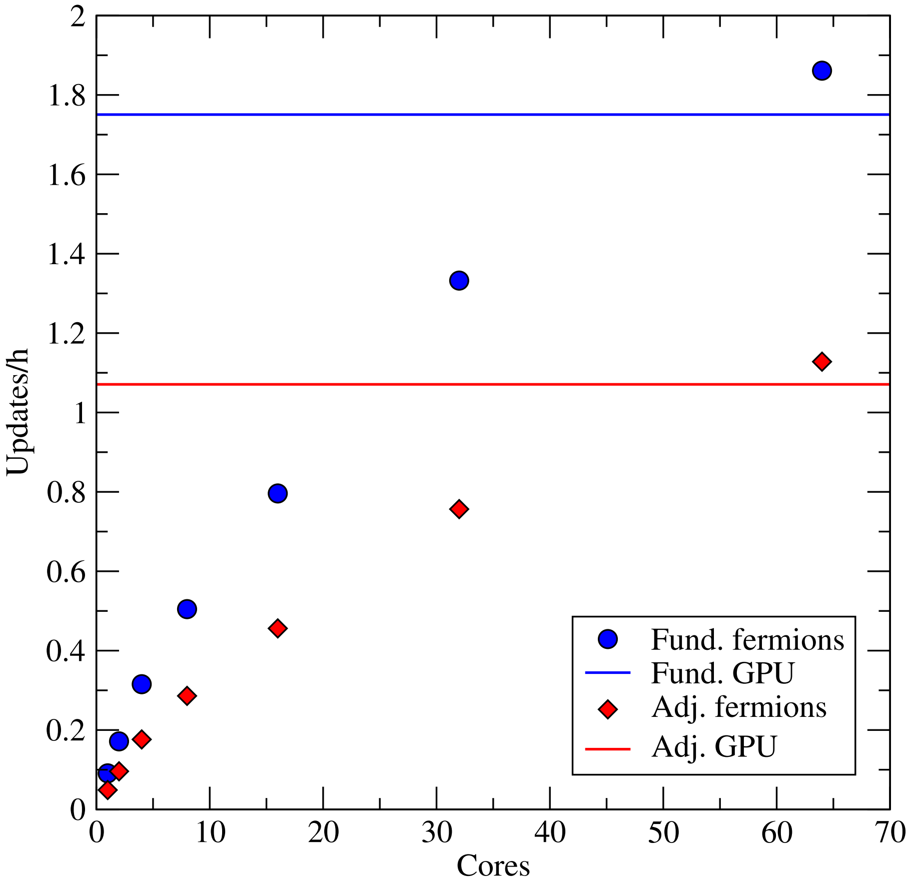

Figure 5: Comparison of actual simulation time between CPU version of the HiRep code and the GPU implementation. The ordinate axis denotes the number of HMC updates pr. hour. Both fundamental and adjoint model were simulated on a 32^4 lattice. The bare parameters for the fundamental model was $\beta = 2.2$, $m_0 = -0.72$. For the adjoint model we used $\beta = 2.5$, $m_0 = -1.05$. The abscissa represents the number of CPU cores used. Note that each node has two CPUs with 4 cores each.

It is of course of interest to compare the GPU implementation with the original CPU version of the code. We use the same setup as before, an Nvidia Tesla C2070 GPU (see table 2) in this test and compare against simulations performed on up to 64 Intel Nahelem X5550 CPU cores (see table 3). Each node in the CPU cluster has two quad-core CPUs giving a total of 8 cores pr. node. The simulations were carried out on a 32^4 lattice and even-odd preconditioning was used in the inversion of the Dirac operator. The parameters used in the simulations are specified in the caption of figure 5. The figure also shows the results. The GPU performs better than a 4 node/32 core CPU simulation and almost as well as an 8 node/64 core simulation.

4.6 SUMMARY AND OUTLOOK

We have demonstrated that simulations of lattice gauge theories make suitable tasks for GPUs. The naive transfer of the computations from CPU to GPU does not perform well, but with optimizations in place we were able to achieve good performance. In the case of an SU(2) gauge theory with fermions in the fundamental representation, we were able to achieve a memory throughput in the Dirac operator very close to the hardware maximum. The two most important optimization steps were the reordering of memory to accommodate coalesced memory access and the elimination/reduction of spilling in the Dirac operator kernels.

The packing of the SU(2) gauge field along with on-the-fly representation also accelerated the execution time of the Dirac operator, but this optimization gave 'only' a 20 - 45 % speedup.

In the case of SU(3) with sextet fermions we have not performed detailed benchmarking. The results would not be as good as with SU(2) models since spilling in the Dirac operator kernel is more severe. We did implement on-the-fly representation of the gauge field which gives a speedup of about 10 - 20 %.

The future of GPUs in scientific computing is promising. New generations of GPU devices with increased memory bandwidth and more registers will increase performance and make the GPUs easier to use. For larger scale simulations where multiple GPUs are required it will be necessary to carefully consider which inverter algorithm to use. This is because the transfer of memory between GPUs likely will be a bottleneck, especially if the GPUs are distributed over several nodes. Some research in this direction was presented in [48] where reasonable scaling was achieved with up to 256 GPUs. Technological progress is also being made in this direction. The Nvidia GPUDirect technology[5] allows copying of memory directly between GPUs on the same node. A recent development even bypasses the host memory completely while transferring memory between GPU cards on different nodes.

Considering these advancements in research and technology, GPU clusters provide an attractive platform for future large scale lattice gauge theory simulations.

---

[5] More information about this can be found at `https://developer.nvidia.com/gpudirect`.

5

SO(4) Fundamental Minimal Walking Technicolor with Wilson fermions

In this chapter the results of the article [49] by A. Hietanen, C. Pica, F. Sannino and UIS will be presented and discussed.

5.1 INTRODUCTION

We study the dynamics of an SO(4) gauge theory with two Wilson fermions in the fundamental representation. The lattice phase diagram is determined by locating the strong coupling bulk phase transition line and the zero PCAC mass line. We present results for the spectrum of the theory obtained at a fixed value of the lattice spacing. In particular we measure the pseudoscalar, vector and axial meson masses. The data favor a chiral symmetry breaking scenario rather than a conformal one.

When used to break the electroweak symmetry dynamically the model leads to a natural dark matter candidate.

5.2 CHIRAL SYMMETRY BREAKING PATTERN

The global flavor symmetry is enlarged in SO(N) gauge theories compared to SU(N) for N > 2 due to the following symmetry of the Dirac operator:

$$(\slashed{D}+m)C\gamma^5 = C\gamma^5(\slashed{D}+m)^*, \tag{5.1}$$

where $\slashed{D}=\gamma^\mu(\partial_\mu - igA^a_\mu\tau_a)$, $a=1,\dots,d[G]$ where $d[G]$ is the dimension of the adjoint representation of the gauge group. $C=i\gamma^0\gamma^2$ is the charge conjugation matrix. This symmetry is not present for complex representations of SU(N) gauge groups like the sextet representation of SU(3) that we will address in chapter6. For N_f massless Dirac fermions transforming under the fundamental representation of SO(N), the classical global symmetry will be $\mathrm{U}(2N_\mathrm{f})$. As usual the U(1) axial symmetry is anomalous so the quantum global symmetry is $\mathrm{SU}(2N_\mathrm{f})$.

Assuming maximal breaking of axial symmetries[50, 51] and respecting the Vafa-Witten theorem[52] by not breaking any vector symmetries, the resulting breaking pattern will be

$$\mathrm{SU}(2N_\mathrm{f}) \quad \longrightarrow \quad \mathrm{SO}(2N_\mathrm{f})\,. \tag{5.2}$$

The Goldstone manifold $\mathrm{SU}(2N_\mathrm{f})/\mathrm{SO}(2N_\mathrm{f})$ has $2N_\mathrm{f}^2 + N_\mathrm{f} - 1$ generators leading to nine Nambu-Goldstone bosons in the massless limit of the $N_\mathrm{f} = 2$ case.

The effective theory for the pseudo-Goldstone modes reads

$$\mathscr{L}_\mathrm{eff} = \frac{f^2}{2}\,\mathrm{Tr}\left(\partial^\mu \Sigma \partial_\mu \Sigma^\dagger\right) - G\,\mathrm{Re}\,\mathrm{Tr}\,(M\Sigma)\,, \tag{5.3}$$

G is a phenomenological coefficient, $M = m(\delta_{i,i+N_\mathrm{f}} + \delta_{i+N_\mathrm{f},i})$, $i = 1...N_\mathrm{f}$ is the quark mass matrix, and Σ is a symmetric unitary matrix in flavor space. Σ can be written as deviations around an average orientation $\bar{\Sigma}$.

$$\Sigma = U\bar{\Sigma}U^T, \quad U = \exp\left(\frac{i}{2f}\Pi\right),$$

where f is a normalization constant and $\Pi = \pi^a X_a/\sqrt{C}$ is a linear combination of generators X_a of the broken symmetries. C is their trace normalization $\mathrm{Tr}\, X_a X_b = C\delta_{ab}$ often chosen to be $2N_\mathrm{f}$.

The quark mass introduces a preferred direction in flavor space for chiral condensation to happen. The Gell-Mann–Oakes–Renner relation (GMOR)[53] relates phenomenological coefficients G and f to the pseudo Goldstone mass

$$m_\mathrm{PS}^2 = \frac{mG}{f^2}\,, \tag{5.4}$$

In the chiral limit $m \to 0$ the coefficient G is related to the chiral condensate through the relation $G = \langle \bar{q}q\rangle/2N_\mathrm{f}$ and f can be identified the with pseudo scalar decay constant.

If the model does not have an intrinsic chiral scale and $\langle \bar{q}q\rangle$ vanishes as m goes to zero the GMOR relation (5.4) will not work. A more thorough analysis can be found in [54].

Baryonic diquarks

To ease the language we will concentrate on the two flavour case and call these u and d. The Dirac spinors, u_{D} and d_{D}, can be constructed from Weyl spinors in the following way

$$u_{\mathrm{D}}^{a} = \begin{pmatrix} u_{\alpha}^{a} \\ \bar{\bar{u}}^{a\dot{\alpha}} \end{pmatrix}, \qquad d_{\mathrm{D}}^{a} = \begin{pmatrix} d_{\alpha}^{a} \\ \bar{\bar{d}}^{a\dot{\alpha}} \end{pmatrix}.$$

$a = 1,\ldots,d[r]$ denotes the SO(N_{C}) index where $d[r]$ is the dimension of the representation of the fermions. In the case of SO(N_{C}) with fundamental fermions $d[r] = N_{\mathrm{C}}$. The α indices on the Weyl fermions follow the SL$(2,\mathbb{C})$ transformation notation of Wess and Bagger[55] and Martin[56].

To construct gauge and Lorentz invariant states the color indices are contracted using a symmetric tensor δ_{ab} and the spinor indices are contracted using an antisymmetric tensor $\varepsilon^{\alpha\beta}$. In Appendix A this is done carefully, but here we will just state the resulting states

$$\Pi_{uu} \equiv u_{\mathrm{D}}^{T} C u_{\mathrm{D}}, \qquad \tilde{\Pi}_{uu} \equiv u_{\mathrm{D}}^{T} \gamma^{5} C u_{\mathrm{D}}, \tag{5.5}$$

$$\Pi_{dd} \equiv d_{\mathrm{D}}^{T} C d_{\mathrm{D}}, \qquad \tilde{\Pi}_{dd} \equiv d_{\mathrm{D}}^{T} \gamma^{5} C d_{\mathrm{D}}, \tag{5.6}$$

$$\Pi_{ud} \equiv u_{\mathrm{D}}^{T} C d_{\mathrm{D}}, \qquad \tilde{\Pi}_{du} \equiv d_{\mathrm{D}}^{T} \gamma^{5} C u_{\mathrm{D}} \tag{5.7}$$

$$\Pi_{du} \equiv d_{\mathrm{D}}^{T} C u_{\mathrm{D}}, \qquad \tilde{\Pi}_{ud} \equiv u_{\mathrm{D}}^{T} \gamma^{5} C d_{\mathrm{D}}. \tag{5.8}$$

$C = i\gamma^{0}\gamma^{2}$ is the charge conjugation matrix. All of the above have non-zero baryon number. The states of course also come with their conjugates $\Pi_{\bar{q}_1\bar{q}_2}$ and $\tilde{\Pi}_{\bar{q}_1\bar{q}_2}$.

Mesons

The scalar and pseudoscalar mesons read

$$\Pi_{\bar{u}u} \equiv \bar{u}_{\mathrm{D}} u_{\mathrm{D}}, \qquad \tilde{\Pi}_{\bar{u}u} \equiv \bar{u}_{\mathrm{D}} \gamma^{5} u_{\mathrm{D}} \tag{5.9}$$

$$\Pi_{\bar{d}d} \equiv \bar{d}_{\mathrm{D}} d_{\mathrm{D}}, \qquad \tilde{\Pi}_{\bar{d}d} \equiv \bar{d}_{\mathrm{D}} \gamma^{5} d_{\mathrm{D}}, \tag{5.10}$$

$$\Pi_{\bar{u}d} \equiv \bar{u}_{\mathrm{D}} d_{\mathrm{D}}, \qquad \tilde{\Pi}_{\bar{u}d} \equiv \bar{u}_{\mathrm{D}} \gamma^{5} d_{\mathrm{D}}, \tag{5.11}$$

$$\Pi_{\bar{d}u} \equiv \bar{d}_{\mathrm{D}} u_{\mathrm{D}}, \qquad \tilde{\Pi}_{\bar{d}u} \equiv \bar{d}_{\mathrm{D}} \gamma^{5} u_{\mathrm{D}}. \tag{5.12}$$

When implementing this new sector in the electroweak sector one will usually choose a more convenient basis for the technimesons

$$\begin{aligned} r &\equiv \Pi_{\bar{u}u} + \Pi_{\bar{d}d} & \Theta &\equiv \tilde{\Pi}_{\bar{u}u} + \tilde{\Pi}_{\bar{d}d}\,, \\ A^0 &\equiv \Pi_{\bar{u}u} - \Pi_{\bar{d}d} & \Pi^0 &\equiv \tilde{\Pi}_{\bar{u}u} - \tilde{\Pi}_{\bar{d}d}\,, \\ A^+ &\equiv \Pi_{\bar{d}u} & \Pi^+ &\equiv \tilde{\Pi}_{\bar{d}u}\,, \\ A^- &\equiv \Pi_{\bar{u}d} & \Pi^- &\equiv \tilde{\Pi}_{\bar{u}d}\,. \end{aligned} \tag{5.13}$$

These will be charge eigenstates. Note that Π^0, Π^+ and Π^- are pseudo Goldstone bosons whereas the others are not. The r state is analogous to the σ of QCD.

The vector mesons and baryons are stated in Appendix A. The states constructed above will be relevant for any theory with real representation fermions. All representations, except the spinorial, of the special orthogonal groups are real, but also the adjoint representation of any gauge group is real. There is however an important difference. If fermions transform under the adjoint representation, like in the SU(2) adjoint MWT model, we can also make gauge singlet quark-gluon states. With the simplest hypercharge assignments the quark-gluon state will be fractionally charged which demand careful attention from the model builder. In this sense the SO(4) MWT model is simpler than SU(2) adjoint MWT. Also, since every technifermion charged under the weak SU(2) gauge group, comes in multiples of four, the dimension of SO(4) fundamental, and not three as in SU(2) adjoint, there is no Witten topological anomaly[57] to be dealt with.

Phenomenology of the scalar diquarks

Important properties about the scalar diquarks can be inferred from the pseudoscalar mesons. In fact their correlation can be shown to be exactly identical. A proof of this for fermions in pseudoreal representations of the gauge group was given in [58]. When the fermions are in a real representation of the gauge group the reality property of the representation translates into the following symmetry of the Dirac operator

$$(\not{D} + m)C\gamma^5 = C\gamma^5(\not{D} + m)^*, \tag{5.14}$$

The symmetry also holds for the Wilson Dirac matrix in the lattice action (2.15).

A generic mesonic correlator will have the form

$$c^{(\Gamma)}_{\bar{q}q'}(x-y) = \mathrm{Tr}\left(\left[\bar{q}(x)\Gamma q'(x)\right]^\dagger \bar{q}(y)\Gamma q'(y)\right), \tag{5.15}$$

where Γ can be any of the matrices $\mathbf{1}, \gamma^5, \gamma^\mu, \gamma^\mu\gamma^5$. A baryonic diquark correlator will have the form

$$c^{(\Gamma)}_{qq'}(x-y) = \mathrm{Tr}\left(\left[q^T(x)C\Gamma q'(x)\right]^\dagger q^T(y)C\Gamma q'(y)\right). \tag{5.16}$$

Rewriting the diquark correlator slightly gives

$$c^{(\Gamma)}_{qq'}(x-y) = \mathrm{Tr}\left(\Gamma q'(y)\bar{q}'(x)\gamma^0\Gamma^\dagger C^\dagger(\gamma^0)^T\left[q(y)\bar{q}(x)\right]^T C\right). \tag{5.17}$$

Now we can invoke two identities

$$(\gamma^\mu)^T = -C\gamma^\mu C^\dagger, \tag{5.18}$$

$$q(x)\bar{q}(y) = C^\dagger\left[q(y)\bar{q}(x)\right]^T C. \tag{5.19}$$

The latter identity follows from the symmetry of the Dirac matrix given in (5.14) along with γ^5-hermiticity $\gamma^5(\not{D}+m)\gamma^5 = (\not{D}+m)^\dagger$. Invoking the identities in the expression for the diquark correlator (5.17) we have

$$c^{(\Gamma)}_{qq'}(x-y) = \mathrm{Tr}\left(\Gamma q'(y)\bar{q}'(x)\gamma^0\Gamma^\dagger\gamma^0 q(x)\bar{q}(y)\right) = c^{(\Gamma)}_{\bar{q}q'}(x-y). \tag{5.20}$$

A similar identity holds for the conjugated diquark state so

$$c^{(\Gamma)}_{qq'}(x-y) = c^{(\Gamma)}_{\bar{q}\bar{q}'}(x-y) = c^{(\Gamma)}_{\bar{q}q'}(x-y). \tag{5.21}$$

We can infer that the mesons and baryons come in degenerate trios - a meson, a diquark with opposite parity along with its antiparticle. In particular, the three standard parity odd Goldstone ’pion’ states come with six parity even Goldstone diquark baryons.

When electroweak interactions are switched on, the six Goldstone diquarks will form a complex isospin triplet T^+, T^0, T^-. The neutral component will be lighter due to isospin interactions and is a dark matter candidate in the model. This was discussed in more detail in [59], where also it was given the name "iTIMP" (isotriplet Technicolor Interacting Massive Particle).

Since this state has non-zero baryon number this can be an ingredient in an asymmetric dark matter scenario.

5.3 PERTURBATIVE ESTIMATES OF THE SO(N) CONFORMAL WINDOW

For model builders it is of utmost importance to know the details of the conformal window of gauge theories with fermion matter. The upper bound in the number of flavors N_f, where

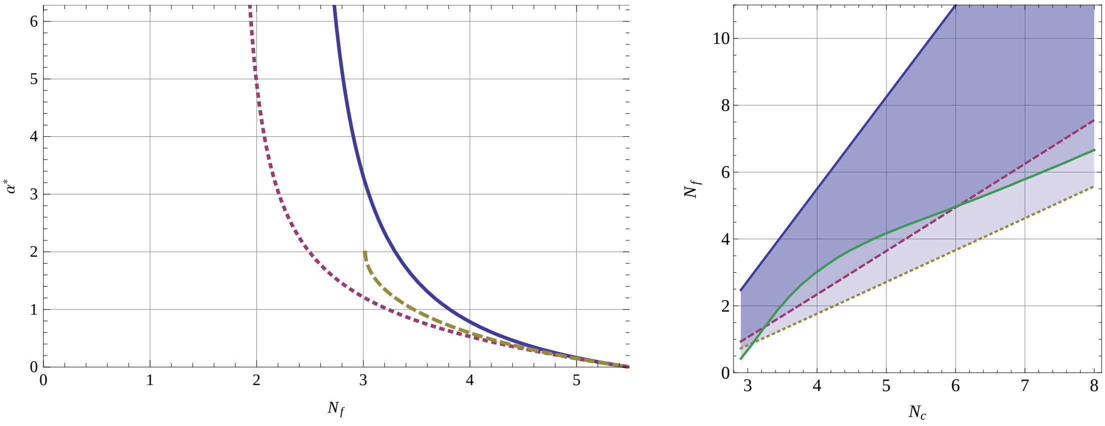

(a) Infrared fixed point couplings calculated at different orders in perturbation theory. The blue line is calculated from 2-loop β-function, dotted red line from 3-loop and dashed yellow from 4-loop.

(b) Conformal window of SO(N_c) with N_f Dirac fermions in the fundamental representation. Upper bound is when asymptotic freedom is lost. Lower bounds are 2-loop (red, dashed), 3-loop (yellow, dotted) and 4-loop estimates (green, solid).

Figure 6: Perturbative estimates of the renormalization of the gauge coupling. Calculations are performed in the $\overline{MS}$ scheme.

asymptotic freedom is lost, is easily determined in perturbation theory. The lower bound, where the IR fixed point is lost is another matter. Perturbative estimates exist, and we will state how they look for SO(N) gauge theories, but this is really overextending the realm of application of perturbation theory. Truly non-perturbative calculations are necessary in order to examine the infrared behaviour of the model.

Having stated this precaution, we proceed with the perturbative β function for the SO(4) gauge theory with N_f fermions in the fundamental representation. To 4 loop order in the $\overline{MS}$ scheme this reads

$$\begin{aligned}\frac{1}{2}\beta_{\text{4-Loop}}(a) = &+ a^2\left(\frac{4N_\mathrm{f}}{3}-\frac{22}{3}\right)\\ &- a^3\left(\frac{136}{3}-\frac{58N_\mathrm{f}}{3}\right)\\ &- a^4\left(N_\mathrm{f}\left(\frac{514N_\mathrm{f}}{27}-\frac{14767}{54}\right)+\frac{11428}{27}\right)\\ &+ a^5\frac{1}{972}\Big(-168(1080\zeta(3)+3841)N_\mathrm{f}^2+9(38976\zeta(3)+452449)N_\mathrm{f}\\ &\qquad\qquad -10784N_\mathrm{f}^3-32(45144\zeta(3)+148853)\Big),\end{aligned}$$

which for the case of $N_\mathrm{f}=2$ is

$$\frac{1}{2}\beta_{\text{4-Loop}}(a) = -\frac{14}{3}a^2-\frac{20}{3}a^3+\frac{1283}{27}a^4+\left(\frac{356681}{486}-\frac{13600\zeta(3)}{9}\right)a^5 .$$

The coupling a is defined as

$$a = \frac{g^2}{(4\pi)^2} = \frac{\alpha}{4\pi}.$$

The generic formula for the 4 loop β function for any gauge theory with fermionic matter was presented in [60]. If we set the β function to zero and solve for the coupling we find the perturbative estimates for the fixed points. Figure 6a shows the IR fixed point couplings as a function of the number of flavors calculated to 2, 3 and 4 loop order. We can see that with two Dirac flavors, which is the model we investigate in this work, the 2 loop calculation does not predict an IR fixed point. At 3 loop order a fixed point appears, but goes away again at 4 loop order. The perturbative calculation is therefore inconclusive regarding the existence of an IR fixed point.

The perturbative conformal window for a range of Dirac flavors N_f is shown in figure 6b. We will spend no more time on perturbation theory and rush on to the non-perturbative lattice studies of SO(4) with 2 Dirac flavors of Wilson fermions.

5.4 DELINEATION OF THE LATTICE PHASE DIAGRAM

The pure gauge sector of SO(N) gauge theories have previously been studied on the lattice. Earlier numerical studies focused mainly on the SO(3) gauge group [61] which is interesting due to the local, but not global isomorphism with SU(2). However Bursa *et al.* [62] have also studied higher values of N. Their studies are focused mainly on large N orbifold equivalence between SO(2N) and SU(N), but we can use their values for the location of the bulk phase transition to compare against ours. For SO(4) it was found that the bulk phase transition happens for $4.62(3) < \beta < 4.87(3)$, which is in agreement with our result in figure 7, where the same physics should be found at large bare quark mass.

Since this is the first lattice study of SO(4) with Wilson fermions, we have made a rough scan of the (β, m_0) parameter space on an $8^3 \times 16$ lattice. The bulk phase transition, determined from figure 7 at three different values of the bare mass m_0, is mapped to the phase diagram outlined in figure 9. The interval over which the measured average plaquette jumps is represented as horizontal errorbars on the phase diagram.

To determine the line of zero physical quark mass we use Partial Conservation of the Axial Current (PCAC)

$$m_\text{PCAC} = \lim_{t\to\infty} \frac{1}{2} \frac{\partial_t V_\text{PS}}{V_\text{PP}}, \tag{5.22}$$

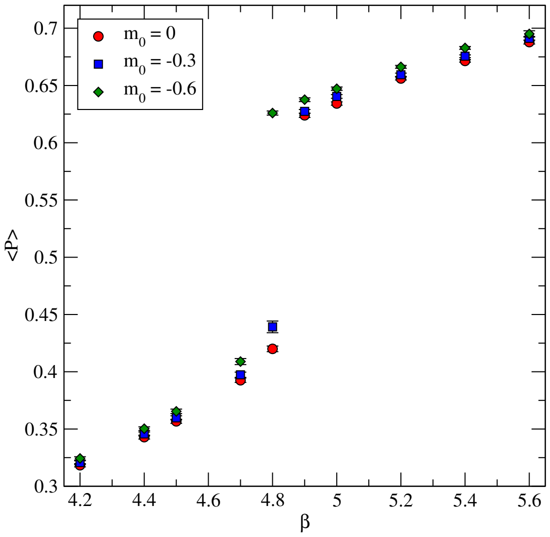

Figure 7: Average plaquette $\langle P \rangle$ vs. β on an $8^3 \times 16$ lattice at three different values of the bare mass.

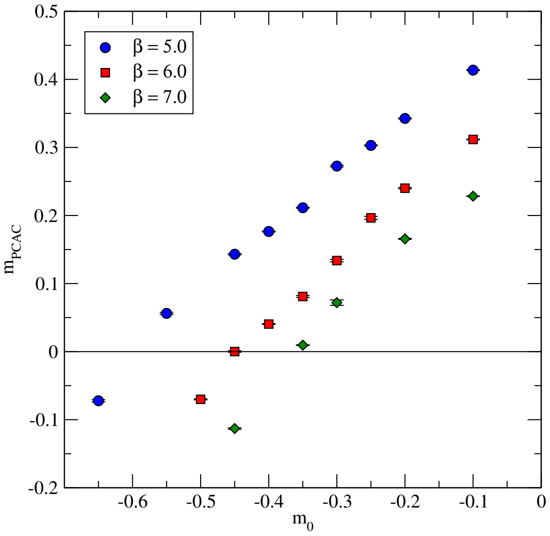

Figure 8: m_{PCAC} in units of inverse lattice spacing at three different couplings. The measurements are performed on a $8^3 \times 16$.

where the currents are

$$
\begin{aligned}
V_{\mathrm{PS}}(x_0) &= a^3 \sum_{x_1,x_2,x_3} \langle \bar{q}_1(x)\gamma_0\gamma_5 q_2(x)\bar{q}_1(0)\gamma_5 q_2(0)\rangle \,, \\
V_{\mathrm{PP}}(x_0) &= a^3 \sum_{x_1,x_2,x_3} \langle \bar{q}_1(x)\gamma_5 q_2(x)\bar{q}_1(0)\gamma_5 q_2(0)\rangle \,. \qquad (5.23)
\end{aligned}
$$

We identify m_{PCAC} with the physical quark mass. At each lattice spacing we measure m_{PCAC} at various values of m_0. Linear fits are made to data presented in figure 8. From the fits the intersection with the abscissa can be read. The results are plotted with circles in the phase diagram in figure 9.

With an outline of the lattice phase diagram in place we can proceed to measure the spectrum as we approach the chiral limit.

5.5 THE SPECTRUM OF SO(4) MWT

Numerical simulations

For these studies we have not been able to use the GPU implementation of the HiRep code[43] that was presented in chapter 4. This is because the study of the SO(4) model was conducted before the GPU enabled code was made. Therefore the configurations was made on CPU using the HMC algorithm[44] and in some cases the RHMC algorithm[63]. A summary of the gauge configurations used in these studies can be found in table 4. For the final calculations of the

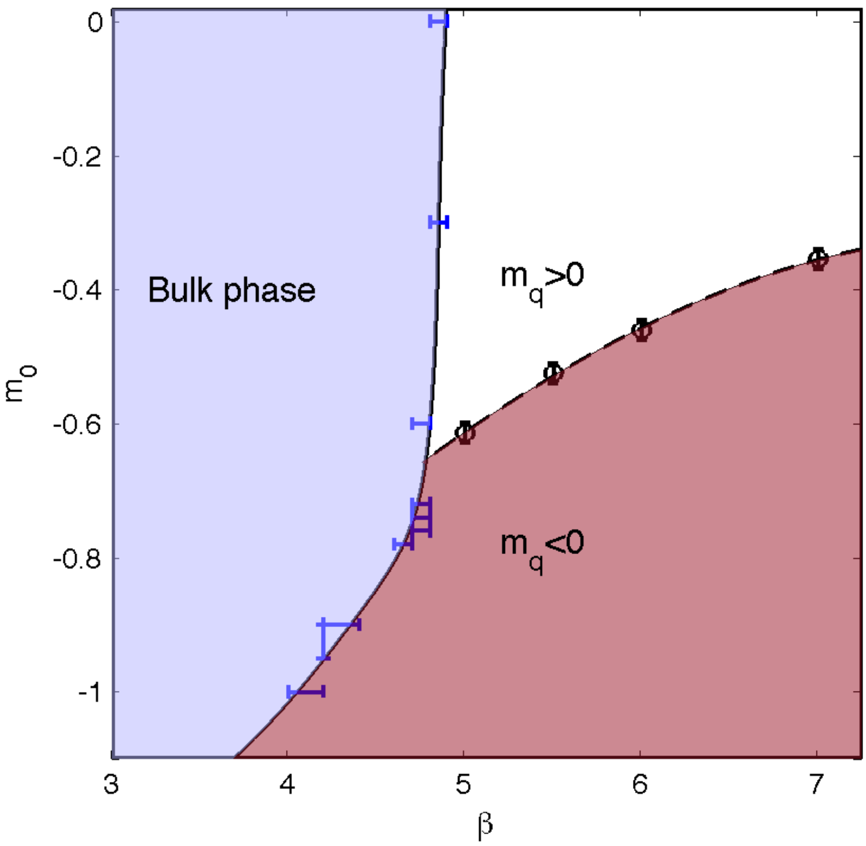

Figure 9: Lattice phase structure outlined on an $8^3 \times 16$ lattice. Circles represent points of critical bare mass where $m_{\text{PCAC}} = 0$. The transition to the bulk phase is first order. The error bars represent the interval over which the measured average plaquette jumps.

Volume	β	Iterations	Thermalization
$8^3 \times 16$	4.1,4.2…4.9, 5.2, 5.4, 5.6	2000	500
	4 4.5 5, 5.5, 6, 7	5000	2000
$12^3 \times 64$	5.5, 7	5000	1500
$24^3 \times 64$	7	850 - 2000	600

Table 4: Simulation parameters and thermalization times. For each coupling we performed multiple simulations with appropriate bare masses. The thermalization column refers to the number of discarded initial configurations.

spectrum of the theory we have used only data from the biggest lattices. Since only one lattice spacing is available at the biggest volume no continuum extrapolation is attempted.

The simulations were performed on three different lattices $8^3 \times 16$, $12^3 \times 64$ and $24^3 \times 64$ where in all cases the larger dimension is the temporal one. The smallest lattice has only been used to outline the lattice phase diagram in figure 9. The simulations on the $12^3 \times 64$ lattice revealed an unexpected phase separation, where two or more phases with different properties coexisted. We will return to this phenomenon in section 5.6.

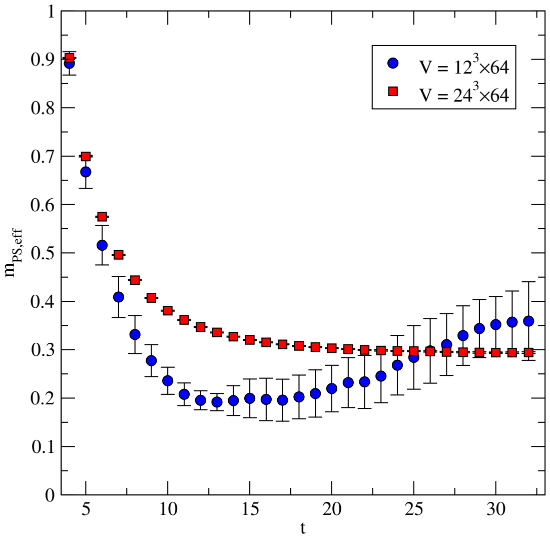

Figure 10: Effective mass of pseudoscalar meson for two different volumes. The parameters are $\beta = 7$ and $m_0 = -0.3$. This corresponds to $m_{\text{PCAC}} \simeq 0.2$.

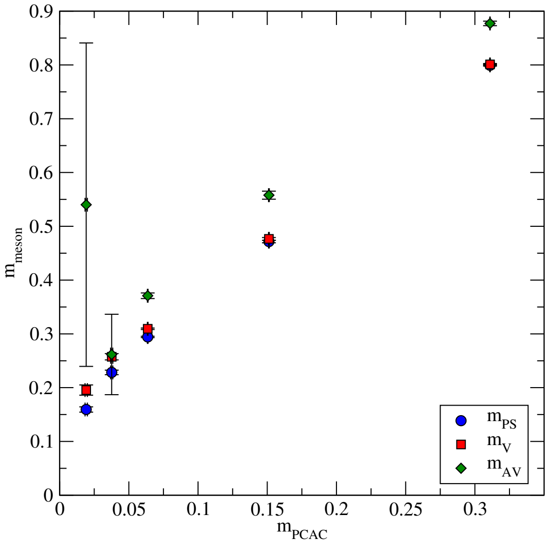

Figure 11: Pseudoscalar, vector, and axial vector meson masses measured on a $24^3 \times 64$ lattice at $\beta = 7$.

Results at fixed lattice spacing

The meson masses are estimated using time slice averaged zero momentum correlators of the kind (5.15). In figure 10 we have shown an example of how the effective mass plateau of the pseudoscalar meson looks when computed on $12^3 \times 64$ and $24^3 \times 64$ lattices keeping fixed the bare parameters. At the larger volume a mass plateau is easily identified and the pseudoscalar mass can be extracted fairly accurately. On the $12^3 \times 64$ the situation is different. There is a rise in the effective mass towards larger time separations. This is unexpected since all the heavier states will decay first and will therefore only dominate the correlators at small time separations. Due to this kind of odd behavior we restricted our spectrum analysis to the $24^3 \times 64$ data. A discussion concerning the unexpected $12^3 \times 64$ results will be given in section 5.6.

Figure 11 shows the pseudoscalar, vector and axial vector meson masses measured on the $24^3 \times 64$ lattice as m_0 is decreased towards the critical value. Clearly, the determination of the axial vector meson is very poor towards the chiral limit and we can not really conclude anything from this channel. More studies of this model is underway and hopefully this will allow a better determination of the axial vector mass. If the axial vector meson remains approximately degenerate with the vector meson deep in the chiral regime it could indicate walking dynamics. This originates from the second Weinberg sum rule being modified by the continuum contribution not relevant in ordinary QCD[64].

More precise are the measurements of the pseudoscalar and vector mesons. What can be

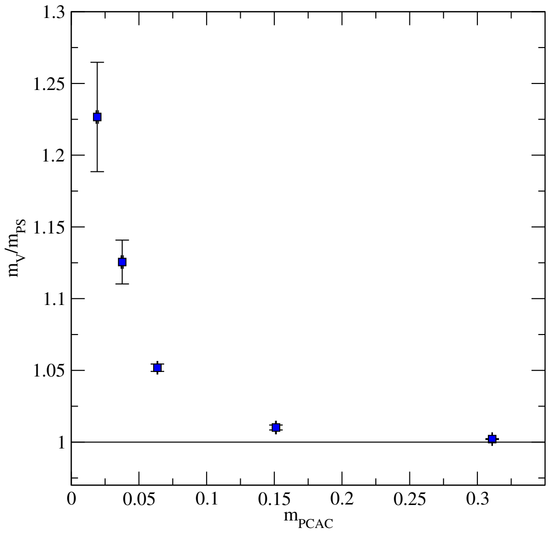

Figure 12: Ratio between pseudoscalar and vector meson masses measured on a $24^3 \times 64$ lattice at $\beta = 7$.

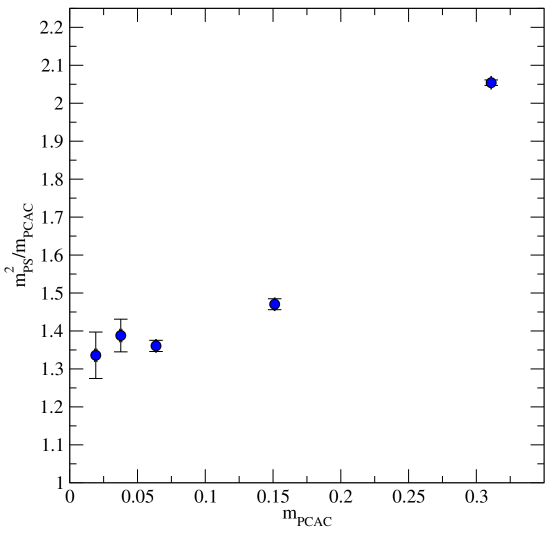

Figure 13: Psudoscalar mass squared divided by the quark mass measured on a $24^3 \times 64$ lattice at $\beta = 7$.

seen from figure 11 is that at large bare quark mass the vector and pseudoscalar is roughly degenerate and their masses are proportional to the quark mass. This is expected if the bare quark mass is the only scale or if it is dominant with respect to a dynamical mass scale. At small quark masses a significant mass splitting is observed indicating indeed the dynamical generation of a mass scale consistent with chiral symmetry breaking. This can be seen more clearly in figure 12 where the ratio m_V/m_{PS} is plotted. If a mass for the vector is generated dynamically this ratio should diverge in the chiral limit since the pseudoscalar is a Goldstone boson. Keep also in mind that, due to the identity (5.21), m_{PS} is exactly the same as the mass of the scalar diquarks which are also Goldstone bosons of the theory.

Another indication of a chiral symmetry breaking scenario can be found in the way the psudoscalar mass decreases with the quark mass. In section 3.3 we have already discussed the pseudoscalar mass in the chiral limit although for a different chiral symmetry breaking pattern. Neglecting chiral logs, which does not seem to play a role in this range of quark masses, the squared mass of the pseudoscalar is roughly proportional to the quark mass

$$m^2_{PS} \simeq \Lambda m_{PCAC}\,. \tag{5.24}$$

This is nothing but the GMOR relation (5.4).

In the case the model is only deformed from conformality by the quark mass, there is no dynamical scale available and we will expect the hyperscaling relations (3.17) to govern at low quark masses.

Meson fit	Fit function	Best parameter	χ^2/dof
PS ChSB	$a\sqrt{m}$	$a = 1.167(6)$	0.49/2
PS conformal	$Am^{\frac{1}{1+\gamma}}$, $\gamma = 1.1675$	$A = 1.047(7)$	4.19/2
PS alternative 1	$Am^{\frac{1}{1+\gamma}}$, γ free	$A = 1.17(5)$ $\gamma = 0.99(5)$	0.48/1
PS alternative 2	$a + b\sqrt{m}$	$a = -0.001(10)$ $b = 1.17(4)$	0.47/1
Vector ChSB	$a + bm$	$a = 0.16(1)$ $b = 2.3(2)$	3.3/1
Vector conformal	$Am^{\frac{1}{1+\gamma}}$, $\gamma = 1.1675$	$A = 1.105(10)$	9.25/2
Vector alternative	$Am^{\frac{1}{1+\gamma}}$, γ free	$A = 0.85(4)$ $\gamma = 1.71(12)$	0.31/1
Combined hyperscaling	$\propto m^{\frac{1}{1+\gamma}}$	$\gamma = 1.17(15)$	13.5/4

Table 5: Different types of fit functions in the chiral regime for the data with m identified with the m_{PCAC}.

Figure 13 shows a plot of the ratio $m_{\text{PS}}^2/m_{\text{PCAC}}$ as a function of m_{PCAC} and it shows that this ratio tends towards a constant in chiral limit. This is consistent with a chiral symmetry breaking scenario.

To further test the chiral symmetry breaking hypothesis we have performed some fits to the data in the chiral regime. By the chiral regime we are referring to measurements with quark masses below 0.1 in lattice units. Three data points are available in this regime. This particular choice of the extend of the fit region is motivated by the observations in figure 13. It shows that the points in this region is consistent with the GMOR relation (5.24). Note that in this region we have $f_{\text{PS}}L \simeq 0.8 - 0.9$. Ideally this quantity should be larger.

In figure 14 the pseudoscalar and vector masses are displayed in the fit region and solid lines show the chiral fits. The hyperscaling fits (3.17) are shown in figure 15. Various fit types was compared and the results are shown in table 5. Attention should be paid to the "ChSB" and "conformal" fits. Looking at the pseudoscalar the ChSB fit, i.e. the GMOR relation (5.24), is clearly stronger than the "PS conformal" fit using the hyperscaling relations (3.17). Note that the anomalous dimension γ in the conformal fit is chosen as a best fit to both the pseudoscalar and vector meson data. The quality of the fit is determined from χ^2/dof, which will be small for good fits. We have also given a couple of alternative fit types. "PS alternative 1" allows a scaling function with γ being a free fit parameter. This fit has essentially the same χ^2 value as the chiral fit but only half the degrees of freedom. Notice also how γ is forced to ~ 1 by the fit recovering the functional form of the GMOR relation. In the last fit, "PS alternative 2", the mass

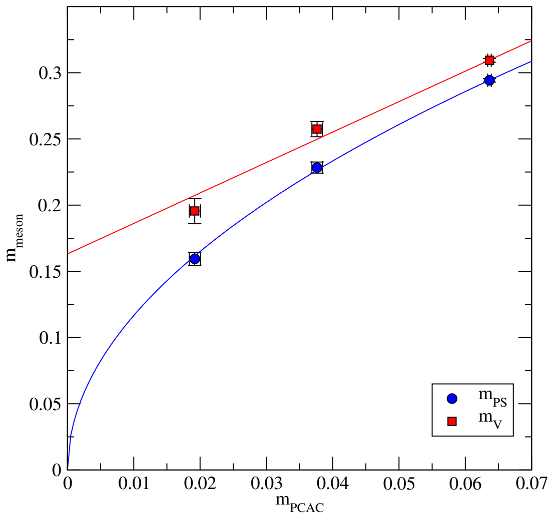

Figure 14: The ChSB fits to the pseudoscalar and vector meson masses on a $24^3 \times 64$ lattice at $\beta = 7$. For details of the fits see table 5.

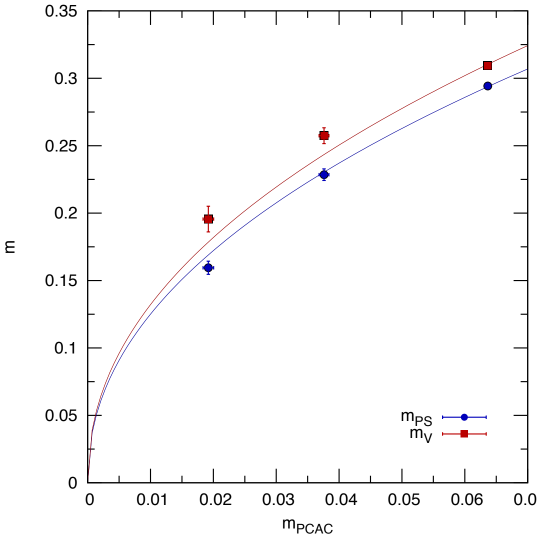

Figure 15: Fits to the pseudoscalar and vector meson masses on a $24^3 \times 64$ lattice at $\beta = 7$ using the hyperscaling hypothesis. For details of the fits see table 5.

in the chiral limit is not forced to zero. Remarkably the best fit demands the pseudoscalar mass to vanish in the chiral limit. This lends further confidence in the chiral symmetry breaking hypothesis.

The second part of table 5 summarizes the fit results for the vector meson. Also in this case is the "ChSB fit" favored over the conformal hyperscaling hypothesis. However, if we look at the data points in figure 14 they curve slightly making the "ChSB" fit a little less convincing. Considering the χ^2/dof values for the two fits stated in table 5 it is evident that to rule out any one of them, on the basis of the vector meson data, would be premature.

It is worth mentioning that if we let γ be unconstrained in the scaling fit, an excellent fit is achieved, but this would not be consistent with the universal hyperscaling expected in a mass deformed conformal model.

Having performed these fits we can also give a very rough estimate of the vector meson mass in physical units. From table 5 we see from the ChSB fit that $m_V = 0.16(1)$ in the chiral limit. This is given in lattice units. To fix the scale we can use the pseudoscalar decay constant f_{PS} which must take the value of the Higgs vacuum expectation value ~ 246 GeV. In lattice units we have measured $f_{PS} = 0.034(4)$ giving a ratio $m_V / f_{PS} = 4.71 \pm {}^{0.96}_{0.76}$. This means that the mass of the vector in physical units will be

$$m_V = 1.2 \pm {}^{0.3}_{0.2}\,\text{TeV}.$$

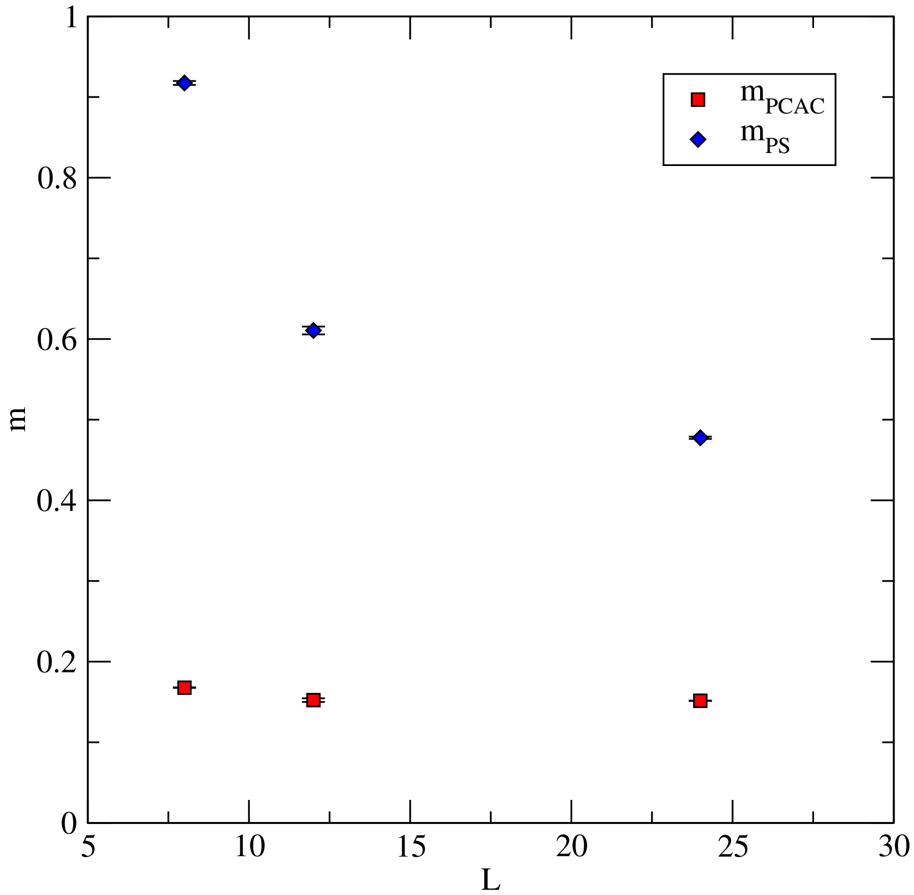

Figure 16: Finite size effects on m_{PS} and m_{PCAC} in units of inverse lattice spacing. The measurements are performed on a $24^3 \times 64$ lattice at $\beta = 7$ and $m_0 = -0.2$.

It can not be stressed enough, that this number is very uncertain. The errors stated are just the uncertainties of the fit values. No estimate of the size of the finite volume effects has been taken into account and no continuum extrapolation has been performed. Therefore, the strongest justifiable statement is that it can not be excluded that the model admits a vector meson as light as 1.2 TeV.

5.6 FINITE SIZE EFFECTS

In this model there are two separate issues concerning finite size effects that need to be addressed. Like in other lattice gauge theories, we can expect a mass shift as a consequence of the finite size of the system. This was the subject of section 3.1. The finite volume effects can be quite sizable in SO(N) gauge theories. This is because the bulk phase transition occurs at weak coupling meaning that the lattice spacing corresponds to very small physical length.

Besides this effect we also observe a phase separation phenomenon taking place in all lattice simulations smaller than our biggest volume $24^3 \times 64$. Two or more phases coexist on the the lattice and they are separated by domain walls. These phases have different properties such as correlation lengths and Polyakov loop expectation values. This causes the unexpected rise in the effective mass plateaus of the mesons as seen in figure 10.

First we will discuss the finite volume mass shifts relevant for our measurements of the spectrum. It has been difficult to really estimate the size of the mass shifts still present in our data on the $24^3 \times 64$ lattice data. This is because the smaller volumes are affected by the phase separation phenomenon. However, in the data from *one* of the simulations at $12^3 \times 64$, the rise in the effective mass plateau was not observed, so we seize the opportunity to use this dataset to provide estimates for the mass shifts. The bare parameters of the data set is $\beta = 7$ and $m_0 = 0.2$ corresponding to $m_{\text{PCAC}} \simeq 0.15$. Of course we would ideally like to do this measurement at smaller quark mass, but this happened to be the only mass where the analysis was possible.

The smallest lattice volume $8^3 \times 16$ does not have long enough temporal extend for any rise in the mass plateau to show up or for any plateau to appear in the first place. Consequently we have used the central effective mass point as the estimate for the pseudoscalar mass.

In figure 16 m_{PS} is plottet for the three lattice sizes available. If one tries to fit a function of the form

$$m_{\text{PS}}(L) = m_{\text{PS}} + A\frac{e^{-m_{\text{PS}}L}}{\sqrt{m_{\text{PS}}L}}, \tag{5.25}$$

in correspondence with the discussion in section 3.1, one will find that the fit is not convincing. However, as was also discussed in section 3.1, other groups have found deviations from the asymptotic formula (3.11). In our case the reason might simply be that the $8^3 \times 16$ mass measurement was still affected by heavier states in the same channel due to the short temporal extent. At any rate, we have included an additional parameter in the fit in order to accommodate the data. The fit now looks like

$$m_{\text{PS}}(L) = m_{\text{PS}}\left(1 + A\frac{e^{-Bm_{\text{PS}}L}}{\sqrt{Bm_{\text{PS}}L}}\right), \tag{5.26}$$

where A, B and m_{PS} are fit parameters. Note that there are no freedom left in the fit. The coefficients are determined to

$$A = 7.385, \qquad B = 0.483 \qquad m_{\text{PS}} = 0.464. \tag{5.27}$$

Based on this fit, we can conclude that in order to get a mass shift of less than 5 % we must have $m_{\text{ps}}L \gtrsim 8.8$. For 10 % it would be $m_{\text{ps}}L \gtrsim 7.6$. If we are to take this seriously it would mean that all points with a pseudoscalar mass less than about ~ 0.36 in lattice units would have finite size corrections of 5 % or more. This includes the entire range of masses used in the chiral fits. It is possible, based on the above fit, to make infinite volume extrapolations in the chiral regime. However, since this fit is based on data from three simulations where two are known to be problematic, it would be unsound to promote this to a universal prescription for the infinite volume correction. We therefore await more results on bigger lattices in order to properly asses the finite volume mass shifts.

Domain walls

It is well known that the Polyakov loop can acquire a non-zero expectation value is the lattice becomes too small. The definition of the Polyakov loop in dimension μ is

$$l_\mu = \frac{1}{N_c} \mathrm{Tr}\, L_\mu(\mathbf{x}_{\perp\mu}), \tag{5.28}$$

where

$$\begin{aligned} L_\mu(\mathbf{x}_{\perp\mu}) &= \mathrm{P}\exp\left[-\int_0^{1/(aL_\mu)} dx_\mu A^a_\mu(\mathbf{x}_{\perp\mu} x_\mu)\tau^a\right] \\ &= \prod_{x_\mu} U_\mu(\mathbf{x}_{\perp\mu}, x_\mu). \end{aligned} \tag{5.29}$$

However, we observe the coexistence of more than one phase on the same 4-volume. These phases are separated by domain walls and differs in this respect from the so called femto-world regime[65, 66, 67] of SU(N) models. As mentioned earlier, this unexpected phenomenon was first indicated to us by the unusual behavior of the mesonic correlators. Figure 10 shows an example of this. This motivated the resolution of the average Polyakov loop to each timeslice. In detail, the operators are

$$L_k(t) = \left\langle \frac{1}{N_i N_j} \sum_{x_i, x_j} \frac{1}{N} \mathrm{Tr} \prod_{x_k} U_k(t, \mathbf{x}) \right\rangle, \tag{5.30}$$

where $i \neq j \neq k$ are spatial directions. The phenomenon can be seen in figure 17a which shows the time resolved Polyakov loops on a $12^3 \times 64$ lattice at $\beta = 7$ and $m_0 = -0.3$. To illustrate the difference from the small volume phase in SU(N) models we have in figure 17b shown the time resolved Polyakov loop in an SU(2) pure gauge theory on a $12^3 \times 64$ lattice. The coexistence of two phases in the SO(4) simulations with different values of L_2 is clear from the figure. The two phases are long-lived and do not move inside the 4-volume of the lattice during the simulation. The phenomenon appears in all simulations performed on small lattices. The location of the phase boundaries and the direction in which the Polyakov loop has non-zero average is random. In some cases more than two phase boundaries appear in the same system. Notice also

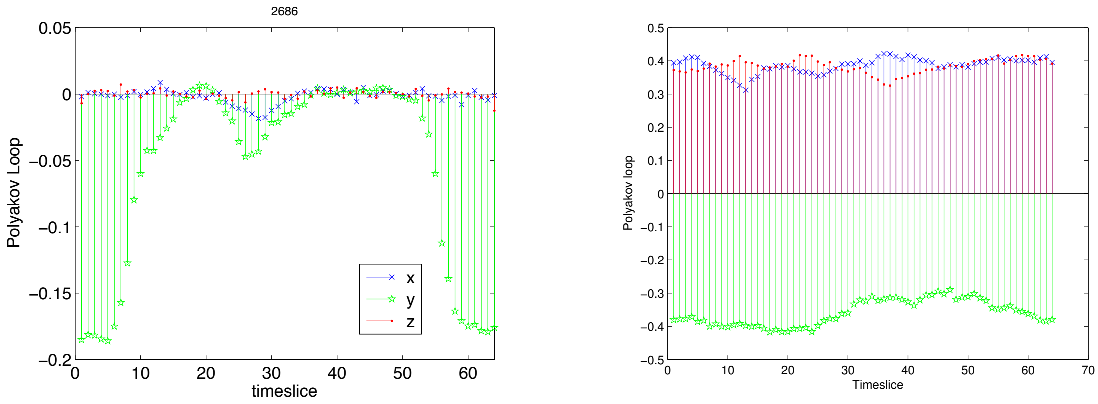

(a) SO(4) gauge theory with two Wilson fermions on a $12^3 \times 64$ lattice at $\beta = 7$ and $m_0 = -0.3$. The values are averages over 700 configurations starting at 1800 where the system does not appear to thermalize further.

(b) SU(2) pure gauge theory on a $12^3 \times 64$ lattice at $\beta = 6$

Figure 17: Average Polyakov loops wound around the three spatial dimensions computed at each timeslice of the lattice.

that in one of the two phases the average value of the Polyakov loop vanishes. To make sure that the domain walls we are seeing are actually walls traversing the entire 3-volume and not just bubbles, we have also resolved the Polyakov loop in two of the three spatial volume. The result can be seen in figure 18. The configurations are the same as the ones used to produce figure 17a as well as the odd looking mass plateau in figure 10. The two spatial directions in the plot is the ones orthogonal to the direction of the Polyakov loop observed to have non-zero expectation value in some range.

To better understand how these phases affect the correlators we have reanalyzed the configurations of 17a as well as the odd looking mass plateau in figure 10. In the procedure we usually employ to compute the correlators, the source is placed at a random timeslice. Figure 19a shows the pseudoscalar and vector meson correlators computed instead from a fixed source at timeslice 20. After the decay of excited states we observe a constant decay rate, i.e. constant effective mass, until about 35 timeslices from the source. Here the decay rate suddenly increases. This behavior continues after the inflection point. Counting 35 timeslices on top of 20 gives 55. In figure 17a we see that the phase boundary is indeed located at timeslice 55.

Figure 19b shows the the derivative of the log of the correlator in 19a. In the region immidiately around the inflection point of the correlator this quantity has no physical meaning. Away from the inflection point of the correlator, this quantity measures the exponential decay rate of

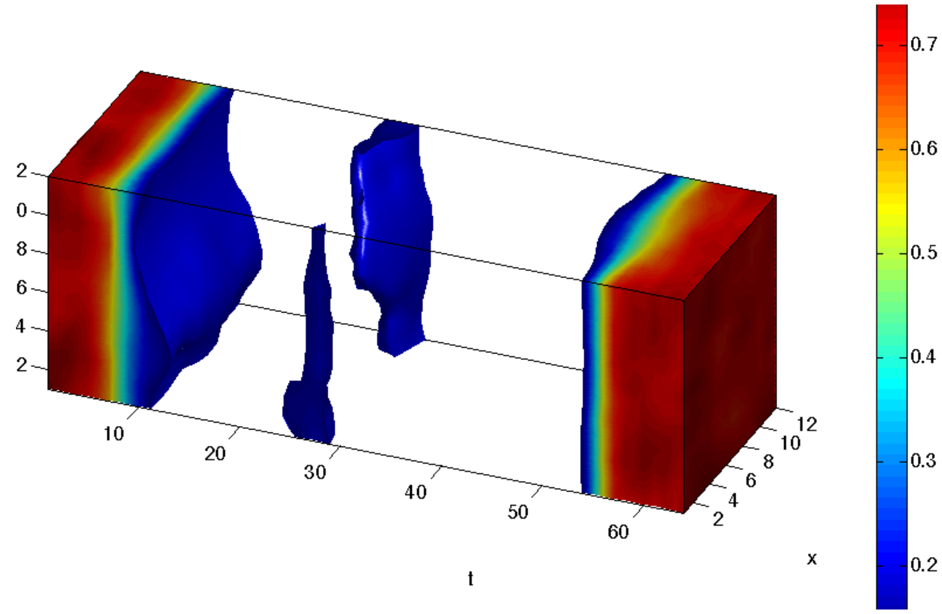

Figure 18: Local Polyakov loop along the y-direction averaged over 500 Monte Carlo updates. Resolving the volume orthogonal to the y-axis in the data for the $12^3 \times 64$ lattice at $\beta = 7$ and $m_0 = -0.3$.

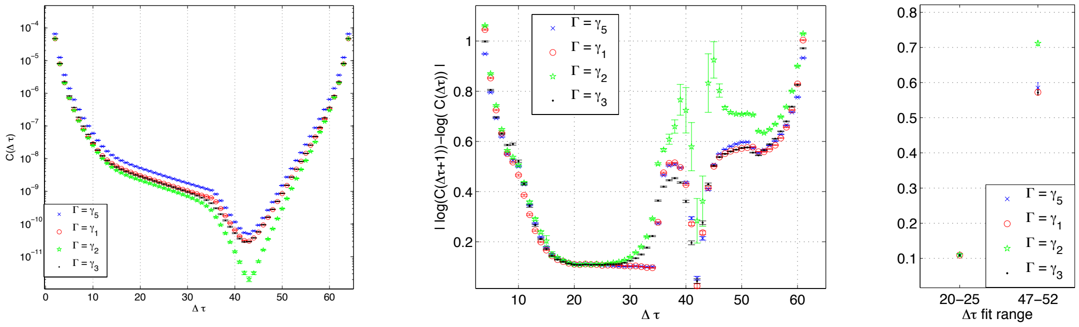

(a) Mesonic correlators.

(b) Effective mass plateaus.

(c) Mass fits in distinct temporal intervals.

Figure 19: Using a fixed source at timeslice $\tau = 20$ for calculating the mesonic $\bar{q}\Gamma q$ correlators on a $12^3 \times 64$ lattice at $\beta = 7$ using a bare mass $m_0 = -0.3$. The norm of the slopes of the correlation functions in (a) is depicted in (b) and is an estimate of the meson masses in the regions away from the inflection point and away from the edges of the $\Delta\tau$ interval. Figure (c) shows a fit to two of such regions.

the correlator i.e. the effective mass.

The figure reveals two mass plateaus, one before $\Delta\tau \simeq 35$ and one after. Figure 19c shows the best fit to the spectrum in these regions. The spectrum in the phase $\langle l_y \rangle \simeq 0$ is very light and it appears that the pseudo scalar and the vector mesons are all approximately degenerate. In the $\langle l_y \rangle \neq 0$-phase the spectrum is much heavier and interestingly there is a mass splitting among the vector mesons. Clearly, such a mass splitting is unphysical.

A relevant question at this point is if the $\langle l_y \rangle \simeq 0$ phase is related to the continuum physics. The answer to this question is probably no. Comparing the spectrum with that measured on the bigger lattice, $24^3 \times 64$, we see that there is a clear disagreement. The mesonic states are heavier on the bigger lattice, where so far we see no sign of the formation of domain walls.

Notice that, even though all the figures 17a, 10, 18,19 relating to the phase separation phenomenon was based on the same simulation, the observations were similar in all simulations performed on the $12^3 \times 64$ lattices and smaller.

Evidently, the correlation functions measured on these lattices cannot be used to extract the physical spectrum of the model.

SU(3) Sextet Minimal Walking Technicolor with Wilson fermions

6

The work presented in this chapter is unpublished and done in collaboration with my supervisors and Dr. Luigi Del Debbio, Edinburgh University.

6.1 STRONG COUPLING EXPANSION

Motivation

The treatment of the SU(3) lattice gauge theory with a doublet of Wilson fermions will be started with some analytical calculations in the strong coupling regime. Although this model has been studied by other groups in the past[68, 69, 70, 71] the use of this particular lattice action is new. We use the HiRep[43] code to conduct our investigations. On the bigger lattices the GPU enabled version was deployed. Facing a new model it is always comforting to have some analytical predictions which can act as a sanity check for the implementation. Various checks of each component of the code can be, and of course has been, performed. However, it is desirable to be able to compare actual observables in a regime accessible to analytical calculations and make quantitative comparisons.

In this section a strong coupling expansion is worked out where the fermion action is neglected. Since the gauge action is identical to that of ordinary QCD, this calculation has already found its way into the textbooks[26]. It is retained in this thesis in order to set up the notation, which will be useful when the fermions are taken into account. The effect of fermions are taken into account through an expansion in the Hopping parameter. Since the fermions are in the sextet representation the Hopping parameter expansion will give rise to a sextet plaquette term in the effective action. Consequently, when calculating observables, the combined expansion will give rise to non-trivial mixed terms.

For our purposes the plaquette expectation value will be good since it is simple to calculate both numerically and analytically. The analytical calculations will be presented in quite some detail since the somewhat formal approach allows for easy generalization to other gauge theories with Wilson fermions in higher representations.

Introduction

The action is defined as

$$S = S_G + S_F\,, \tag{6.1}$$

where

$$S_F = -\sum_{A,B} \bar{q}_A(n) K_{nA,mB}[U_R]\, q_B(m)\,, \tag{6.2}$$

is the Wilson fermion action and will be ignored in this section. The gauge action reads

$$S_G = \beta \sum_P \left(1 - \frac{1}{2N_c} \mathrm{Tr}\left[U_{\mu\nu} + U_{\mu\nu}^\dagger\right]\right). \tag{6.3}$$

From this point on N_c will be put to 3 explicitly. The partition function is

$$Z(\beta) = \int [dU]\, e^{-S_G}\,. \tag{6.4}$$

The plaquette expectation value is

$$\langle P \rangle = \frac{1}{3} \frac{\int [dU]\, \mathrm{Tr}(U_p) e^{-S_G}}{\int [dU]\, e^{-S_G}} \tag{6.5}$$

Character expansion

The first constant in (6.3) is of no importance and will just factor out in the partition function. Therefore it will be omitted from now on. Then

$$e^{-S_G} = e^{-\sum_p S_p} = e^{\sum_p \frac{\beta}{6} \mathrm{Tr}\left[U_p + U_p^\dagger\right]} \tag{6.6}$$

Clearly, if $\beta \to 0$ then $e^{-S_p} \to 1$. It is possible to be more precise by doing a character expansion

$$e^{x\mathrm{Tr}[U+U^\dagger]} = N(x) \sum_r d_r A_r(x) \chi_r(U) = N(x) \left(1 + \sum_{r\neq 0} d_r A_r(x) \chi_r(U)\right). \tag{6.7}$$

r runs over the irreducible representations of the gauge group. The character $\chi_r(U)$ is just the trace over U in representation r. x is just a shorthand for $\beta/6$ and is the natural expansion parameter. $N(x)$ and $A_r(x)$ are coefficients of the expansion. The characters are orthonormal.

$$\int [dU]\,\chi_r(U)\chi^*_{r'}(U) = \delta_{r,r'}\,, \tag{6.8}$$

where $\chi_{r^*}(U) = \chi^*_r(U) = \chi_r(U^\dagger)$ if r^* and r are conjugate representations. For SU(2) and U(1) there are closed form expressions for the coefficients $N(x)$ and $A_r(x)$. For SU(3) this is not the case. However, the coefficients are known to arbitrarily high orders in x and can be found in [72]. Letting a representation be denoted by two integers $r = (\lambda, \mu)$ related to the Young tableau, the relevant formulae goes

$$d_{(\lambda,\mu)} = \frac{1}{2}(\mu+1)(\lambda+1)(\mu+\lambda+2)\,, \tag{6.9}$$

$$\Gamma^k_r(x) = \sum_{n=0}^{\infty}\sum_{m=0}^{n} \frac{2^{m+1}(3n+3r+3)!\,x^{m+2n}}{m!(n-m)!(n+r+1)!(k+n+r+2)!(m+2n+3r+3)!}\,, \tag{6.10}$$

$$N(x) = \Gamma^0_0(x) \tag{6.11}$$

$$\begin{aligned} A_{(\lambda,\mu)}(x) = {} & \frac{1}{N(x)} x^{(\lambda+\mu)} \sum_{s=0}^{\mu} s! \binom{\lambda}{s}\binom{\mu}{s} \sum_{k=0}^{\lambda+\mu-2s} \binom{\lambda+\mu-2s}{k} x^{\lambda+\mu-2s-k} \\ & \times \sum_{r=0}^{2k+s} \binom{2k+s}{r} x^{2r}\,\Gamma^{k+s}_{\lambda+\mu+r-k-s}(x)\,. \end{aligned} \tag{6.12}$$

The most important thing to notice here is the fact that the lowest power of x in $A_{(\lambda,\mu)}(x)$ is $x^{\lambda+\mu}$ and that $N(x) \to 1$ for $x \to 0$.

The partition function can now be written as

$$Z(x) = \int [dU] \prod_p N(x)\left(1 + \sum_{r\neq 0} d_r A_r(x)\chi_r(U_p)\right) \tag{6.13}$$

where $x = \beta/6$. Let Ω denote the 4-volume of the lattice (the total number of lattice sites). Then we can rewrite the above

$$Z(x) = N(x)^{6\Omega}\left(1 + \int [dU] \sum_{\mathcal{G}} \prod_{p\in|\mathcal{G}|} d_{r_p} A_{r_p}(x)\chi_{r_p}(U_p)\right). \tag{6.14}$$

Now $\mathcal{G}$ denotes a *graph* which is a mapping from every plaquette p in the lattice to a representation r_p. $|\mathcal{G}|$ denotes the support of $\mathcal{G}$ i.e. all the plaquettes which does not map to the singlet representation. Here we are not going to spend time evaluating all the contributions to the partition function, but we have to make a few observations and simplifications.

- $N(x)^{6\Omega}$ is gauge-independet and factorizes in the partition function. If we want to compute the free energy at some point we will have to include it, but for explicit evaluations of expectation values such as (6.5) we can omit it.

- The 1 is the contribution from the trivial path mapping all plaquettes to the singlet representation. This could be included instead in $\sum_{\mathscr{G}}$.

The partition function to $\mathscr{O}\left((\beta/6)^{10}\right)$

When computing the partition function as and expansion in $x = \beta/6$ the first contributions are easy to find. Clearly the only graphs that survive the group integrals comes from closed surfaces. The smallest one being an elementary cube. Since the lowest order in $x = \beta/6$ in the coefficients $A_{(\mu,\lambda)}(x)$ are $x^{\mu+\lambda}$ the cube with fundamental $(\mu,\lambda) = (1,0)$ plaquettes comes with a factor of x^6 which will be the leading order. In fact the contribution is easy to evaluate.

$$Z(x) = 1 + 4\Omega d^2_{(1,0)} \left(A_{(\mu,\lambda)}(x)\right)^6 + \mathscr{O}\left(x^{10}\right). \tag{6.15}$$

The 4 comes from the possible orientations of the cubes. $d^2_{(1,0)}$ comes from the gauge integration and tracing. To be more explicit we could insert the expansion

$$A_{(1,0)}(x) = \frac{x}{3} + \frac{x^2}{6} - \frac{5x^4}{72} - \frac{x^5}{24} + \frac{7x^6}{720} + \mathscr{O}\left(x^7\right). \tag{6.16}$$

so

$$Z(x) = 1 + 4\Omega d^2_{(1,0)} \left(\frac{x}{3}\right)^6 + \mathscr{O}\left(x^{10}\right). \tag{6.17}$$

Note that to order x^{12} we would have a contribution from the expansion of $\left(A_{(1,0)}(x)\right)^6$ as well as paths with 12 fundamental plaquettes (e.g. two disconnected cubes). On top of this we would have a contribution from unit cubes covered with plaquettes in the adjoint $(1,1)$ and sextet $(2,0)$ representation and even $(1\times 1\times 2)$-cubes with higher representation inner wall. This will not be considered here. Instead we consider the order x^{10} contribution which only comes from the $(1\times 1\times 2)$-cubes. There are 36 different orientations of these pr. site so the contribution becomes

$$36\Omega d^2_{(1,0)} \left(A_{(\mu,\lambda)}(x)\right)^{10}.$$

This last contribution is really not that important, it was just to outline the method with which one would proceed to higher orders. The point of this detour is to convince ourselves that up to order x^5 we do not need to worry about the denominator when computing expectation values like in (6.5).

Plaquette expectation value to $\mathcal{O}\left((\beta/6)^4\right)$

We can go about calculating this in two different ways. At this point the simplest way is to calculate the free energy and then differentiate with respect to β. This would go as follows:

$$F = -\ln Z \tag{6.18}$$

so

$$\langle P\rangle = -\frac{1}{6\Omega}\frac{dF}{d\beta}.$$

Here the most important part of the partition function is the factor $N(\beta/6)^6$. The explanation for this is not trivial. Since at higher powers of β there will be more and more disconnected contributions to the partition function (6.14) it will also contain higher and higher powers of Ω. The only way the free energy can be proportional to Ω (for large Ω) is if all the powers of Ω exponentiates. It can be shown explicitly that this is indeed the case. To find the exponent we can just look at the terms linear in Ω in the β-expansion (6.15). This term will be a series in $\beta/6$ starting at order $(\beta/6)^6$. Therefore the free energy will be

$$F = -6\Omega \ln N(\beta/6) + \mathcal{O}\left((\beta/6)^6\right) \tag{6.19}$$

This means that up to $\mathcal{O}\left((\beta/6)^6\right)$ we can get the free energy from the expansion

$$N(x) = 1 + x^2 + \frac{x^3}{3} + \frac{x^4}{2} + \frac{x^5}{4} + \mathcal{O}\left(x^6\right). \tag{6.20}$$

Note also that

$$\frac{d\ln N(\beta/6)}{d\beta} = A_{(1,0)}(\beta/6) \tag{6.21}$$

so

$$\begin{aligned}\langle P\rangle &= -\frac{1}{6\Omega}\frac{dF}{d\beta}\\ &= A_{(1,0)}(\beta/6) + \mathcal{O}\left((\beta/6)^5\right)\\ &= \frac{\beta}{18} + \frac{\beta^2}{216} - \frac{5\beta^4}{93312} + \mathcal{O}\left((\beta/6)^5\right).\end{aligned}$$

Note that we do in fact have enough information to proceed to $\mathcal{O}\left((\beta/6)^9\right)$ in the plaquette.

Now I will perform the calculation explicitly through formula (6.5). That is

$$\begin{aligned}\langle P\rangle &= \frac{1}{3}\frac{\int [dU]\,\mathrm{Tr}(U_p)e^{-S_G}}{\int [dU]\,e^{-S_G}} &(6.22)\\ &= \frac{1}{3}\int [dU]\,\mathrm{Tr}(U_{p'})\sum_{\mathcal{G}}\prod_{p\in|\mathcal{G}|} d_{r_p}A_{r_p}(x)\chi_{r_p}(U_p) + \mathcal{O}\left((\beta/6)^6\right). &(6.23)\end{aligned}$$

Notice that since $\chi_{(1,0)}(U_{p'}) = \mathrm{Tr}(U_{p'})$ we can use the orthogonality relations to reduce the number of graphs we need to consider. The simplest contribution is the graph only supported on p' mapping p' to the (anti-)fundamental representation. The next simplest kind of path is the ones supported on a box opened at plaquette p'. These will contribute only at order $(\beta/6)^5$, so we can write

$$\begin{aligned}\langle P\rangle &= \frac{1}{3}\int dU_p \chi_{(1,0)}(U_p) d_{(0,1)} A_{(0,1)}(x) \chi^*_{(1,0)}(U_p) + \mathcal{O}\left((\beta/6)^5\right)\\ &= A_{(1,0)}(\beta/6) + \mathcal{O}\left((\beta/6)^5\right).\end{aligned}$$

where we have used the fact that $A_{(1,0)} = A_{(0,1)}$. The result is the same as before. Remarkably the only term that mattered in this calculation was the one we neglected in the free energy calculation and the only term that mattered there could be disregarded in this calculation. This is a consequence of (6.21).

Both methods have their uses. The second one will probably be more handy when including the fermions and expanding also in the Hopping parameter κ.

6.2 HOPPING PARAMETER EXPANSION

Integrating out the fermions we can write the effective action

$$S_{\text{eff}} = S_G - \ln\det K.$$

The fermion matrix K can be written as $1 - \kappa M$ where.

$$M[U]_{x,y} = \sum_\mu \delta_{x,x+\mu}(r + \gamma_\mu) U^{(R)}_\mu(x).$$

The sum over μ goes both backwards and forwards in all 4 dimensions. In this notation $\gamma_{-\mu} = -\gamma_\mu$, r is the Wilson parameter and $U^{(R)}$ is the gauge link in representation R of the fermions. We can rewrite $\ln\det K = \mathrm{Tr}\ln K$ and expand in the Hopping parameter $\kappa = \frac{1}{2m+8}$.

$$\begin{aligned}\mathrm{Tr}\ln K &= -\sum_{l=2}^{\infty}\frac{\kappa^l}{l}\mathrm{Tr}\left(M^l\right)\\ &= \text{const.} + 8\kappa^4 N_f(1 + 2r^2 - r^4)\sum_P \mathrm{Tr}\left[U^{(R)}_p + U^{(R)\dagger}_p\right] + \mathcal{O}(\kappa^6).\end{aligned} \tag{6.24}$$

The trace is over both colour, flavour and spin indices. Now we will derive the above $\mathcal{O}(\kappa^4)$ expansion in detail.

Due to the sparse structure of M we can write

$$\mathrm{Tr}\left(M^l\right) = N_f \sum_{\{x_i,\mu_i\}\in\mathcal{C}_l} \mathrm{Tr}_c\left(\prod_{i=1}^{l} U^{(R)}(x)_{\mu_i}\right)\mathrm{Tr}_s\left(\prod_{j=1}^{l}(r + \gamma_{\mu_j})\right). \tag{6.25}$$

$\mathscr{C}_l$ denotes all directed closed paths of length l. Some paths should be counted multiple times since the same path can be started at every lattice point on its route. Clearly for $l = 2$ there is only one kind of closed path that can contribute. Namely directly back and forth. There are 8 directions from each lattice site in which one can start the path. Thus the contribution becomes

$$\begin{aligned} \mathrm{Tr}\left(M^2\right) &= N_f \Omega 8 \mathrm{Tr}_c\left[U^{(R)} U^{(R)\dagger}\right] \mathrm{Tr}_s\left[(r+\gamma_\mu)(r-\gamma_\mu)\right] && (6.26) \\ &= N_f \Omega 8 d_R 4 (r^2-1)\,. && (6.27) \end{aligned}$$

So if $r = 1$, which is a common choice, this contribution vanishes. This is true for all paths involving a backtracking of a link since, as was the case here, they will introduce a factor of (r^2-1) through the spin trace. The next order i.e. $l = 4$ has two different kind of contributions. There is the plaquette along with some backtracked paths.

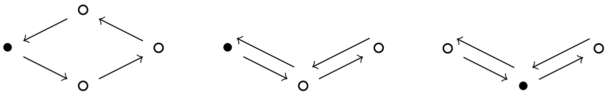

The filled circle in the above diagrams represent the lattice point from which the path originates. This can help the counting. Clearly, the second and third diagram have similar contributions. The multiplicity of the second diagram will be $8 \cdot 7$. For the third diagram it will be $8 \cdot 8$. In total we should count this diagram 120 times pr. site. Therefore we get

$$N_f \Omega 120 d_R 4 (r^2-1)^2\,. \tag{6.28}$$

The plaquette term is the first non-trivial term in the Hopping parameter expansion (HPE). The multiplicity is $8 \cdot 6$ pr. site. Normally when summing over plaquettes we count 6 plaquettes pr. site. This means that each plaquette enters 8 times in this contribution. The contribution therefore becomes

$$\begin{aligned} &N_f 8 \sum_p \mathrm{Re}\,\mathrm{Tr}_c U_p^{(R)} \mathrm{Tr}_s\left[(r+\gamma_\mu)(r+\gamma_\nu)(r-\gamma_\mu)(r-\gamma_\nu)\right] \\ &= N_f 8 \cdot 4 (r^4 - 2r^2 - 1) \sum_p \mathrm{Re}\,\mathrm{Tr}_c U_p^{(R)}\,. \end{aligned}$$

Taking the real part of the plaquette is justified since each plaquette enters with both directions in the computation.

Now we are ready to collect the contributions up to order κ^4

$$\begin{aligned}\mathrm{Tr}\ln K &= -\sum_{l=2}^{\infty}\frac{\kappa^l}{l}\mathrm{Tr}\left(M^l\right)\\ &= -\kappa^2 N_f\Omega 16 d_R(r^2-1) - \kappa^4 N_f\Omega 120 d_R(r^2-1)^2 \\ &\qquad -\kappa^4 N_f 8(r^4-2r^2-1)\sum_p \mathrm{Re}\,\mathrm{Tr}_c U_p^{(R)} + \mathcal{O}\left(\kappa^6\right)\end{aligned} \tag{6.29}$$

This is the result from (6.24). Now we need to calculate the plaquette in the combined HPE and SCE.

6.3 PLAQUETTE EXPECTATION VALUE IN SCE AND HPE

From now on we will specialize to the case of $r = 1$ so

$$\mathrm{Tr}\ln K = \kappa^4 N_f 16\sum_p \mathrm{Re}\,\mathrm{Tr}_c U_p^{(R)} + \mathcal{O}\left(\kappa^6\right) \tag{6.30}$$

The calculation now goes like

$$\langle P\rangle = \frac{1}{3}\frac{\int [dU]\,\mathrm{Tr}(U_p)e^{-S_{\mathrm{eff}}}}{\int [dU]\,e^{-S_{\mathrm{eff}}}} \tag{6.31}$$

Notice that we still do not need to worry about the denominator of (6.31) since at order κ^4 this can be put to 1 for the same reason as in the SCE. One could again do a character expansion of $\exp(\mathrm{Tr}\ln K)$. However, since we are dealing with the trace of the represented plaquette, the expansion coefficients would not be the same. These coefficients could be worked out, but we will settle for the first term which is

$$\begin{aligned}e^{\mathrm{Tr}\ln K} &= \prod_p\left(1+\kappa^4 N_f 16\,\mathrm{Re}\,\mathrm{Tr}_c U_p^{(R)}\right) + \mathcal{O}\left(\kappa^6\right)\\ &= \prod_p\left(1+\kappa^4 N_f 8\left[\chi_R(U_p)+\chi_R^*(U_p)\right]\right) + \mathcal{O}\left(\kappa^6\right).\end{aligned}$$

Now inserting this into (6.31) and explicitly using the sextet representation for the fermions we get

$$\begin{aligned}\langle P\rangle = \frac{1}{3}\int [dU]\,\chi_{(1,0)}(U_{p'})\sum_{\mathcal{G}}\prod_{p\in|\mathcal{G}|} d_{r_p}A_{r_p}(\beta/6)\chi_{r_p}(U_p)\\ \times\prod_{p''}\left(1+\kappa^4 N_f 8(\chi_R(U_{p''})+\chi_R^*(U_{p''})\right) + \mathcal{O}\left(\kappa^6\right) + \mathcal{O}\left((\beta/6)^6\right)\end{aligned}$$

The above computation will simplify at this order since we can disregard non-minimal graphs. Notice also that the first term will be exactly the SCE plaquette expectation value

$$\begin{aligned}\langle P\rangle = \langle P\rangle_{\mathrm{SCE}} + \frac{\kappa^4 N_f 8}{3}\int dU\chi_{(1,0)}(U)\sum_r d_r A_r(\beta/6)\chi_r(U)\left(\chi_{(2,0)}(U)+\chi_{(2,0)}^*(U)\right)\\ +\mathcal{O}\left(\kappa^6\right)+\mathcal{O}\left((\beta/6)^5\right)\end{aligned}$$

From the above formula it is clear that in the case of higher representation fermions. We will not have any contributions at order $\kappa^4(\beta/6)^0$ which we would have for fundamental fermions. We can go to the next order, i.e $\kappa^4(\beta/6)^1$, by using the property of the characters

$$\chi_{r_1}(U)\dots\chi_{r_k}(U)=\sum_{\lambda}\chi_{\lambda}(u)\,,$$

where lambda goes over the irreducible representations contained in $r_1\otimes\cdots\otimes r_k$. In other words

$$\int dU\chi_{r_1}(U)\dots\chi_{r_k}(U) = \#\text{ of singlets}\,.$$

which gives us

$$\begin{aligned}\langle P\rangle &= \langle P\rangle_{\text{SCE}} + \frac{\kappa^4 N_f 8}{3}\int dU\chi_{(1,0)}(U)d_{(1,0)}A_{(1,0)}(\beta/6)\chi_{(1,0)}(U)\chi^*_{(2,0)}(U)+\text{h.o.}\\ &= \langle P\rangle_{\text{SCE}} + \kappa^4 N_f 8A_{(1,0)}(\beta/6)+\text{h.o.}\\ &= (1+\kappa^4 N_f 8)A_{(1,0)}(\beta/6)+\text{h.o.}\end{aligned}$$

where h.o. is a shorthand for $\mathcal{O}\left(\kappa^6\right)+\mathcal{O}\left((\beta/6)^5\right)+\mathcal{O}\left(\kappa^4(\beta/6)^3\right)$.

Now inserting the expansion of $A_{(1,0)}(\beta/6)$ we get

$$\langle P\rangle = (1+\kappa^4 N_f 8)\left(\frac{\beta}{18}+\frac{\beta^2}{216}-\frac{5\beta^4}{93312}\right)+h.o.. \tag{6.32}$$

We can try to compare our data with the calculations. This has been done in figure. 20, which shows lattice data in a region where good statistics on the plaquette was available and where the theoretical uncertainty (higher orders in $\beta/6$ and κ) does not exceed the κ^4-correction). The lattice data and the SCE+HPE expansion is clearly in agreement. The results are different from ordinary QCD with fundamental fermions, where the leading order Hopping parameter correction would be order zero in β and therefore be about ten times as big for $\beta \simeq 1.5$.

The agreement of the lattice data with the analytical calculations gives confidence in our lattice simulations and we can start probing regions not accessible with analytical methods.

6.4 BULK PHASE AND DELINEATION OF THE LATTICE PHASE DIAGRAM

The strong coupling expansion can actually capture many interesting properties of a lattice gauge theory, but since the expansion per construction is one on a coarse lattice (low β), we will need to abandon it to probe the continuum limit. At strong coupling the lattice is in a bulk phase which is not connected to the continuum. As we increase β a phase transition will be crossed where an abrupt rise in the plaquette expactation value occurs. At this point the strong

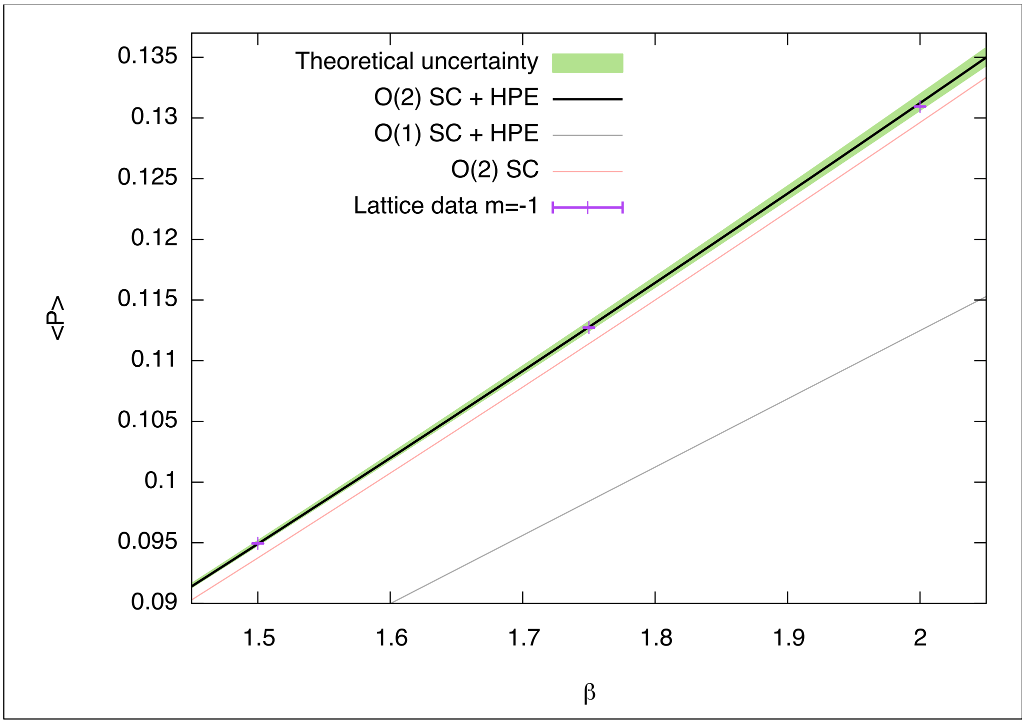

Figure 20: $m_0 = -1$ data for the plaquette zoomed in a region where good statistics on the plaquette was available and where the theoretical uncertainty (higher orders in $\beta/6$ and κ) does not exceed the κ^4-correction).

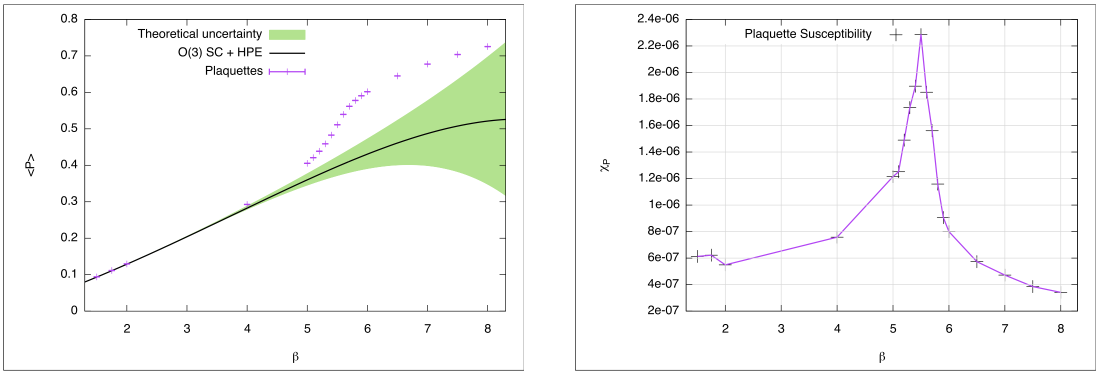

(a) Breakdown of the SC-HPE at the bulk phase transition.

(b) Bulk phase transition from peak in plaquette susceptibility.

Figure 21: Lattice data used to determine the location of the bulk phase transition at a fixed value of the bare mass $m_0 = 0$

coupling expansion breaks down as can be seen from figure 21a. In this model the transition is somewhat broad and the exact point of the transition is not conveniently read off. Better is it to look at the plaquette susceptibility χ_P (Fig. 21b) which peaks at the transition. This can be done for multiple values of the bare mass and in this way the bulk phase was outlined in the lattice phase diagram shown in figure 22.

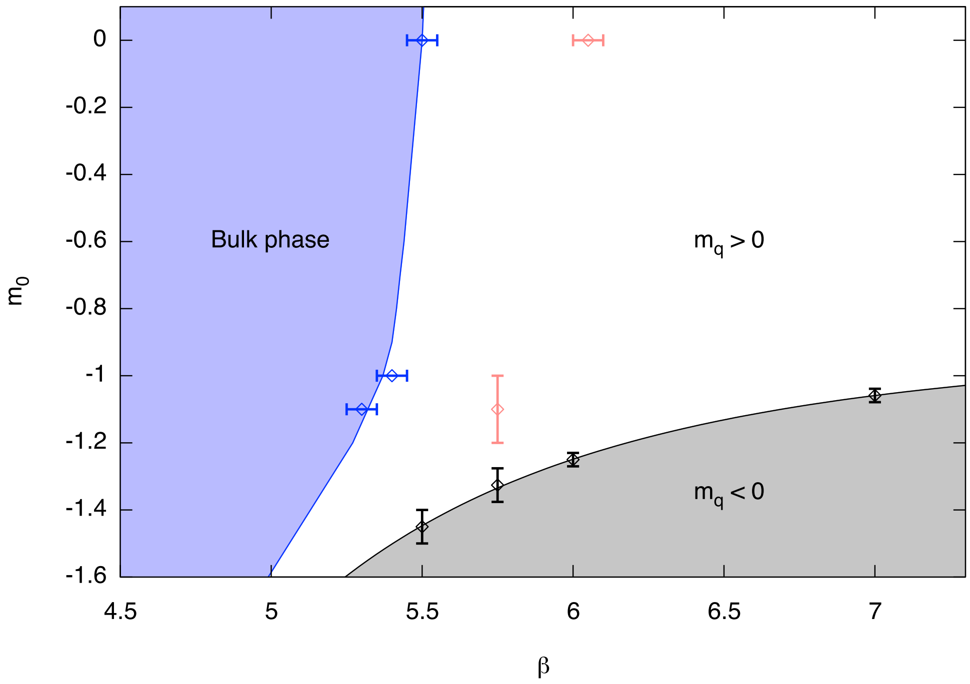

Figure 22: Phase diagram delineated on a 12^4 lattice. The red data points shows where the deconfinement phase transition has been detected. The red, blue and black points with errorbars reflect actual data whereas the lines are drawn with *free hand*.

In the phase diagram the deconfinement transition on a 12^4 lattice is also indicated by the red points. The errorbars are given by the distance between simulation points. An example of this can be seen from figure 23 where a scan in the bare mass was performed while holding fixed β at 5.75. A density plot in the complex plane of the Polyakov loops around all four directions is shown for each value of the mass. Clearly at the lowest bare mass, $m_0 = -1.2$ the $\mathbb{Z}_3$ center symmetry is broken, while for the highest masses it is not. At $m_0 = -1.1$ the density plot is clearly tending towards a more triangular shape and the same thing might even be hinted at $m_0 = -1.0$. In this case the conservative approach has been taken and the value indicated in the phase diagram spans the mass range from -1.2 to -1.

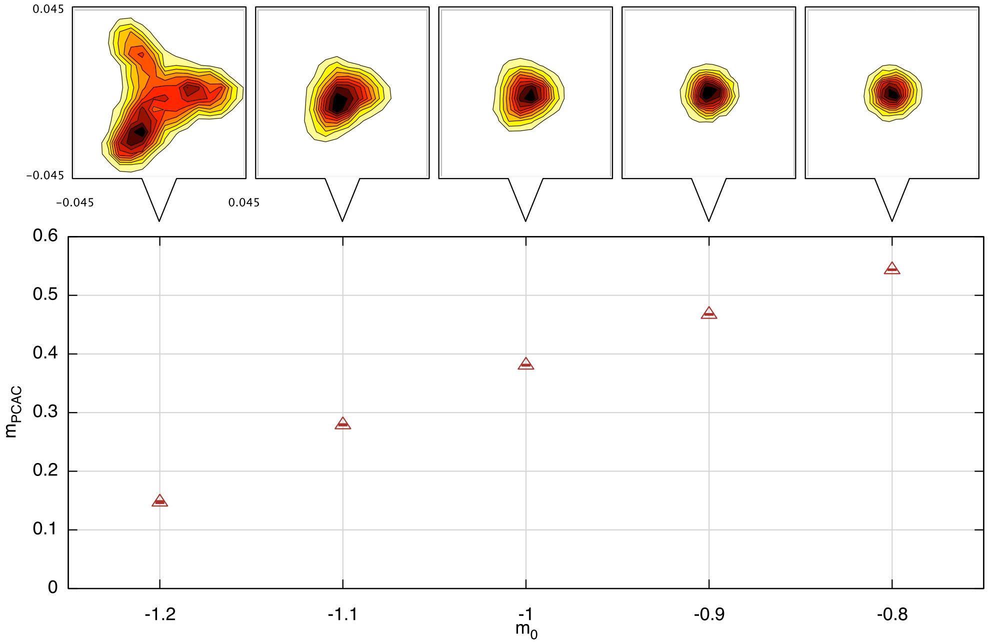

Figure 23: Data taken on a 12^4 lattice with $\beta = 5.75$ for the Polyakov loops around all directions mapped as a density plot at different values of the quark mass. The first 400 configurations out of a total of 3000 were discarded for the Polyakov loop plot.

6.5 THE SPECTRUM OF SU(3) SEXTET TECHNICOLOR

In this section we will present the numerical studies of the spectrum of the SU(3) lattice gauge theory with two Dirac flavors of Wilson fermions in the sextet (2-index symmetric) representation. This is a complex representation and therefore the assumed pattern of chiral symmetry breaking pattern is SU(2)⊗SU(2)→SU(2). This means that three Goldstone bosons would appear in the spectrum had the SU(2)⊗SU(2) global flavour symmetry been exact. Due to the explicit breaking by the non-zero quark mass we can expect pseudo Goldstone modes when the quark mass is decreased below the chiral scale of the theory. The discussion is somewhat similar to the one for SO(4) MWT except that there are no baryonic diquarks in the low energy spectrum. The three pseudo Goldstone bosons has the same form as the pseudoscalar *pions* in (5.13). In fact all of the mesons will have the same naive quark content as for SO(4) MWT, but since the Dirac operator no longer has the symmetry (5.1), i.e

$$(\not{D} + m)C\gamma^5 \neq C\gamma^5(\not{D} + m)^*, \tag{6.33}$$

the spectrum does not come in degenerate trios of two baryons and a meson.

Numerical simulations

For these studies we have used configurations generated using the HiRep[43] code. The configurations generated on small lattices below $L = 16$ has been generated with a CPU driven HMC algorithm and in some cases the RHMC algorithm. All configurations on bigger lattices are generated using a GPU accelerated version of HiRep which is described chapter 4. In this version the represented sextet gauge field was constructed on the fly from the fundamental gauge field. As for the case of the quaternion representation of SU(2) this was done to reduce the memory transfer to the GPU. In this case however the speedup is only about 15%. This is because the Dirac operator kernel spills memory from the registers, which introduces another bottleneck. Table 6 shows a listing of the simulations performed along with acceptance ratios and thermalization times. Note that in some cases the simulations were started from a configuration thermalized at another mass.

Volume	β	m	Iterations	Acceptance	Thermalization
$12^3 \times 12$	5	$[-1.5, 0]$	3000-5000	76%-84%	1000
$12^3 \times 12$	5.5	$[-1.2, 0]$	3000-5000	59%-85%	1000
$12^3 \times 12$	5.75	$[-1.2, -0.6]$	3000	78%-89%	1000
$12^3 \times 12$	6	$[-1.15, 0]$	3000	75%-84%	1000
$12^3 \times 12$	7	$[-1, 0]$	2000-5000	75%-83%	1000
$12^3 \times 12$	$[1.5, 7]$	0	3000-5000	76%-85%	1000
$12^3 \times 12$	$[1.5, 7]$	-1	2000-5000	66%-85%	1000
$12^3 \times 12$	$[4, 6]$	-1.1	1577-5000	75%-82%	1000
$16^3 \times 16$	6	$[-1.41, 0]$	2431-3460	88%-95%	1000
$16^3 \times 32$	5.75	$[-1.45, -1.3]$	2228-2631	84%-89%	1000
$16^3 \times 32$	5.75	$[-1.51, -1.475]$	932-1160	87%-92%	$500 - 700$
$16^3 \times 32$	6	-1.4	1672	91%	700
$20^3 \times 32$	6	-1.4	1524	88%	700
$24^3 \times 32$	6	-1.4	1299	90%	600

Table 6: Simulation parameters and typical values used for thermalization times and acceptance ratios. Brackets $[\cdot, \cdot]$ denote a scanned range in that particular parameter.

Results

As is can be seen from table 6, we have investigated the spectrum at two different lattice spacings. This will allow for a crude continuum extrapolation in the end. The figures 24, 25, 26, 27 , 28 and 29 summarize the results at two different lattice spacings, $\beta = 5.75$ and $\beta = 6$. We will return to the scale fixing shortly.

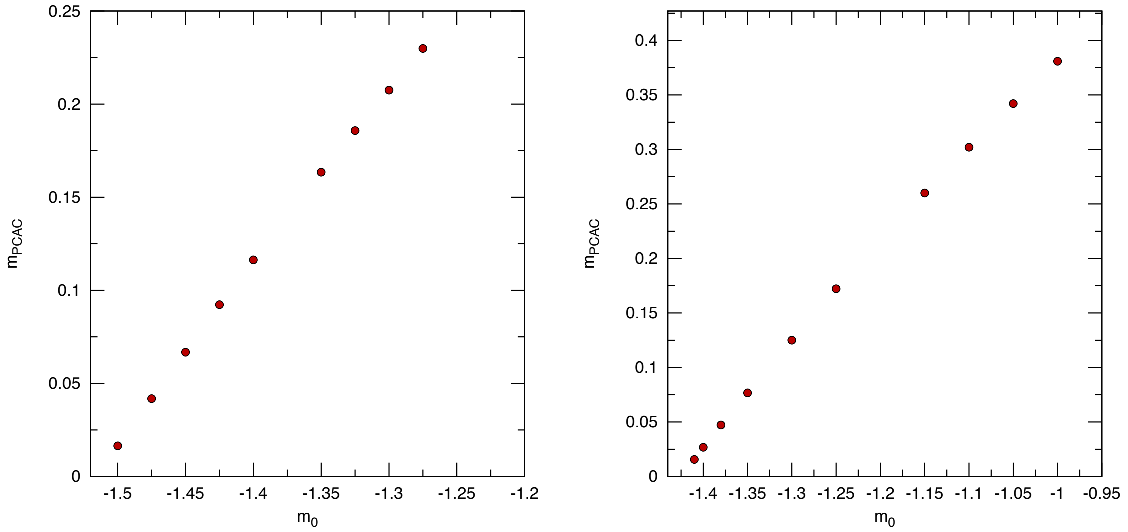

(a) $16^3 \times 32$ lattice with $\beta = 5.75$

(b) 16^4 lattice with $\beta = 6$

Figure 24: The quark mass determined from the axial ward identity m_{PCAC} vs. the bare quark mass m_0. Note that the errors are smaller than point markers so they do not show in the plot.

For the convenience of the reader figure 24 shows the PCAC quark mass as a function of the bare mass parameter m_0.

When looking at the spectrum the first thing one can look at for a sign of chiral symmetry breaking is if there is a tendency in figure 25 towards a mass splitting between the pseudoscalar and the vector meson as the quark mass is decreased. It maybe seems there is, but this is more evident when looking at figure 26 where the ratio is plotted. As also discussed in chapter 5 , if chiral symmetry breaks we expect the $m_{\text{V}}/m_{\text{PS}}$ to diverge at zero quark mass since the pseudoscalar mesons, i.e. the 'pions', are Goldstone bosons of the model, whereas the vector meson should retain a mass. This indicates that chiral symmetry breaking is taking place in this model and this confirms the results of Fodor *et al.* [68, 73, 69].

Figure 27 shows the pseudoscalar meson decay constant f_{PS} as a function of the quark mass m_{PCAC} in lattice units. It is seen to decrease more rapidly towards the lower quark masses and the analytical expectation of the approach towards the chiral limit is required to reliably extract f_{PS}. Of course this quantity in particular is important when making predictions for the LHC since, as discussed earlier, it will be used to fix the scale of the theory in a technicolor scenario. Upon fixing the physical scale with f_{PS} in the chiral limit the ratio $m_{\text{V}}/f_{\text{PS}}$ becomes interesting since this will tell us the physical scale of the vector meson. This ratio is plotted in figure 26. It is not easy from this plot, to determine accurately what this ratio is in the chiral limit. It seems that for

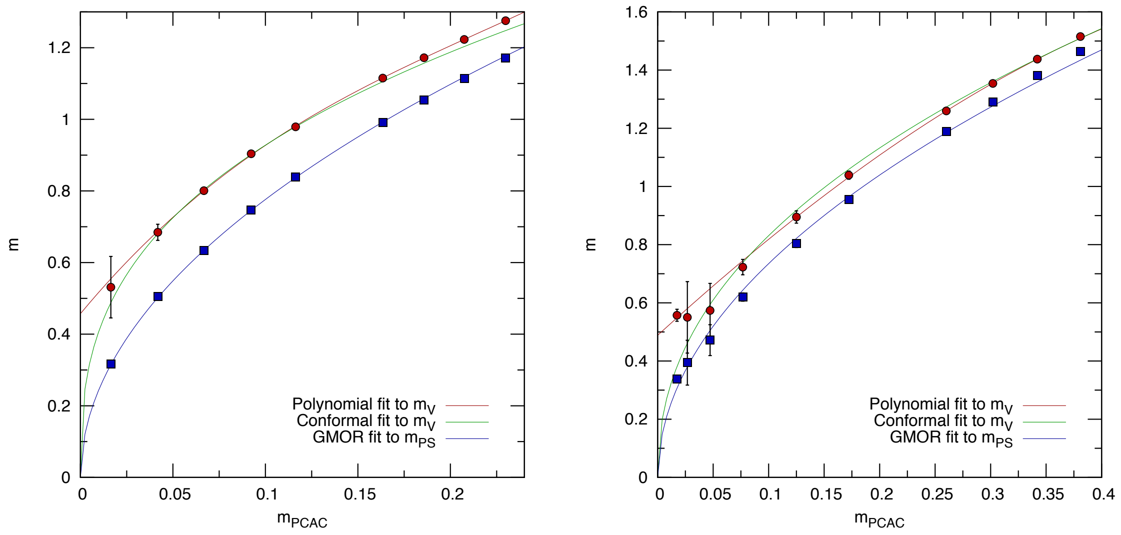

(a) $16^3 \times 32$ lattice with $\beta = 5.75$

(b) 16^4 lattice with $\beta = 6$

Figure 25: Pseudoscalar and vector meson masses vs. the quark mass. Some fits to the data has been included as well

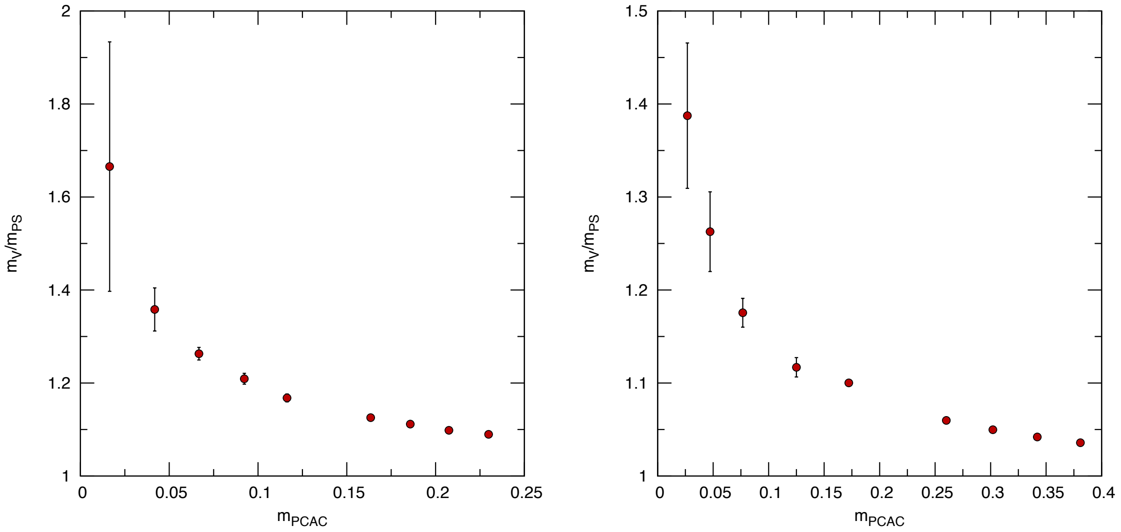

(a) $16^3 \times 32$ lattice with $\beta = 5.75$

(b) 16^4 lattice with $\beta = 6$

Figure 26: Ratio between messes of the vector meson and the pseudocalar meson.

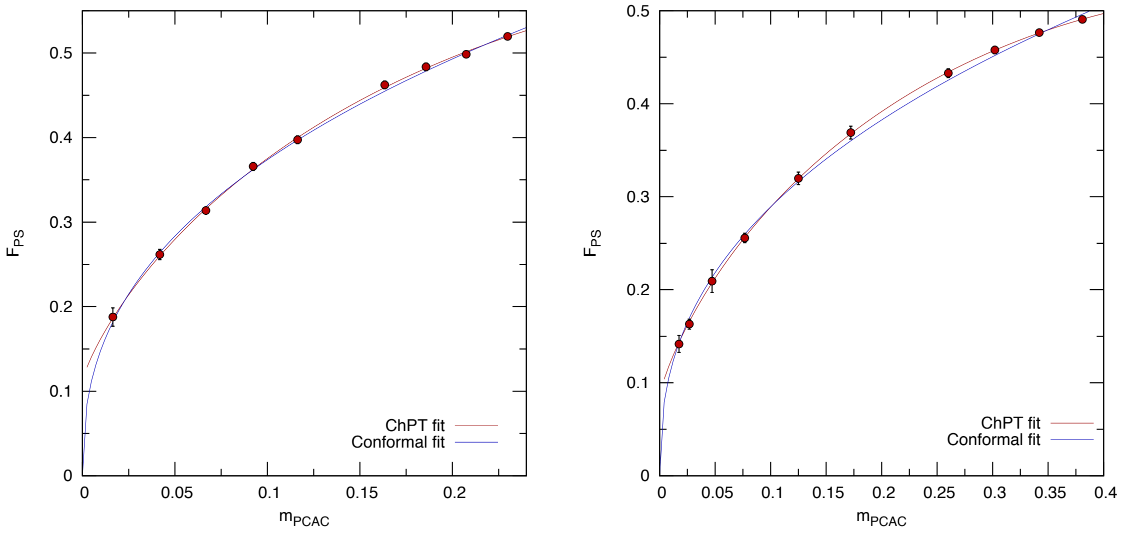

(a) $16^3 \times 32$ lattice with $\beta = 5.75$

(b) 16^4 lattice with $\beta = 6$

Figure 27: The decay constant for pseudoscalar meson as a function of the quark mass.

small quark masses this ratio rises. In particular the $\beta = 6$ data in figure 28b increases rapidly as the quark mass is decreased. With the present data it is hard to determine the precise reason for this rise, but a couple of things come to mind. Finite size effects might decrease the value of f_{PS} when the pions are sufficiently light. This could possibly result in a rise in the $m_{\text{V}}/f_{\text{PS}}$ ratio.

Another possibility is that chiral logarithms are relevant at these quark masses. If this is the case the pseudoscalar decay constant should obey the formula (3.16) presented in chapter 3. As we will see shortly, this is indeed the case. Before moving on to the chiral fits it is worth having a look at figure 29 showing the ratio $m_{\text{PS}}^2/m_{\text{PCAC}}$ as the chiral limit is approached. In the $\beta = 6$ data shown in figure 28b this ratio also rises rapidly as the quarks become lighter. Again, it can be hard to pinpoint the explanation for this, but the same considerations apply. It is worth mentioning that in Wilson Chiral Perturbation Theory logarithmic terms $\sim \log m_{\text{quark}}$ divergent in the $m_{\text{quark}} \to 0$ limit appear at second order in the lattice spacing[41]. This is in contrast to the usual $m_{\text{quark}} \log m_{\text{quark}}$ terms appearing without including the lattice artifacts.

When doing chiral extrapolations we are sensitive in particular to the measurements at small quark masses, but the spectral observables have large uncertainties in this regime. This is due to large correlation times. Figure 30a illustrates this by binning configurations and plotting the expectation value of f_{PS} in each bin as a function of the number of completed Hybrid Monte Carlo updates with unit trajectory length. Figure 30b shows a similar plot for m_{PS}.

In order for the statistical errors not to be underestimated we have used binsizes up to 200

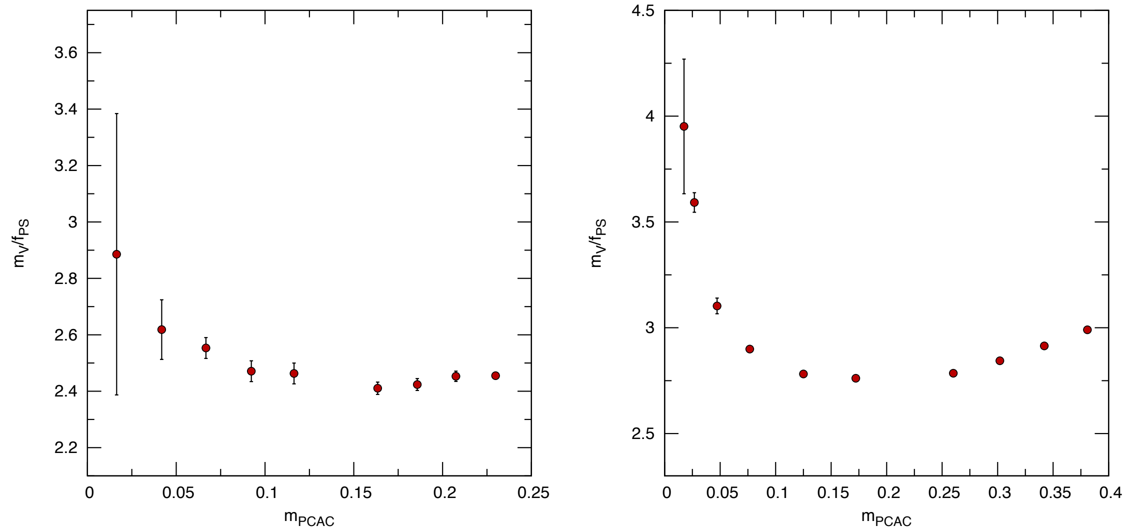

(a) $16^3 \times 32$ lattice with $\beta = 5.75$

(b) 16^4 lattice with $\beta = 6$

Figure 28: Vector meson mass divided by the pion decay constant.

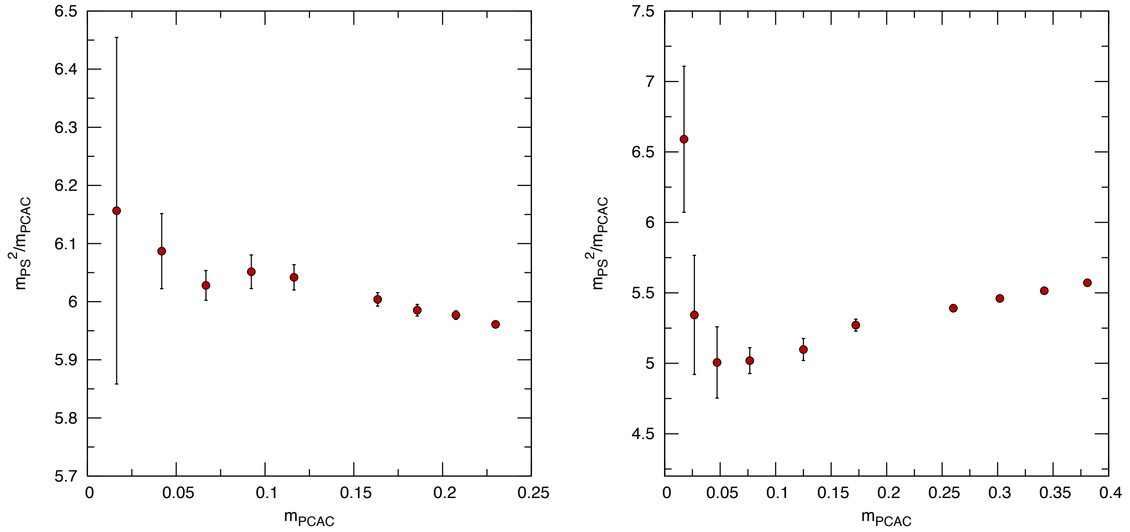

(a) $16^3 \times 32$ lattice with $\beta = 5.75$

(b) 16^4 lattice with $\beta = 6$

Figure 29: Pseudoscalar mass squared over the quark mass vs the quark mass.

when computing expectation values for the spectrum.

We would have liked to include measurements of the mass of the axial vector meson. However, we have been unsuccesful in extracting reliable estimates in this channel. Hopefully, with more data, we will be able to successfully revisit this analysis.

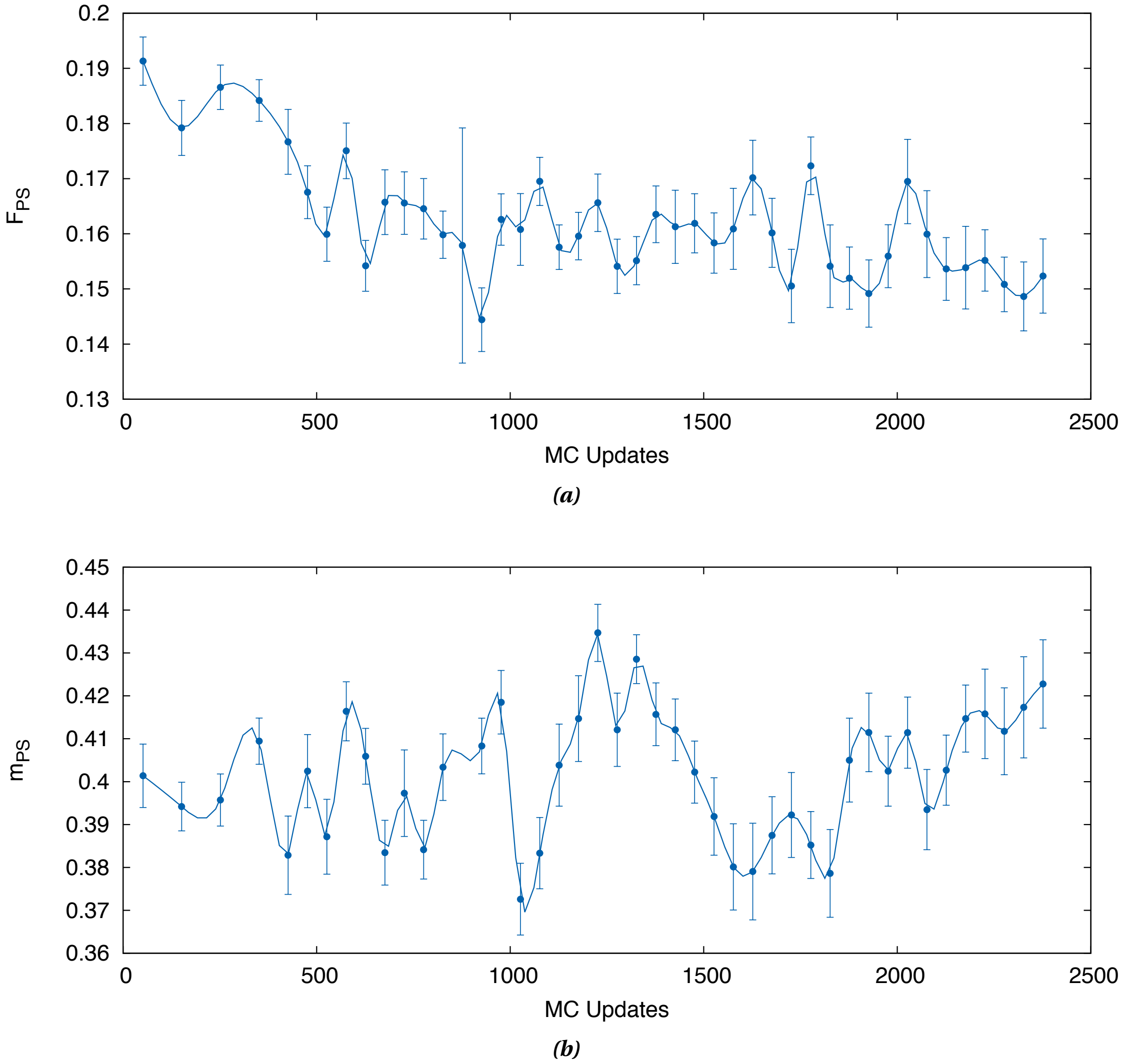

Figure 30: Pseudoscalar decay constant and mass measured in bins of 50 configurations and plottet as a function of Monte Carlo updates. The measurements were done on a 16^4 lattice at $\beta = 6$ and $m_0 = -1.4$ corresponding to $m_{\text{PCAC}} = 0.027$. The solid lines are guides for the eye.

Finite size effects

In the work by Fodor *et al.*[69] it is reported that the infinite volume limit is reached within 1% if $m_{\text{PS}} L \geq 5$. At the lightest quark mass used in the simulations at $\beta = 6$ on the 16^4 lattice we have $m_{\text{PS}} L \simeq 4.2$, but at the next-to lowest mass point the quantity is $m_{\text{PS}} L \simeq 5.5$. In the $\beta = 5.75$

simulations on the $16^3 \times 32$ lattice we find at the lightest quark mass that $m_{\mathrm{PS}}L \simeq 5.1$.

Since data from bigger lattices are not available at the lowest quark masses we can not make a fit to the asymptotic formula (3.11). This could otherwise have been used to make an infinite volume extrapolation. Simulations on bigger lattices are underway, but until then we will try to quantify our sensitivity to the lightest quark mass data by performing chiral fits both with and without these points.

An estimate of the magnitude of the finite size correction can be made from the observations of Fodor *et al.*[69]. They observe approximately 15 % decrease from the value of m_{PS} at $m_{\mathrm{PS}}L \simeq 3.2$ to the infinite volume extrapolation. From m_{PS} at $m_{\mathrm{PS}}L \simeq 4.3$ the decrease is about 3 %. For the decay constant of the pseudoscalar the relative increase is roughly similar.

According to these results we should be unable to detect any finite size effects at the next-to-lowest mass point on the $\beta = 6$, 16^4 lattice, where $m_{\mathrm{PS}}L \simeq 5.5$. For this particular set of parameters there are simulation data available on three volumes: $16^3 \times 32$, $20^3 \times 32$ and $24^3 \times 32$. A plot showing the dependence of f_{PS}, m_{PS} and m_{PCAC} on L can be found in figure 31. The data does not reveal any finite size effects significant beyond the statistical errors.

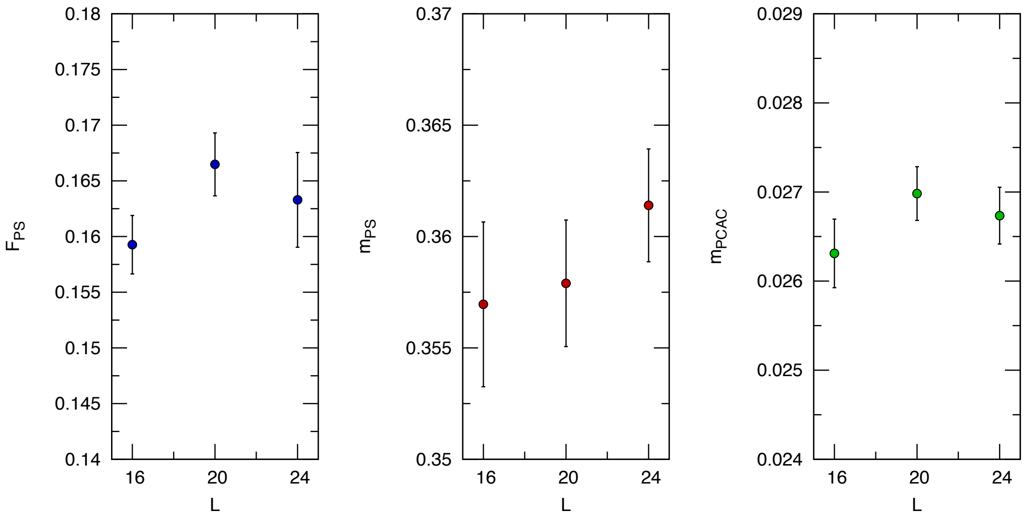

(a) *(b)* *(c)*

Figure 31: Finite size effects. Configurations are measured at $\beta = 6$, $m_0 = -1.4$ on lattices of size $L^3 \times 32$. At $L = 16$ we have $m_{\mathrm{PS}}L \simeq 5.5$

Chiral limit

In order to extract the chirally extrapolated quantities we use different kinds of fits. Our choices are based on the assumption of chiral symmetry breaking on one side and a mass deformed conformal scenario on the other. The corresponding fits are those of chiral perturbation theory (3.15), (3.16) on one side and hyperscaling relations (3.17) on the other. For the pion decay constant we test for two different kind of fits:

$$\text{Wilson ChPT fit:} \quad f_{\mathrm{PS}}(m) = F_0 + Am + Bm\log(m)\,, \tag{6.34}$$

$$\text{Conformal fit:} \quad f_{\mathrm{PS}}(m) = Cm^{\frac{1}{1+\gamma}}\,. \tag{6.35}$$

m is the PCAC quark mass. For the mass of the vector meson we deploy the following fits

$$\text{Three term fit:} \quad m_{\mathrm{V}}(m) = M_0 + c_2 m_{\mathrm{PS}}^2 + c_3 m_{\mathrm{PS}}^3\,, \tag{6.36}$$

$$\text{Polynomial fit:} \quad m_{\mathrm{V}}(m) = M_0 + c_1 m + c_2 m^2 + c_3 m^3\,, \tag{6.37}$$

$$\text{Conformal fit:} \quad m_{\mathrm{V}}(m) = Cm^{\frac{1}{1+\gamma}}\,. \tag{6.38}$$

The "Three term fit" is again motivated by Chiral Perturbation Theory, whereas the polynomial fit is included to give a good versatile fit able to provide a chiral extrapolation without prejudice. For the pseudoscalar we include the following fit types

$$\text{GMOR fit:} \quad m_{\mathrm{PS}}(m) = A\sqrt{m}\,, \tag{6.39}$$

$$\text{Conformal fit:} \quad m_{\mathrm{PS}}(m) = Cm^{\frac{1}{1+\gamma}}\,. \tag{6.40}$$

In our conformal fits we have allowed the anomalous dimension to vary independently. It is seen in tables 7, 8 and 9 that these scaling fits, termed "Conformal fits", gives quite good results with the exception of the m_{V} fit at $\beta = 6$. This fit improves significantly if the lightest mass point is disregarded. As we have just discussed, this might be justified by finite size considerations. Even though these fits are good their preferred value for the anomalous dimension varies from channel to channel. This is in conflict with the hyperscaling hypothesis. Consider for instance the fits to f_{PS} in table 7. They favor a value around $\gamma \simeq 1.5$ whereas the best fit values for the pseudoscalar meson mass is $\gamma \simeq 1.0$ and $\gamma \simeq 0.85$ for $\beta = 5.75$ and $\beta = 6$ respectively.

Note that the conformal fits to f_{PS} and m_V are shown in figure 27 and 25 respectively.

Next we consider the fits relating to a scenario where chiral symmetry is spontaneously broken. Also these fits are shown in the figures 27 and 25. Stating with the f_{PS} data we can see in table 7 that the "Wilson ChPT" fits are somewhat better than the conformal fits, but clearly both fit types are compatible with data having χ^2/d.o.f of order one or less. This is of course only because γ is not fitted globally but is left unconstrained in the fits. The significance of the fits being "Wilson ChPT" fits and not just "ChPT" fits is that the coefficients in (6.34) are totally unconstrained. In ordinary chiral perturbation theory, the B coefficient should be related to F_0

Fit	β	Values	d.o.f	χ^2/d.o.f
f_{PS} Wilson ChPT fit	5.75	$F_0 = 0.113(7)$	6	0.437
f_{PS} Conformal fit		$\gamma = 1.51(4)$	7	1.05
f_{PS} Wilson ChPT fit	6.00	$F_0 = 0.083(1)$	7	0.0323
f_{PS} Conformal fit		$\gamma = 1.47(6)$	8	1.70
Excluding the lightest point				
f_{PS} Wilson ChPT fit	6.00	$F_0 = 0.083(2)$	6	0.0373
f_{PS} Conformal fit		$\gamma = 1.48(7)$	7	1.94

Table 7: Summary of fits to the pseudoscalar decay constant.

Fit	β	Values	d.o.f	χ^2/d.o.f
m_{V} Three term fit	5.75	$M_0 = 0.406(7)$	2	0.00768
m_{V} Polynomial fit		$M_0 = 0.46(1)$	5	0.0936
m_{V} Conformal fit		$\gamma = 1.81(6)$	3	0.14987
m_{V} Three term fit	6.00	$M_0 = 0.46(1)$	4	0.221
m_{V} Polynomial fit		$M_0 = 0.49(2)$	5	0.380
m_{V} Conformal fit		$\gamma = 1.2(1)$	8	11.2
Excluding the lightest point				
m_{V} Conformal fit	$\beta = 6.00$	$\gamma = 1.09(2)$	7	0.289

Table 8: Summary of fits to the vector meson spectrum. In the fits a number of heavy mass points were discarded in the fit. This number was determined by the one minimizing χ^2/d.o.f while including an acceptable number of points in the fit.

Fit	β	Values	d.o.f	χ^2/d.o.f
m_{PS} GMOR fit	5.75		4	0.107
m_{PS} Conformal fit		$\gamma = 1.002(7)$	7	0.139
m_{PS} GMOR fit	6.00		6	2.25
m_{PS} Conformal fit		$\gamma = 0.854(6)$	7	0.0908

Table 9: Summary of fits to the pseudoscalar meson spectrum. In the fits a number of heavy mass points were discarded in the fit. This number was determined by the one minimizing χ^2/d.o.f while including an acceptable number of points in the fit.

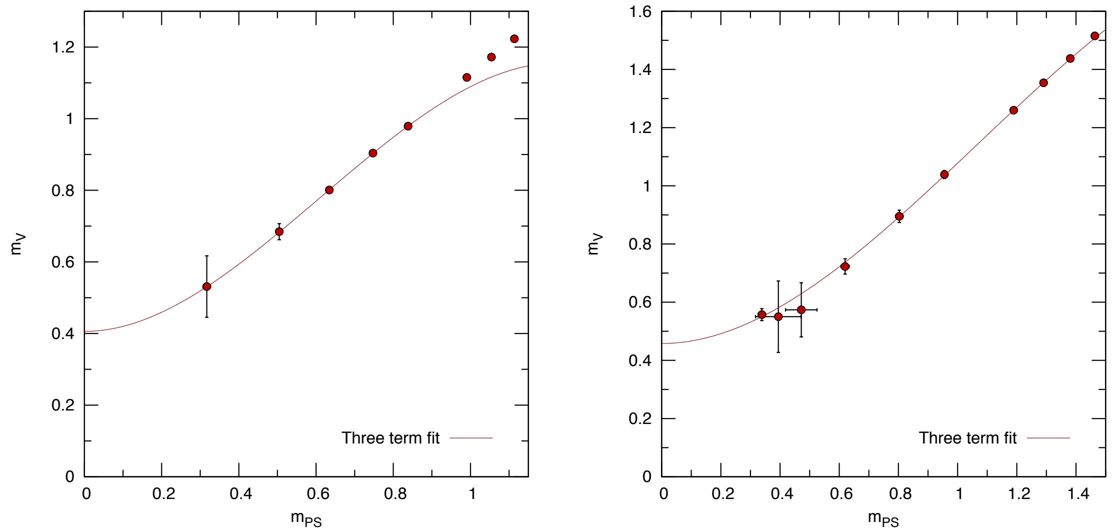

(a) $16^3 \times 32$ lattice with $\beta = 5.75$

(b) 16^4 lattice with $\beta = 6$

Figure 32: Vector meson mass vs the pseudoscalar mass.

and the A coefficient in the GMOR fit (6.39). This correspondence was discussed in chapter 3 and can be seen from equation (3.15) and (3.16). The fits allow us to read off the decay constant in the chiral limit in lattice units. Conversely we can use this to determine our lattice spacing in physical units if we fix the scale to $f_{\text{PS}} = 246$ GeV. For example we can write with all factors of lattice spacing, Planck constant and speed of light

$$\frac{f_{\text{PS}} a_{\beta=5.75}}{hc} = 0.113 \quad \Leftrightarrow \quad a_{\beta=5.75} \simeq 5.68 \cdot 10^{-19}\,\text{m}. \tag{6.41}$$

A similar calculation for $\beta = 6$ gives

$$a_{\beta=6.00} \simeq 4.18 \cdot 10^{-19}\,\text{m}. \tag{6.42}$$

Moving on the the vector meson fits in table 8 we see that the quality of the three-term fits and the polynomial fits are excellent. The polymanial fit is displayed in figure 25 while the three-term-fits are depicted in figure 32. Which of these two functional forms is best suited for the chiral extrapolation is difficult to say. Due to the fact that the three term fit has a theoretical motivation behind it, this is a reasonable choice. However, if we look in figure 32 it appears that the flattening of the fit curve towards small quark masses is supported by very few datapoints. For this reason we will retain both chiral extrapolation procedures in our analysis.

The fits give us chirally extrapolated values of the vector meson masses in lattice units. Since we have already determined our lattice spacings in physical units we can immediately state the results in physical units:

Three term extrapolation: $m_{\mathrm{v}}^{\beta=5.75} \simeq 0.89\ \mathrm{TeV}$,
Polynomial extrapolation: $m_{\mathrm{v}}^{\beta=5.75} \simeq 1.0\ \mathrm{TeV}$,
Three term extrapolation: $m_{\mathrm{v}}^{\beta=6.00} \simeq 1.4\ \mathrm{TeV}$,
Polynomial extrapolation: $m_{\mathrm{v}}^{\beta=6.00} \simeq 1.4\ \mathrm{TeV}$.

At this point we have not stated any errors in these values. In order to estimate the errors we use the following proceedure. We force the M_0 paramter in the three term fit (6.36) and polynomial fit (6.37) to a range of values in the vicinity of the best fits stated in table 8. At each of these values we compute the corresponding χ^2. We can for each χ^2 compute the probability Q of the outcome of our measurements given the forced value of M_0 and the functional form of the fit is correct

$$Q = \left(2^{d/2}\Gamma\left(d/2\right)\right)^{-1} \int_{\chi^2}^{\infty} ds s^{d/2-1} e^{-t/2}. \tag{6.43}$$

d is the number of degrees of freedom. The errors are then found by computing the values of M_0 corresponding to $Q = 0.159$ (one sigma). The accepted interval around the best fit value need not be symmetric. However, we find that they very nearly are, so we will state only one error for each estimate of m_V.

Three term extrapolation: $\sigma_{m_{\mathrm{v}}^{\beta=5.75}} \simeq 0.33\ \mathrm{TeV}$,
Polynomial extrapolation: $\sigma_{m_{\mathrm{v}}^{\beta=5.75}} \simeq 0.24\ \mathrm{TeV}$,
Three term extrapolation: $\sigma_{m_{\mathrm{v}}^{\beta=6.00}} \simeq 0.19\ \mathrm{TeV}$,
Polynomial extrapolation: $\sigma_{m_{\mathrm{v}}^{\beta=6.00}} \simeq 0.19\ \mathrm{TeV}$.

Now we are ready to perform our continuum extrapolation and extract our best estimate for the physical mass of the vector meson.

Continuum extrapolation

We should in principle also estimate the errors for our lattice spacings in order to fully estimate the uncertainty of the final extrapolation. However, we will not do this at this point since the continuum extrapolation is anyway very uncertain due to the fact that we only have data at two lattice spacing which are not very for from each other.

In figure 33 we have plotted the chiral values of m_{v} in physical units against the lattice spacing. The plot also shows the linear continuum extrapolations. To the left in the plot the

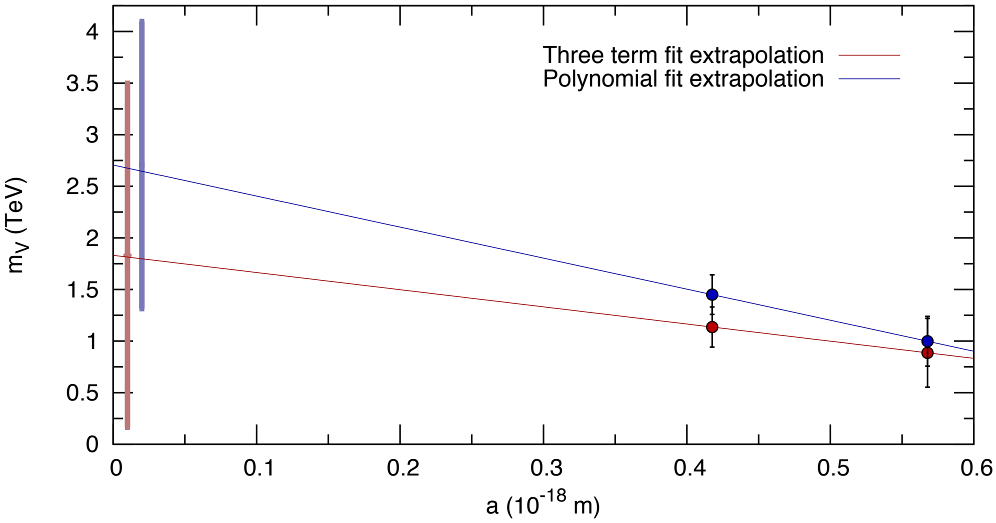

Figure 33: The above plot shows the linear continuum extrapolation of the m_{V} data obtained by two different chiral extrapolation schemes. The red points are the m_{PS} values obtained from the three term fit and the blue points are from the polynomial fits. The colored bars to the left denote the range of continuum values compatible with data within one sigma.

range of continuum values compatible with data within one sigma is marked. This range is again determined by the method used to estimate the errors in the chiral extrapolations.

We will end the presentation of our numerical investigation of the SU(3) sextet MWT model by stating our preliminary results for the physical mass of the vector meson. For this final estimate we will use the data obtained by the polynomial chiral extrapolations. This choice is motivated by the lack of data at small m_{PC}. This causes the three term fits shown in figure 32 to look somewhat unreliable. Therefore

$$m_{\mathrm{V}} = 2.71\ ^{+1.39}_{-1.39}\ \mathrm{TeV}\ .$$

The value is in agreement with what is found by Fodor et al.[69]. It will be very interesting to get a more accurate determination of this mass allowing a possibility of testing this model at the LHC.

Summary and outlook

7

In this thesis we have outlined some of the methods used in the non-perturbative, lattice regularized studies of technicolor models relevant for physics beyond the Standard Model. After a brief discussion of the transition from a lattice gauge theory to real world phenomenology, we presented a GPU accelerated algorithm for lattice simulations. The particular implementation presented in this thesis builds upon the HiRep code[43], which is a versatile suite for lattice simulations with Wilson fermions in arbitrary representations of SU(N). The GPU code uses a mixed precision γ_5-QMR algorithm to perform the computationally intensive inversion of the Dirac operator. The mixed precision solver will perform the inversion in single precision and accumulate the result in double precision. This should take advantage of the fast single precision operations on the GPU. A rearrangement of the memory layout was done. This allows for coalesced memory access and enhances the performance drastically. Futhermore, packing and on-the-fly representation of the gauge field was introduced in order to reduce the amount of data transfer between global and local memory. This gave up to 40 % performance enhancement in the Dirac operation.

Besides the more technical aspects relating to algorithms and performance of simulation software, some new results in models of physics beyond the Standard Model was presented. Two explicit models have been considered, and their spectrum investigated on the lattice. The two models are the SO(4) Minimal Walking Technicolor model and the SU(3) sextet Minimal Walking Technicolor model. The two models have in common that they have only one doublet of fermions. Besides that, the phenomenology of the models are quite different due to their different patterns of global symmetry breaking. If chiral symmetry breaks, the SO(4) model has an SU(4)→SO(4) flavor symmetry breaking pattern. This gives 6 additional Goldstone modes compared to the SU(2)×SU(2)→SU(2) breaking pattern seen in models with fermions in a complex representation. When charged under the electroweak interactions, these additional

Goldstone bosons form a complex, baryonic isospin triplet with interesting phenomenological consequences[59].

Simulations of the SO(4) model at fixed lattice spacing was performed. Evidence is presented in this thesis that favor a chiral symmetry breaking scenario over an infrared conformal one. More studies are underway and more data will allow a more systematic study, where finite volume effects can be taken into account. This should make possible a more definite conclusion about the infrared behavior of the model and possible give more accurate estimates of the spectrum. This might be relevant for the Large Hadron Collider since we show that the vector meson in this model can be as light as ~ 1.2 TeV.

We also present numerical results for the SU(3) Sextet Minimal Walking Technicolor model. Most simulations were performed using the GPU accelerated version of the HiRep code. Simulations were carried out at two different lattice spacings. We present evidence in favor of chiral symmetry breaking in agreement with recent work[73, 69]. Other studies[71], using Schrödinger functional techniques on smaller lattices, suggest that an infrared fixed point exists, but are unable to rule out a slowly running coupling. While the simulations carried out in [73, 69] was done using staggered fermions with rooting of the fermion determinant, we use Wilson fermions. We perform a continuum extrapolation of our vector meson masses and find it to be $m_{\mathrm{V}} = 2.71\ {}^{+1.39}_{-1.39}\ \mathrm{TeV}$.

It would of course be very interesting if we would be able to extract a mass for the Higgs like 0^{++} state in both the SO(4) MWT and the SU(3) sextet MWT model. It presents a huge technical and numerical task. The correlators involved in the calculations are both gluonic and fermionic since the 0^{++} glueball will mix with the flavor singlet meson with the same quantum numbers. Furthermore the fermionic part will have contributions from disconnected quark loops meaning that "all-to-all" lattice correlators are required in the evaluation. The authors of [69] have already commenced in this challenging task in the SU(3) sextet model. A reliable estimate of the 0^{++} state can potentially allow the model to be excluded by present LHC data.

Another direction for future studies are the calculation of the electric and magnetic form factors. This will be relevant especially for the SO(4) MWT model, since it contains a dark matter candidate.

Last but not least it would very interesting to estimate non-perturbatively the size of the contribution to the S parameter coming from these models. This could potentially provide another means of excluding them.

A

Construction of hadrons in SO(4)

An example of a gauge and Lorentz invariant object could be

$$\delta_{ab} u^a_\alpha \varepsilon^{\alpha\beta} u^b_\beta . \tag{A.1}$$

Suppressing now the Technicolor indices and writing this in terms of Dirac spinors the projection operators can conveniently be introduced

$$P_L = \frac{\mathbf{1}-\gamma_5}{2}, \quad P_R = \frac{\mathbf{1}+\gamma_5}{2}, \tag{A.2}$$

giving us

$$\delta_{ab} u^a_\alpha \varepsilon^{\alpha\beta} u^b_\beta \quad \leftrightarrow \quad (P_L u_{\text{D}})^T \begin{pmatrix} \varepsilon^{\alpha\beta} & \mathbf{0} \\ \mathbf{0} & \mathbf{X} \end{pmatrix} (P_L u_{\text{D}})$$

The $\mathbf{X}$ is at this point arbitrary since it only affects the right handed part of the Dirac fermions which is projected away. One particular choice, which will prove convenient, is $\mathbf{X} = \varepsilon_{\dot\alpha\dot\beta}$. In this case the matrix will be the charge conjugation matrix:

$$C = \begin{pmatrix} \varepsilon^{\alpha\beta} & \mathbf{0} \\ \mathbf{0} & \varepsilon_{\dot\alpha\dot\beta} \end{pmatrix} = i\gamma^0\gamma^2 . \tag{A.3}$$

Note that $\{\gamma^5, \gamma^\mu\} = 0$ so $[\gamma^5, C] = 0$ and $[P_L, C] = 0$. Note also that $P_L^T = P_L$ since $(\gamma^5)^T = \gamma^5$ and $P_L^2 = P_L$. The operator in question can now be expressed as

$$\Pi^L_{uu} \equiv u_{\text{D}}^T P_L C u_{\text{D}} . \tag{A.4}$$

The analogous operator for the opposite projection is

$$\Pi^R_{uu} \equiv u_{\text{D}}^T P_R C u_{\text{D}} \quad \leftrightarrow \quad \delta_{ab} \bar{\tilde{u}}^{a\dot\alpha} \varepsilon_{\dot\alpha\dot\beta} \bar{\tilde{u}}^{b\dot\beta} . \tag{A.5}$$

The operators Π^L_{uu} and Π^R_{uu} does not have definite parity so it is custom to consider instead the two linear combinations

$$\Pi_{uu} \equiv \Pi^R_{uu} + \Pi^L_{uu} = u_{\mathrm{D}}^T C u_{\mathrm{D}}\,, \tag{A.6}$$

$$\tilde{\Pi}_{uu} \equiv \Pi^R_{uu} - \Pi^L_{uu} = u_{\mathrm{D}}^T \gamma^5 C u_{\mathrm{D}}\,. \tag{A.7}$$

Note that $P(\tilde{\Pi}_{uu}) = +1 = -P(\tilde{\Pi}_{\bar{u}u})$ and $P(\Pi_{uu}) = -1 = -P(\Pi_{\bar{u}u})$. The remaining scalar and pseudoscalar baryons can be constructed in a similar way.

The mesonic operators can be constructed from similar considerations. However we will now use u_α and $\tilde{u}_\beta$ as a starting point.

$$\tilde{u}_\alpha \varepsilon^{\alpha\beta} u_\beta = \tilde{u}^\alpha u_\alpha \quad \leftrightarrow \quad (P_R u_{\mathrm{D}})^\dagger \gamma^0 (P_L u_{\mathrm{D}}) = \bar{u}_{\mathrm{D}} P_L u_{\mathrm{D}}\,, \tag{A.8}$$

where we have suppressed the color indices. Similarly

$$\bar{u}_{\mathrm{D}} P_R u_{\mathrm{D}}\,, \tag{A.9}$$

is a valid combination and as with the diquark states we choose the linear combinations with definite parity

$$\Pi_{\bar{u}u} \equiv \bar{u}_{\mathrm{D}} P_L u_{\mathrm{D}} + \bar{u}_{\mathrm{D}} P_R u_{\mathrm{D}} = \bar{u}_{\mathrm{D}} u_{\mathrm{D}}\,, \tag{A.10}$$

$$\tilde{\Pi}_{\bar{u}u} \equiv \bar{u}_{\mathrm{D}} P_L u_{\mathrm{D}} - \bar{u}_{\mathrm{D}} P_R u_{\mathrm{D}} = \bar{u}_{\mathrm{D}} \gamma^5 u_{\mathrm{D}}\,. \tag{A.11}$$

Vector mesons and baryons

The vector mesons and baryons can be constructed through the same considerations as for the scalar operators. However one includes a Dirac γ-matrix in the building blocks:

$$q_{\mathrm{D}}^T C = \left(q^\alpha\,, \bar{\tilde{q}}_{\dot{\alpha}}\right) \quad \text{and} \quad \gamma^\mu q_{\mathrm{D}} = \begin{pmatrix} \sigma^\mu_{\ \alpha\dot{\beta}} \bar{\tilde{q}}^{\dot{\beta}} \\ (\bar{\sigma}^\mu)^{\dot{\alpha}\beta} q_\beta \end{pmatrix}\,, \tag{A.12}$$

for the baryons and

$$\bar{q}_{\mathrm{D}} \quad \text{and} \quad \gamma^\mu q_{\mathrm{D}}\,, \tag{A.13}$$

for the mesons. This gives the following baryons:

$$V^\mu_{uu} \equiv u_{\mathrm{D}}^T C \gamma^\mu u_{\mathrm{D}}\,, \qquad \tilde{V}^\mu_{uu} \equiv u_{\mathrm{D}}^T \gamma^5 C \gamma^\mu u_{\mathrm{D}}\,, \tag{A.14}$$

$$V^\mu_{dd} \equiv d_{\mathrm{D}}^T C \gamma^\mu d_{\mathrm{D}}\,, \qquad \tilde{V}^\mu_{dd} \equiv d_{\mathrm{D}}^T \gamma^5 C \gamma^\mu d_{\mathrm{D}}, \tag{A.15}$$

$$V^\mu_{ud} \equiv u_{\mathrm{D}}^T C \gamma^\mu d_{\mathrm{D}}\,, \qquad \tilde{V}^\mu_{ud} \equiv u_{\mathrm{D}}^T \gamma^5 C \gamma^\mu d_{\mathrm{D}}\,, \tag{A.16}$$

$$V^\mu_{du} \equiv d_{\mathrm{D}}^T C \gamma^\mu u_{\mathrm{D}}\,, \qquad \tilde{V}^\mu_{du} \equiv d_{\mathrm{D}}^T \gamma^5 C \gamma^\mu u_{\mathrm{D}}\,, \tag{A.17}$$

and the following mesons:

$$V^{\mu}_{\bar{u}u} \equiv \bar{u}_{\mathrm{D}}\gamma^{\mu}u_{\mathrm{D}}\,, \qquad \tilde{V}^{\mu}_{\bar{u}u} \equiv \bar{u}_{\mathrm{D}}\gamma^{\mu}\gamma^{5}u_{\mathrm{D}}\,, \tag{A.18}$$

$$V^{\mu}_{\bar{d}d} \equiv \bar{d}_{\mathrm{D}}\gamma^{\mu}d_{\mathrm{D}}\,, \qquad \tilde{V}^{\mu}_{\bar{d}d} \equiv \bar{d}_{\mathrm{D}}\gamma^{\mu}\gamma^{5}d_{\mathrm{D}}\,, \tag{A.19}$$

$$V^{\mu}_{\bar{u}d} \equiv \bar{u}_{\mathrm{D}}\gamma^{\mu}d_{\mathrm{D}}\,, \qquad \tilde{V}^{\mu}_{\bar{u}d} \equiv \bar{u}_{\mathrm{D}}\gamma^{\mu}\gamma^{5}d_{\mathrm{D}}\,, \tag{A.20}$$

$$V^{\mu}_{\bar{d}u} \equiv \bar{d}_{\mathrm{D}}\gamma^{\mu}u_{\mathrm{D}}\,, \qquad \tilde{V}^{\mu}_{\bar{d}u} \equiv \bar{d}_{\mathrm{D}}\gamma^{\mu}\gamma^{5}u_{\mathrm{D}}\,. \tag{A.21}$$

Bibliography

[1] P. Frampton, “Vacuum Instability and Higgs Scalar Mass,” *Phys.Rev.Lett.*, vol. 37, p. 1378, 1976.

[2] J. Ellis, J. Espinosa, G. Giudice, A. Hoecker, and A. Riotto, “The Probable Fate of the Standard Model,” *Phys.Lett.*, vol. B679, pp. 369–375, 2009.

[3] O. Antipin, M. Gillioz, J. Krog, E. Mølgaard, and F. Sannino, “Standard Model Vacuum Stability and Weyl Consistency Conditions,” 2013.

[4] J. Goldstone, “Field Theories with Superconductor Solutions,” *Nuovo Cim.*, vol. 19, pp. 154–164, 1961.

[5] Y. Nambu, “Quasiparticles and Gauge Invariance in the Theory of Superconductivity,” *Phys.Rev.*, vol. 117, pp. 648–663, 1960.

[6] S. Weinberg, “Implications of Dynamical Symmetry Breaking,” *Phys.Rev.*, vol. D13, pp. 974–996, 1976.

[7] L. Susskind, “Dynamics of Spontaneous Symmetry Breaking in the Weinberg-Salam Theory,” *Phys.Rev.*, vol. D20, pp. 2619–2625, 1979.

[8] S. Eidelman *et al.*, “Review of particle physics. Particle Data Group,” *Phys.Lett.*, vol. B592, p. 1, 2004.

[9] T. W. Appelquist, D. Karabali, and L. Wijewardhana, “Chiral Hierarchies and the Flavor Changing Neutral Current Problem in Technicolor,” *Phys.Rev.Lett.*, vol. 57, p. 957, 1986.

[10] K. Yamawaki, M. Bando, and K.-i. Matumoto, “Scale Invariant Technicolor Model and a Technidilaton,” *Phys.Rev.Lett.*, vol. 56, p. 1335, 1986.

[11] H. S. Fukano and F. Sannino, "Conformal Window of Gauge Theories with Four-Fermion Interactions and Ideal Walking," *Phys.Rev.*, vol. D82, p. 035021, 2010.

[12] M. E. Peskin and T. Takeuchi, "Estimation of oblique electroweak corrections," *Phys. Rev. D*, vol. 46, pp. 381–409, Jul 1992.

[13] D. C. Kennedy and P. Langacker, "Precision electroweak experiments and heavy physics: A global analysis," *Phys. Rev. Lett.*, vol. 65, pp. 2967–2970, Dec 1990.

[14] M. E. Peskin and T. Takeuchi, "New constraint on a strongly interacting higgs sector," *Phys. Rev. Lett.*, vol. 65, pp. 964–967, Aug 1990.

[15] G. Altarelli and R. Barbieri, "Vacuum polarization effects of new physics on electroweak processes," *Physics Letters B*, vol. 253, no. 1,??2, pp. 161 – 167, 1991.

[16] M. Baak, M. Goebel, J. Haller, A. Hoecker, D. Kennedy, *et al.*, "The Electroweak Fit of the Standard Model after the Discovery of a New Boson at the LHC," *Eur.Phys.J.*, vol. C72, p. 2205, 2012.

[17] R. Foadi and F. Sannino, "S and T Parameters from a Light Nonstandard Higgs versus Near Conformal Dynamics," 2012.

[18] H.-J. He, N. Polonsky, and S.-f. Su, "Extra families, Higgs spectrum and oblique corrections," *Phys.Rev.*, vol. D64, p. 053004, 2001.

[19] S. Di Chiara, C. Pica, and F. Sannino, "Flavor Dependence of the S-parameter," *Phys.Lett.*, vol. B700, pp. 229–235, 2011.

[20] U. I. Sondergaard, C. Pica, and F. Sannino, "S-parameter at Non-Zero Temperature and Chemical Potential," *Phys.Rev.*, vol. D84, p. 075022, 2011.

[21] P. A. Boyle, L. Del Debbio, J. Wennekers, and J. M. Zanotti, "The S Parameter in QCD from Domain Wall Fermions," *Phys.Rev.*, vol. D81, p. 014504, 2010.

[22] T. DeGrand, "Oblique correction in a walking lattice theory," 2010.

[23] T. Appelquist *et al.*, "Parity Doubling and the S Parameter Below the Conformal Window," *Phys.Rev.Lett.*, vol. 106, p. 231601, 2011.

[24] D. D. Dietrich, F. Sannino, and K. Tuominen, "Light composite Higgs from higher representations versus electroweak precision measurements: Predictions for CERN LHC," *Phys.Rev.*, vol. D72, p. 055001, 2005.

[25] H. J. Rothe, *Lattice gauge theories: An Introduction*, vol. 74. 2005.

[26] I. Montvay and G. Münster, *Quantum fields on a lattice*. Cambridge Monographs on Mathematical Physics, Cambridge University Press, 1994.

[27] S. Chatrchyan *et al.*, "Observation of a new boson at a mass of 125 GeV with the CMS experiment at the LHC," *Phys.Lett.B*, 2012.

[28] G. Aad *et al.*, "Observation of a new particle in the search for the Standard Model Higgs boson with the ATLAS detector at the LHC," 2012.

[29] H. Nielsen and M. Ninomiya, "Absence of neutrinos on a lattice: (i). proof by homotopy theory," *Nuclear Physics B*, vol. 185, no. 1, pp. 20 – 40, 1981.

[30] E. Follana and H. Panagopoulos, "Critical mass of wilson fermions: A comparison of perturbative and monte carlo results," *Phys. Rev. D*, vol. 63, p. 017501, Dec 2000.

[31] B. Orth, T. Lippert, and K. Schilling, "Finite-size effects in lattice qcd with dynamical wilson fermions," *Phys. Rev. D*, vol. 72, p. 014503, Jul 2005.

[32] M. Luscher, "Volume Dependence of the Energy Spectrum in Massive Quantum Field Theories. 1. Stable Particle States," *Commun.Math.Phys.*, vol. 104, p. 177, 1986.

[33] M. Fukugita, N. Ishizuka, H. Mino, M. Okawa, and A. Ukawa, "Full QCD hadron spectroscopy with two flavors of dynamical Kogut-Susskind quarks on the lattice," *Phys.Rev.*, vol. D47, pp. 4739–4769, 1993.

[34] T. Reisz, "RENORMALIZATION OF LATTICE FEYNMAN INTEGRALS WITH MASSLESS PROPAGATORS," *Commun.Math.Phys.*, vol. 117, p. 639, 1988.

[35] T. Reisz, "LATTICE GAUGE THEORY: RENORMALIZATION TO ALL ORDERS IN THE LOOP EXPANSION," *Nucl.Phys.*, vol. B318, p. 417, 1989.

[36] C. Bernard, S. Hashimoto, D. B. Leinweber, P. Lepage, E. Pallante, *et al.*, "Panel discussion on chiral extrapolation of physical observables," *Nucl.Phys.Proc.Suppl.*, vol. 119, pp. 170–184, 2003.

[37] B. Sheikholeslami and R. Wohlert, "Improved Continuum Limit Lattice Action for QCD with Wilson Fermions," *Nucl.Phys.*, vol. B259, p. 572, 1985.

[38] S. R. Sharpe and J. Singleton, Robert L., “Spontaneous flavor and parity breaking with Wilson fermions,” *Phys.Rev.*, vol. D58, p. 074501, 1998.

[39] G. Rupak and N. Shoresh, “Chiral perturbation theory for the Wilson lattice action,” *Phys.Rev.*, vol. D66, p. 054503, 2002.

[40] O. Bar, G. Rupak, and N. Shoresh, “Chiral perturbation theory at O(a**2) for lattice QCD,” *Phys.Rev.*, vol. D70, p. 034508, 2004.

[41] S. Aoki, “Chiral perturbation theory with Wilson-type fermions including a**2 effects,” *Nucl.Phys.Proc.Suppl.*, vol. 128, pp. 9–17, 2004.

[42] L. Del Debbio and R. Zwicky, “Hyperscaling relations in mass-deformed conformal gauge theories,” *Phys.Rev.*, vol. D82, p. 014502, 2010.

[43] L. Del Debbio, A. Patella, and C. Pica, “Higher representations on the lattice: Numerical simulations. SU(2) with adjoint fermions,” *Phys.Rev.*, vol. D81, p. 094503, 2010.

[44] S. Duane, A. Kennedy, B. Pendleton, and D. Roweth, “Hybrid Monte Carlo,” *Phys.Lett.*, vol. B195, pp. 216–222, 1987.

[45] Y. Saad, *Iterative Methods for Sparse Linear Systems.* Society for Industrial and Applied Mathematics, 2 ed., 2003.

[46] G. Sleijpen and H. Vorst, “Reliable updated residuals in hybrid bi-cg methods,” *Computing*, vol. 56, no. 2, pp. 141–163, 1996.

[47] M. Clark, R. Babich, K. Barros, R. Brower, and C. Rebbi, “Solving Lattice QCD systems of equations using mixed precision solvers on GPUs,” *Comput.Phys.Commun.*, vol. 181, pp. 1517–1528, 2010.

[48] R. Babich, M. Clark, B. Joo, G. Shi, R. Brower, *et al.*, “Scaling Lattice QCD beyond 100 GPUs,” 2011.

[49] A. Hietanen, C. Pica, F. Sannino, and U. I. Sondergaard, “Orthogonal Technicolor with Isotriplet Dark Matter on the Lattice,” *Phys.Rev.*, vol. D87, p. 034508, 2013.

[50] S. Dimopoulos, “Technicoloured signatures,” *Nuclear Physics B*, vol. 168, no. 1, pp. 69 – 92, 1980.

[51] M. E. Peskin, “The alignment of the vacuum in theories of technicolor,” *Nuclear Physics B*, vol. 175, no. 2, pp. 197 – 233, 1980.

[52] C. Vafa and E. Witten, “Parity conservation in quantum chromodynamics,” *Phys. Rev. Lett.*, vol. 53, pp. 535–536, Aug 1984.

[53] M. Gell-Mann, R. J. Oakes, and B. Renner, “Behavior of current divergences under $su_3 \times su_3$,” *Phys. Rev.*, vol. 175, pp. 2195–2199, Nov 1968.

[54] A. Patella, “Gell-mann-oaks-renner-like relation in infrared-conformal gauge theories,” *Phys. Rev. D*, vol. 84, p. 125033, Dec 2011.

[55] J. Wess and J. Bagger, *Supersymmetry and Supergravity*. Princeton University Press, 1983.

[56] S. P. Martin, “A Supersymmetry Primer,” 1997.

[57] E. Witten, “An su(2) anomaly,” *Physics Letters B*, vol. 117, no. 5, pp. 324 – 328, 1982.

[58] R. Lewis, C. Pica, and F. Sannino, “Light Asymmetric Dark Matter on the Lattice: SU(2) Technicolor with Two Fundamental Flavors,” *Phys.Rev.*, vol. D85, p. 014504, 2012.

[59] M. T. Frandsen and F. Sannino, “iTIMP: isotriplet Technicolor Interacting Massive Particle as Dark Matter,” *Phys.Rev.*, vol. D81, p. 097704, 2010.

[60] T. van Ritbergen, J. Vermaseren, and S. Larin, “The Four loop beta function in quantum chromodynamics,” *Phys.Lett.*, vol. B400, pp. 379–384, 1997.

[61] P. de Forcrand and O. Jahn, “Comparison of SO(3) and SU(2) lattice gauge theory,” *Nucl.Phys.*, vol. B651, pp. 125–142, 2003.

[62] F. Bursa, R. Lau, and M. Teper, “SO(2N) and SU(N) gauge theories in 2+1 dimensions,” *JHEP*, vol. 1305, p. 025, 2013.

[63] A. Kennedy, I. Horvath, and S. Sint, “A New exact method for dynamical fermion computations with nonlocal actions,” *Nucl.Phys.Proc.Suppl.*, vol. 73, pp. 834–836, 1999.

[64] T. Appelquist and F. Sannino, “The Physical spectrum of conformal SU(N) gauge theories,” *Phys.Rev.*, vol. D59, p. 067702, 1999.

[65] M. Luscher, “Some Analytic Results Concerning the Mass Spectrum of Yang-Mills Gauge Theories on a Torus,” *Nucl.Phys.*, vol. B219, pp. 233–261, 1983.

[66] P. van Baal, “SU(N) YANG-MILLS SOLUTIONS WITH CONSTANT FIELD STRENGTH ON T**4,” *Commun.Math.Phys.*, vol. 94, p. 397, 1984.

[67] J. Koller and P. van Baal, “A NONPERTURBATIVE ANALYSIS IN FINITE VOLUME GAUGE THEORY,” *Nucl.Phys.*, vol. B302, p. 1, 1988.

[68] Z. Fodor, K. Holland, J. Kuti, D. Nogradi, and C. Schroeder, “Chiral properties of SU(3) sextet fermions,” *JHEP*, vol. 0911, p. 103, 2009.

[69] Z. Fodor, K. Holland, J. Kuti, D. Nogradi, C. Schroeder, *et al.*, “Can the nearly conformal sextet gauge model hide the Higgs impostor?,” *Phys.Lett.*, vol. B718, pp. 657–666, 2012.

[70] Y. Shamir, B. Svetitsky, and T. DeGrand, “Zero of the discrete beta function in SU(3) lattice gauge theory with color sextet fermions,” *Phys.Rev.*, vol. D78, p. 031502, 2008.

[71] T. DeGrand, Y. Shamir, and B. Svetitsky, “Mass anomalous dimension in sextet QCD,” 2012.

[72] N. Tanimura and O. Tanimura, “Recursion relation of character expansion coefficient in SU(3) lattice gauge theory,” *J.Math.Phys.*, vol. 31, pp. 721–724, 1990.

[73] Z. Fodor, K. Holland, J. Kuti, D. Nogradi, C. Schroeder, *et al.*, “Twelve fundamental and two sextet fermion flavors,” 2012.

PHYSICAL REVIEW D **84,** 075022 (2011)

S parameter at nonzero temperature and chemical potential

Ulrik Ishøj Søndergaard,[*] Claudio Pica,[†] and Francesco Sannino[‡]
CP^3*-Origins and DIAS, Campusvej 55, DK-5230 Odense M, Denmark*

(Received 19 August 2011; published 24 October 2011)

We compute the finite-temperature and matter density corrections to the S-parameter at the one-loop level. At nonzero temperature T and matter density μ Lorentz symmetry breaks and therefore we suggest a suitable generalization of the S-parameter. By computing the plasma correction, we discover a reduction of the S-parameter in the physically relevant region of small external momenta for any nonzero μ and T. In particular, the S-parameter vanishes at small m/T, where m is the mass of the fermions, due to the finite extent of the temporal direction. Our results are directly applicable to the determination of the S-parameter via first-principle lattice simulations performed with antiperiodic boundary conditions in the temporal direction.

DOI: 10.1103/PhysRevD.84.075022 PACS numbers: 14.80.Tt, 11.25.Hf, 12.15.Lk

I. INTRODUCTION

Models of dynamical electroweak symmetry breaking are quickly gaining momentum. The reason why these models featuring uncolored techniquarks are harder to constrain, even at the LHC, is that they typically predict a heavier spectrum, compared to the electroweak scale, of new particles.[1] For this reason it is interesting to analyze the indirect constraints from electroweak precision data established at LEP. It is well known that any extension of the standard model replacing the electroweak symmetry breaking sector can be constrained analyzing the electroweak gauge bosons vacuum polarizations as proved long time ago by Kennedy and Lynn [1]. Indirect constraints were therefore set using LEP results via the S, T and U parameters, or any linear combinations of them in [1–4]. It is therefore crucial to gain as much information as possible about these important correlators. In particular, the S-parameter is especially relevant for models of electroweak symmetry breaking. Several estimates have appeared in the literature making use of model computations [5–17] and/or first-principle lattice computations [18,19]. The latter ones are necessarily carried out on finite lattices, i.e. at finite volume and temperature. Surprisingly the finite size corrections to such parameters have not yet been investigated. Here we analyze the impact of the finite-temperature corrections on the S-parameter.

This correlator can be determined for any asymptotically free gauge theory with matter transforming according to a given representation of a generic underlying gauge group. Once the number of colors of the new gauge dynamics is fixed, we can have a number of distinct phases in which the theory can exist. For example, it can display large distance conformality or break the global chiral symmetries spontaneously. In both cases this correlator is well defined [12–14] and worth computing.

We provide here the first one loop determination of the S-parameter at nonzero matter density μ and temperature T. These computations are either under perturbative control when applied to the upper end of the conformal window or can be viewed as naive estimates, à la Peskin and Takeuchi, when used below the conformal window. Since at nonzero temperature and matter density Lorentz symmetry breaks we suggest a suitable generalization of the S-parameter and investigate the various limits in the ratios of the relevant energy scales.

In Sec. II we compute the plasma corrections to the S-parameter and we show that, at small external momenta, it is reduced with respect to the zero T and μ case. We consider different limits for which analytical expressions can be derived, better elucidating the physical results.

In Sec. III we discuss the relevance of our results for lattice determinations of the S-parameter and we finally conclude in Sec. IV.

A detailed derivation of our results is provided in the Appendices.

II. THE *S*-PARAMETER AT NONZERO TEMPERATURE AND CHEMICAL BARYON POTENTIAL

The definition of the S-parameter used by He, Polonsky and Su [20] and in [12,14] is

$$S = -16\pi \frac{\Pi_{3Y}(k^2) - \Pi_{3Y}(0)}{k^2}, \tag{1}$$

where Π_{3Y} is the vacuum polarization of the third component of the isospin into the hypercharge current, and we have used, as a reference point, an external momentum k^2, instead of the usual Z boson mass. The S-paramter in Eq. (1) also depends on the fermion masses m_u, m_d.

---

[*] sondergaard@cp3.sdu.dk
[†] pica@cp3-origins.net
[‡] sannino@cp3-origins.net

[1] Light states can also be present, depending on the specific dynamics. Here we are referring to the QCD-like states.

The definition by Peskin and Takeuchi [2] is recovered in the $k^2 \to 0$ limit:

$$S = -16\pi \frac{d\Pi_{3Y}(k^2)}{dk^2}\bigg|_{k^2=0}. \tag{2}$$

At nonzero temperature, Lorentz invariance breaks, and therefore one should differentiate between the temporal and spatial components of the 4-momentum k. Also several new scales will enter in the definition of the S-parameter.

The partition function of a four-dimensional field theory with (anti)periodic boundary conditions in the Euclidianized temporal direction coincides with the partition function of a three-dimensional theory at finite temperature. The compactification of the temporal direction makes k^0 discrete. For a pedagogical introduction of the formalism we refer to the book by J. I. Kapusta and C. Gale [21]. For a system in thermal equilibrium at temperature T and chemical baryon potential μ, the allowed frequencies have values $k^0 = i\omega_n + \mu$ where $\omega_n = 2n\pi T$ for bosons and $\omega_n = (2n+1)\pi T$ for fermions.

At nonzero temperature, we extend the definition of the He-Polonsky-Su S-parameter in the following way:

$$S^{\mu\nu}(m_u, m_d, x, k^2, T, \mu) = -16\pi \frac{\Pi_{3Y}^{\mu\nu}(m_u, m_d, x, k^2, T, \mu) - \Pi_{3Y}^{\mu\nu}(m_u, m_d, x, 0, T, \mu)}{k^2}, \tag{3}$$

with the reference external 4-momentum given by $(k_0, \mathbf{k})$ with $k_0 = x|\mathbf{k}|$ and $k^2 = k_0^2 - \mathbf{k}^2$. Note that the external 4-momentum can also be written as

$$\begin{pmatrix} k_0 \\ |\mathbf{k}| \end{pmatrix} = \begin{pmatrix} k\cosh\eta \\ k\sinh\eta \end{pmatrix}, \qquad x = \coth\eta \geq 1, \tag{4}$$

with η the rapidity of the 4-vector $(k_0, \mathbf{k})$. As expected from the breaking of Lorentz invariance, the generalized S-parameter in Eq. (3) does not depend only on k^2, but also on $x = \coth\eta$.

We also extend the Peskin-Takeuchi definition at finite temperature, by taking the limit $k^2 \to 0$ of Eq. (3):

$$S^{\mu\nu}(m_u, m_d, x, T, \mu) = -16\pi \frac{d\Pi_{3Y}^{\mu\nu}(m_u, m_d, x, k^2, T, \mu)}{dk^2}\bigg|_{k^2=0}. \tag{5}$$

The complete expressions for the finite temperature $\Pi_{3Y}^{\mu\nu}(m_u, m_d, x, k^2, T, \mu)$ and the S-parameter are derived in Appendix B. To make contact with the zero temperature S-parameter we still consider the term proportional to $g^{\mu\nu}$. This is, according to us, a natural choice of extending the S-parameter at nonzero temperature and chemical potential. Furthermore, we have explicitly checked, see Appendix B, that in the degenerate fermion mass limit $S^{\mu\nu} = Sg^{\mu\nu}$.

The S-parameter being a pure number can only depend on adimensional ratios of the physical scales entering in its definition. In the case of degenerate u- and d-type fermions we have $m_u = m_d = m$, and the S-parameter will only depend on the pure numbers x, k^2/m^2, βm and $\beta\mu$: $S(m, x, k^2, T, \mu) = S(x, k^2/m^2, \beta m, \beta\mu)$. As shown in Appendix B, the total S-parameter is given by its zero temperature and zero chemical baryon potential part S_0 plus a plasma contribution S_+: $S = S_0 + S_+$. The explicit expression of the plasma contribution to the S-parameter is given by

$$\begin{aligned} &S_+(x, (k/m)^2, \beta m, \beta\mu) \\ &\quad = \frac{\sharp}{6\pi} \int_0^\infty dq q^2 24 \frac{\tilde{F}(\beta m, \beta\mu, q)}{\sqrt{1+q^2}} \\ &\qquad \times \left(\frac{\sqrt{x^2-1}\ln(\frac{u_+}{u_-})}{4q\frac{k}{m}} + \frac{x^2-1}{2(q^2(x^2-1)+x^2)} \right) \left(\frac{m}{k} \right)^2, \end{aligned} \tag{6}$$

where we used the shorthand notation:

$$u_\pm = \pm 4\frac{k}{m} q\sqrt{x^2-1} + \frac{k^2}{m^2}(x^2-1) - 4(x^2 + q^2(x^2-1)), \tag{7}$$

and the function $\tilde{F}$ is defined as:

$$\begin{aligned} \tilde{F}(\beta m, \beta\mu, q) = &\frac{1}{\exp(\beta m\sqrt{1+q^2} - \beta\mu) + 1} \\ &+ \frac{1}{\exp(\beta m\sqrt{1+q^2} + \beta\mu) + 1}. \end{aligned} \tag{8}$$

In Eq. (6), the factor $\sharp = d[r]N_f/2$ accounts for $N_D = N_f/2$ doublets of fermions in the representation r with dimension $d[r]$ of the gauge group. To understand the plasma contribution to the S-parameter, we plot in Fig. 1 the finite-temperature S-parameter, in the case $\mu = 0$, as a function of k^2/m^2 for a particular value of βm. The zero-temperature part S_0 was computed in [12] and it is displayed for comparison by the dashed-dotted lines (the real part corresponds to the thick line, while the imaginary part to the thin line). The plasma contribution S_+ is shown by the dashed lines, and the total S-parameter is displayed by the solid lines. As we will show below with a direct computation, S_+ vanishes in the zero-temperature limit as expected. At nonzero temperature the structure of the real and imaginary parts of S_+ is similar to the one of S_0, and, at small k^2/m^2, reduces the total S-parameter. When increasing the temperature, S_+ grows in absolute value, and in the limit $\beta m \to 0$ exactly cancels the zero-temperature part, so that the S-parameter vanishes in this limit. In the case of

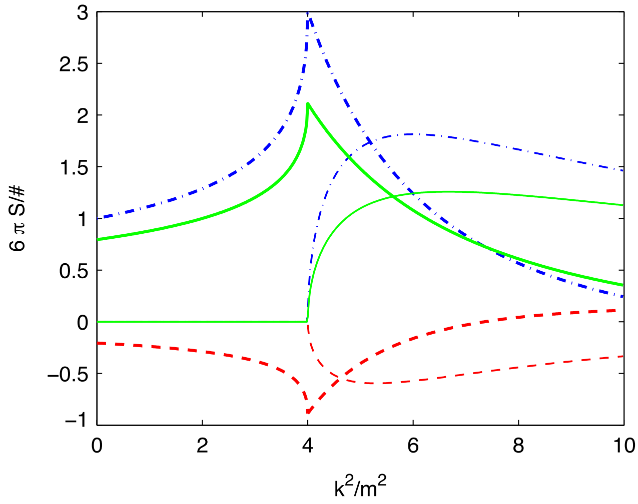

FIG. 1 (color online). The finite-temperature S-parameter (3) (real part: thick solid line, imaginary part: thin solid line) is given by the sum of the zero-temperature part S_0 (dashed-dotted lines) and a plasma contribution S_+ (6) (dashed lines). In this plot $\coth\eta = x = \sqrt{2}$, $\mu = 0$ and $\beta m = 1$.

zero chemical potential, this cancellation is encoded directly in the Matsubara frequency sum formula (B3). Physically one can understand this cancellations by recalling that in this limit the fermions decouple.

Adding a nonzero chemical potential does not alter this picture, as we shall see below, and a similar reduction at small k^2/m^2 is observed.

A. The $k^2/m^2 \rightarrow 0$ limit

Starting from Eq. (6) we expand the term in parenthesis as a power series in k^2/m^2. We have

$$\sqrt{x^2-1}\,\frac{\ln(\frac{u_+}{u_-})}{4q\frac{k}{m}} + \frac{x^2-1}{2(q^2(x^2-1)+x^2)} = \sum_{i=1}^{\infty} a_i\left(\frac{k^2}{m^2}\right)^i, \quad (9)$$

where the first coefficients in the expansion are

$$a_1 = -\frac{(x^2-1)^2(q^2(3x^2+1)+3x^2)}{24(q^2(x^2-1)+x^2)^3}, \quad (10)$$

$$a_2 = -\frac{(x^2-1)^3(q^4(5x^4+10x^2+1)+10q^2(x^4+x^2)+5x^4)}{160(q^2(x^2-1)+x^2)^5}. \quad (11)$$

By inserting the expansion in Eq. (9) into Eq. (6), we obtain

$$S_+ = \frac{\sharp}{6\pi}\sum_{j=0}^{\infty} C_j\left(\frac{k^2}{m^2}\right)^j, \quad (12)$$

where

$$C_j(x, \beta m, \beta\mu) = 24\int_0^\infty dq q^2 \frac{\tilde{F}(\beta m, \beta\mu, q)}{\sqrt{1+q^2}} a_{j+1}. \quad (13)$$

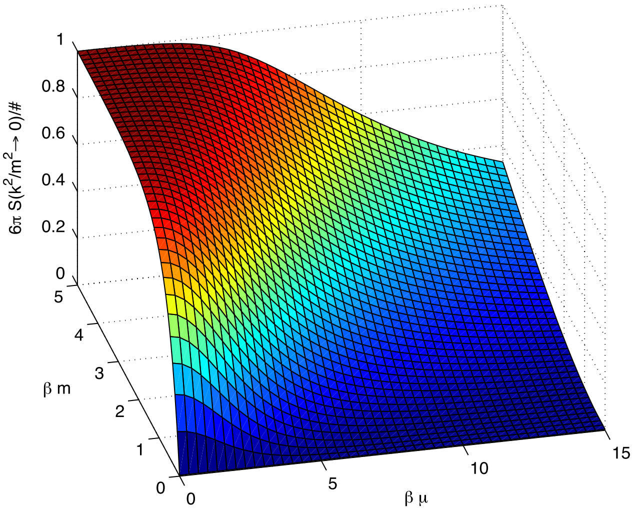

FIG. 2 (color online). The generalized S-parameter in Eq. (5) at finite temperature and chemical potential for $\coth\eta = x = \sqrt{2}$.

The generalized S-parameter in Eq. (5) can be easily read from the above expression:

$$S(k^2/m^2 \rightarrow 0) = \frac{\sharp}{6\pi}[1 + C_0(x, \beta m, \beta\mu)]. \quad (14)$$

We plot in Fig. 2 the generalized S-parameter in Eq. (5) and (14) as a function of the temperature and chemical potential. We find the interesting result that the S-parameter reduces in the presence of nonzero temperature and/or chemical potential.

We have already discussed why the S-parameter is reduced at small k^2/m^2 at high temperature. The decrease as a function of the chemical potential is due to the fact that only one species of fermions survives at large μ, effectively restoring chiral symmetry. At large chemical potential there will be instabilities at the Fermi surface leading to the breaking of the vacuum, which we are not considering here.

B. High-temperature limit

In the limit of large temperature $\beta m \rightarrow 0$, we expand $\tilde{F}$ as a power series in βm:

$$\tilde{F}(\beta m, \beta\mu) = 1 - \mathrm{sech}^2\left(\frac{1}{2}\beta\mu\right)\frac{1}{2}\sqrt{1+q^2}\,\beta m + \mathcal{O}(\beta^3 m^3), \quad (15)$$

and insert this expansion in the integral defining S_+ (6). The first term in the expansion (15), constant in βm, gives a contribution which is identical in size but opposite in sign to the zero temperature S-parameter S_0. The second term, linear in βm, can also be computed leading to

$$S_+ = -S_0 + \mathrm{sech}^2\left(\frac{1}{2}\beta\mu\right)\cosh(\eta)S_+^{(1)}(k^2/m^2)(\beta m) + \mathcal{O}(\beta^3 m^3), \tag{16}$$

where:

$$S_+^{(1)}(k^2/m^2) = \frac{3\pi}{k^2/m^2}\left(1 + i\sqrt{\frac{1}{4}\frac{k^2}{m^2} - 1}\right). \tag{17}$$

In the limit $k^2/m^2 \to 0$ the generalized S-parameter in Eq. (5) is given by

$$S(k^2/m^2 \to 0) = \frac{\sharp}{16}\mathrm{sech}^2\left(\frac{1}{2}\beta\mu\right)\cosh(\eta)(\beta m) + \mathcal{O}(\beta^3 m^3). \tag{18}$$

Interestingly we note that, in this limit, the contribution to S-parameter depending on $\beta\mu$, η, k^2/m^2 and βm all factorize.

C. Low-temperature limit

When the ratio βm is large enough, corresponding to the low-temperature limit of the theory, we expect to recover the familiar zero-temperature result. To show that this is indeed the case, we start from the expression for S_+ in Eq. (6) and perform a change of variable and rewrite the integral in terms of the new variable $Q = \beta m(\sqrt{1+q^2} - 1)$. We then expand the integrand as an asymptotic series for large βm. In the final expression the dependence on the chemical potential factorizes, as in the case of the high-temperature expansion. This can be easily seen as, at large βm, the function $\tilde{F}$ appearing in Eq. (6) can be approximated by

$$\tilde{F}(\beta m, \beta\mu) \approx 2\cosh(\beta\mu)e^{-\beta m\sqrt{1+q^2}}. \tag{19}$$

Keeping only the first term in the expansion of S we obtain

$$S_+ = -\frac{\sharp}{6\pi}\frac{\cosh(\beta\mu)\mathrm{sech}^4(\eta)}{1 - \left(\frac{k/m}{2\cosh\eta}\right)^2} \times \frac{3\sqrt{2\pi}}{(\beta m)^{3/2}}e^{-\beta m}\cdot\left(1 + \mathcal{O}\left(\frac{1}{\beta m}\right)\right). \tag{20}$$

Higher order terms in the expansion can easily be obtained in the same way.

The final expression (16) contains an exponential Boltzmann-like suppression factor as expected.

We compare the high- and low-temperature expansions in Eq. (16) and (20) to the complete numerical result for the generalized S-parameter in the $k^2/m^2 \to 0$ limit in Fig. 3. The expansions converge within their respective domain of validity temperature regions.

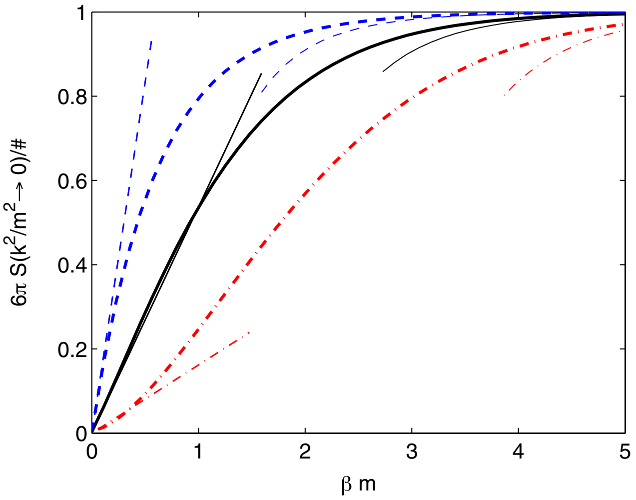

FIG. 3 (color online). The generalized S-parameter in Eq. (5) (thick lines) at finite temperature and chemical potential as compared to the high-temperature (16) and low-temperature (20) expansions. The three different curves correspond to $\beta\mu = 0$ (top, dashed line), $\beta\mu = 2.33$ (middle, solid line) and $\beta\mu = 4.33$ (bottom, dashed-dotted line). In this plot we use $\coth\eta = \sqrt{2}$.

We also note that the accuracy of the low-temperature expansion in Eq. (20) depends critically on the value of k^2/m^2 as the coefficient of the first term in the expansion diverges for $k/m = 2\cosh\eta$. This divergence is unphysical, as it is clear from the fact that it is not present in the full expression. We compare in Fig. 4 the value of S_+ with its asymptotic expansion at low-temperature for a finite, low value of the temperature $\beta m = 5$ and at finite density $\beta\mu = 3$. The dip at $k^2/m^2 = 4$ of S_+ is the kinematical threshold.

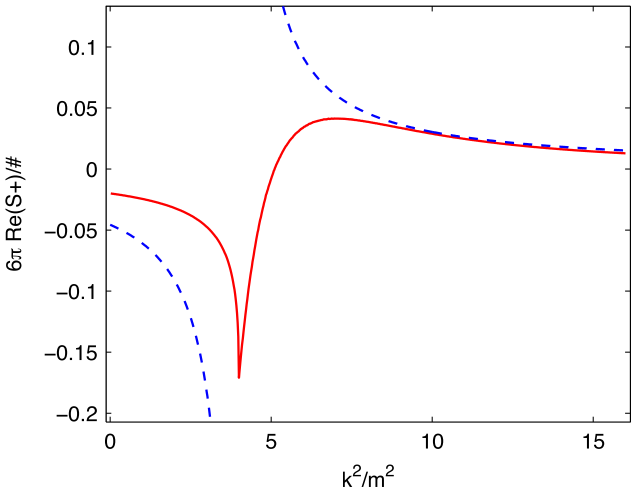

FIG. 4 (color online). The plasma contribution to the S-parameter (6) (solid line) at finite temperature $\beta m = 5$ and finite chemical potential $\beta\mu = 3$ compared to the low-temperature expansion (20) (dashed line).

III. APPLICATIONS TO LATTICE FIELD THEORY

Our result can be used to estimate the finite-temperature corrections to the S-parameter as computed using numerical lattice simulations. These are typically performed at nonzero temperature, when antiperiodic boundary conditions are used in the temporal direction, so that it is crucial to disentangle the finite-temperature effects to extrapolate to zero temperature. We demonstrated that the S-parameter in the phenomenologically relevant parameter region of small external momenta, is reduced by the effects of nonzero temperature. The smaller is βm the larger the negative corrections. There is also a dependence on the rapidity η which has to be taken into account. At large βm such a dependence disappears, while it increases at smaller βm. This dependence is shown in Fig. 5. In the large rapidity regime, corresponding to $x \to 1$, one approaches the zero-temperature result. This can be better understood considering that in this limit the temporal and spatial momentum both diverge in order to keep k^2 finite, as required by our definition of the S-parameter.

To better elucidate the size of the corrections to the S-parameter, we plot in Fig. 6 the contour lines of S/S_0 in the $\beta m - \coth\eta$ plane. We also show in Fig. 7 the contour plots of S/S_0 as a function of βm and $\beta\mu$, for $\coth\eta = \sqrt{2}$ corresponding to Fig. 2.

To compare to the lattice results, we show in Fig. 8 the dependence on the fermion masses of the S-parameter at zero chemical potential and finite T for two different values of the reference momentum k^2. The decrease in S at small m is not due to a chiral restoration but the finite-temperature corrections. From Fig. 8 it is possible to estimate the range of masses for which a reliable estimate of the S-parameter can be extracted from lattice results, assuming that the infinite volume regime has been reached.

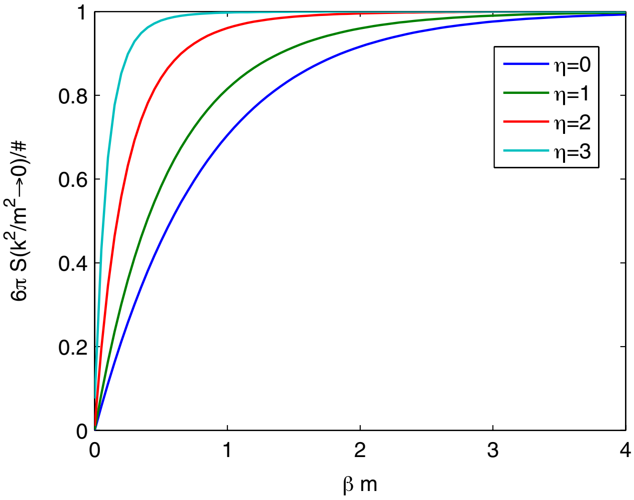

FIG. 5 (color online). The rapidity dependence of the S-parameter in the limit $k^2/m^2 \to 0$ for $\mu = 0$. The finite-temperature corrections vanish at large rapidity. The curves correspond to different values of the rapidity ranging from $\eta = 0$ (lowermost) to $\eta = 3$ (uppermost).

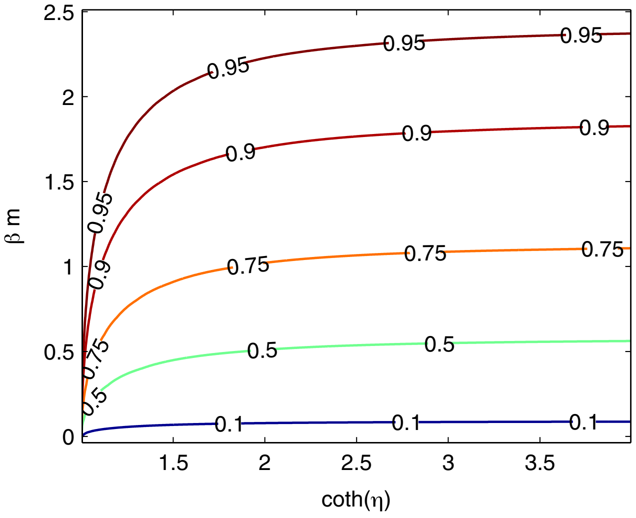

FIG. 6 (color online). Contour plot of S/S_0 at $\mu = 0$.

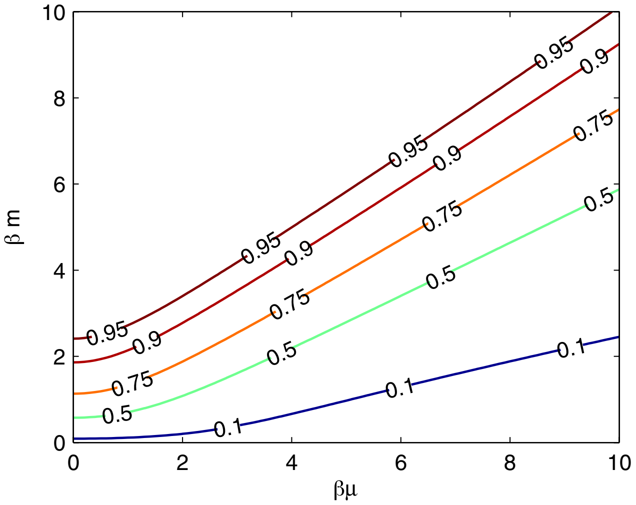

FIG. 7 (color online). Contour plot of S/S_0 for $\coth\eta = \sqrt{2}$ corresponding to Fig. 2.

In order to be able to directly compare with lattice results we need to consider two cases. In a theory displaying large distance conformality the relevant mass scale, at infinite volume and zero temperature, is the explicit femion mass term. Therefore in the conformal window our computations are directly applicable and reliable in the Banks-Zaks regime. In a theory developing a chiral condensate dynamically such as QCD our computations constitute an extremely crude estimate of the thermal corrections upon identifying the fermion mass m with the dynamical generated mass scale. Having in mind these two different regimes we can now revisit recent lattice determinations of the S-parameter. For example, Boyle *et al.* [19] determined the S-parameter in lattice QCD with 2 + 1 fermion

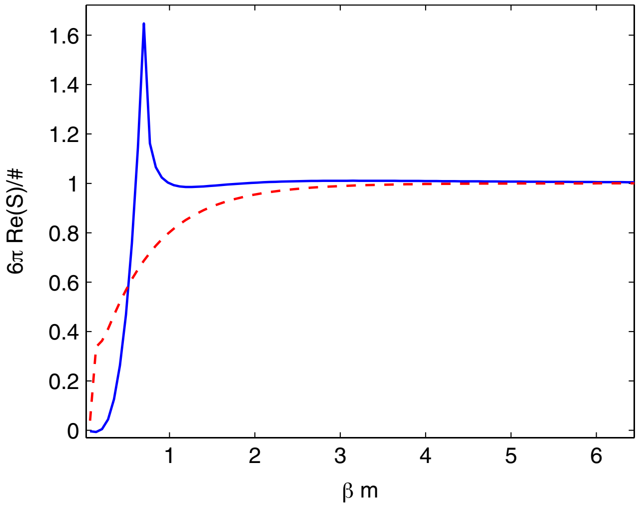

FIG. 8 (color online). S-parameter at finite temperature as a function of the fermions mass for $k^2\beta^2 = 0.1$ (dashed line) and $k^2\beta^2 = 2$ (solid line). In this figure $\coth\eta = \sqrt{2}$.

flavors. Using the vector meson masses as an extremely naive measure of the chiral scale of the theory i.e. $m \sim \Lambda \sim m_\rho$ one has $\beta m \sim m_\rho L_0$ where L_0 is the lattice temporal extension. For the lowest quark mass used in their work one then has $\beta m_\rho \simeq 11$ which is well beyond the point around $\beta m \simeq 2.5$ where the thermal corrections become important, say above 5%, as shown in Fig. 7. Similarly the results reported by the LSD Collaboration [22] seem also away from substantial thermal corrections having $\beta m_\rho \simeq 16$.

In the work by DeGrand [23] the S-parameter is determined for a $SU(3)$ gauge theory with two flavors in the sextet representation. If this theory is below the conformal window, thermal effects are expected to be small for the setup used since $\beta m_\rho \simeq 6.6$. However, if the theory is conformal the relevant mass is the quark mass yielding a βm ranging between ~0.4 and 1.2. This suggests potentially significant thermal corrections.

Furthermore, and independently from thermal corrections, lattice computations should also carefully choose the kinematical regime in which the interesting S-parameter should be measured. Since, as first noted in [12–14] the order of the limits is crucial. Considering the aforementioned lattice simulations we find that the first two lattice determinations [19,22] are approaching the k^2/m^2 zero limit while the third one seems still far away from this limit, having a ratio larger than 10 (see figure 12 of [23]).

IV. CONCLUSIONS

In this work we provided a suitable generalization of the S-parameter at nonzero temperature and chemical potential. By computing the plasma contributions S_+ we discovered a reduction of the S-parameter in the physically relevant region of small k^2/m^2 for any nonzero μ and T. Our results are directly applicable to the determination for the S-parameter via first-principle lattice simulations performed with antiperiodic boundary conditions in the temporal direction. In this case we find that the vanishing of the S-parameter at small βm is due to the finite extent of the temporal direction.

We have explicitly compared our results with the most recent lattice determinations, however finite spatial volume corrections, which can be sizable, still need to be investigated.

ACKNOWLEDGMENTS

The authors acknowledge the useful discussions with Tuomas Hapola and Stefano Di Chiara in the initial stages of this work.

APPENDIX A: VACUUM CONTRIBUTION TO THE *S*-PARAMETER

At zero temperature $T = 0$ and chemical potential $\mu = 0$, the perturbative expression for the S-parameter, as defined by He, Polonsky and Su, has been calculated at one-loop in [20] and at two-loop in [24]. At one-loop order the He-Polonsky-Su S-parameter, as defined in Eq. (1), reads

$$S = \frac{N_D d[r]}{6\pi}\bigg\{2(4Y+3)z_u + 2(-4Y+3)z_d - 2Y\log\left(\frac{z_u}{z_d}\right) + \left[\left(\frac{3}{2}+2Y\right)z_u + Y\right]G(z_u) + \left[\left(\frac{3}{2}-2Y\right)z_d - Y\right]G(z_d)\bigg\}, \tag{A1}$$

with

$$G(z) = -4\sqrt{4z-1}\arctan\left(\frac{1}{\sqrt{4z-1}}\right),$$

where Y is the hypercharge, $z_i = m_i^2/k^2$, $i = u, d$, m_i is the mass of the fermionic species and $N_D = N_f/2$ is the number of doublets transforming under a technicolor group representation r with dimension $d[r]$.

APPENDIX B: DETAILED CALCULATION OF PLASMA CONTRIBUTION TO THE *S*-PARAMETER

The S-parameter can be written in terms of the following vacuum polarization amplitudes:

$\Pi^{\mu\nu}_{LL}(m_u, m_d) =$

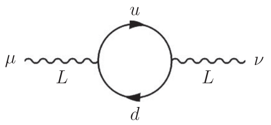

,

$\Pi^{\mu\nu}_{LR}(m_u, m_d) =$

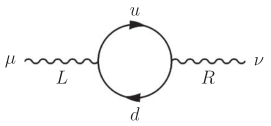

,

TABLE I. Hypercharge and isospin assignments for the fermions. y is an arbitrary real number.

	T^3	Y
u_L	$1/2$	$y/2$
u_R	0	$(y+1)/2$
d_L	$-1/2$	$y/2$
d_R	0	$(y-1)/2$

where the wavy lines represent electroweak gauge bosons, once we specify the hypercharge and isospin of the fermion doublets. We use the choice of Table I. The amplitude $\Pi_{3Y}^{\mu\nu}$, entering in the S-parameter, can then be constructed in terms of $\Pi_{LL}^{\mu\nu}$ and $\Pi_{LR}^{\mu\nu}$. We have

$$\begin{aligned} 4\Pi_{3Y}^{\mu\nu}(k, m_u, m_d) = {} & y[\Pi_{LL}^{\mu\nu}(k, m_u, m_u) + \Pi_{LR}^{\mu\nu}(k, m_u, m_u)] \\ & - y[\Pi_{LL}^{\mu\nu}(k, m_d, m_d) + \Pi_{LR}^{\mu\nu}(k, m_d, m_d)] \\ & + \Pi_{LR}^{\mu\nu}(k, m_u, m_u) + \Pi_{LR}^{\mu\nu}(k, m_d, m_d). \end{aligned} \tag{B1}$$

In the equations above we have suppressed the explicit dependence on the temperature T and the chemical potential μ. In the case of degenerate fermion masses, $\Pi_{3Y}^{\mu\nu}(k)$ becomes independent of the particular choice of hypercharge, and we have

$$\Pi_{3Y}^{\mu\nu}(k, m) = \frac{1}{2}\Pi_{LR}^{\mu\nu}(k, m). \tag{B2}$$

Evaluation of diagrams

The explicit expression for the amplitudes, at finite temperature and chemical potential, have the form:

$$\begin{aligned} \Pi_{LH}^{\mu\nu} = {} & T\sum_{l=-\infty}^{\infty}\int\frac{d^3\mathbf{p}}{(2\pi)^3} \\ & \times \mathrm{Tr}\bigg[\gamma^\mu P_L \frac{\not{p}+m}{p^2-m^2}\gamma^\nu P_H \frac{\not{k}+\not{p}+m}{(k+p)^2-m^2}\bigg], \end{aligned}$$

where $p^0 = i(2l+1)\pi T + \mu$ and $H = L, R$. Let $N_{LH}^{\mu\nu}$ denote the numerator of the expression in square brackets. By evaluating the traces we get

$$\begin{aligned} N_{LL}^{\mu\nu} &= 2[p^\mu(p+k)^\nu + p^\nu(p+k)^\mu - p\cdot(p+k)g^{\mu\nu}], \\ N_{LR}^{\mu\nu} &= 2m^2 g^{\mu\nu}. \end{aligned}$$

Introducing the shorthand

$$b = (p^0 + k^0)^2 - \mathbf{p}^2 - \mathbf{k}^2 - m^2,$$

we can rewrite the amplitude in a more compact form:

$$\Pi_{LH}^{\mu\nu} = T\sum_{l=-\infty}^{\infty}\int\frac{d\mathbf{p}^3}{(2\pi)^3}\frac{1}{p^2-m^2}\cdot\frac{N_{LH}^{\mu\nu}}{b - 2|\mathbf{p}\,\|\,\mathbf{k}|\cos\theta}.$$

We now use the Matsubara frequency sum formula (see e.g. [21])

$$\begin{aligned} T\sum_{l=-\infty}^{\infty} f(p^0) = {} & \frac{i}{2\pi}\int_{-i\infty+\mu+\varepsilon}^{+i\infty+\mu+\varepsilon} dp^0 f(p^0)\tilde{f}(p^0-\mu) \\ & + \frac{i}{2\pi}\int_{-i\infty+\mu-\varepsilon}^{+i\infty+\mu-\varepsilon} dp^0 f(p^0)\tilde{f}(\mu-p^0) \\ & - \frac{i}{2\pi}\oint_C dp^0 f(p^0) - \frac{i}{2\pi}\int_{-i\infty}^{i\infty} dp^0 f(p^0), \end{aligned} \tag{B3}$$

to evaluate the sum over the frequencies. In this expression C is a rectangular path $(i\infty, -i\infty+\mu)$ going counterclockwise and $\tilde{f}(p^0) = (e^{\beta p^0}+1)^{-1}$ where $\beta = T^{-1}$. This formalism allows for a neat separation of the vacuum contribution $\Pi_{LH,0}^{\mu\nu} = \Pi_{LH}^{\mu\nu}|_{T,\mu=0}$ and the plasma contribution $\Pi_{LH,+}^{\mu\nu} = \Pi_{LH}^{\mu\nu} - \Pi_{LH,0}^{\mu\nu}$. The last term in the sum formula gives the zero temperature and chemical potential, and reads:

$$\Pi_{LH,0}^{\mu\nu}(k) = -i\int\frac{d^4p}{(2\pi)^4}\frac{1}{p^2-m^2}\cdot\frac{N_{LH}^{\mu\nu}}{b - 2|\mathbf{p}\,\|\,\mathbf{k}|\cos\theta}.$$

For evaluation of this term we refer to standard textbooks, see e.g. Peskin and Schroeder [25]. The final result for this integral corresponds to the S-parameter as stated in (A1).

In this paper we compute $\Pi_{LH,+}^{\mu\nu}$. We first consider the case where no poles are contained inside the closed path C. This depends on the values of the chemical potential μ and the external momentum. In this case only the first two integrals contribute to the result:

$$\begin{aligned} \Pi_{LH,+}^{\mu\nu} = {} & i\int_{-i\infty+\mu+\varepsilon}^{i\infty+\mu+\varepsilon}\frac{dp^0}{2\pi}\int\frac{d^3\mathbf{p}}{(2\pi)^3}\frac{1}{p^2-m^2}\frac{N_{LH}^{\mu\nu}}{b - 2|\mathbf{p}\,\|\,\mathbf{k}|\cos\theta}\tilde{f}(p^0-\mu) \\ & + i\int_{-i\infty+\mu-\varepsilon}^{i\infty+\mu-\varepsilon}\frac{dp^0}{2\pi}\int\frac{d^3\mathbf{p}}{(2\pi)^3}\frac{1}{p^2-m^2}\frac{N_{LH}^{\mu\nu}}{b - 2|\mathbf{p}\,\|\,\mathbf{k}|\cos\theta}\tilde{f}(\mu-p^0). \end{aligned}$$

Changing to spherical coordinates the angular part of the integration over **p** can be performed (note that also $N_{LL}^{\mu\nu}$ depends on the angle θ). The results for the two amplitudes are

$$\begin{aligned}\Pi_{LL,+}^{\mu\nu} &= i\int_{-i\infty+\mu+\varepsilon}^{i\infty+\mu+\varepsilon}\frac{dp^0}{2\pi}\int_0^\infty\frac{d|\mathbf{p}\,\|\,\mathbf{p}|^2}{(2\pi)^2}\frac{2\tilde{f}(p^0-\mu)}{p^2-m^2}\left[\frac{a^{\mu\nu}+bg^{\mu\nu}}{4|\mathbf{p}\,\|\,\mathbf{k}|}\ln\left(\frac{b+2|\mathbf{p}\,\|\,\mathbf{k}|}{b-2|\mathbf{p}\,\|\,\mathbf{k}|}\right)-g^{\mu\nu}\right]\\ &\quad + i\int_{-i\infty+\mu-\varepsilon}^{i\infty+\mu-\varepsilon}\frac{dp^0}{2\pi}\int_0^\infty\frac{d|\mathbf{p}\,\|\,\mathbf{p}|^2}{(2\pi)^2}\frac{2\tilde{f}(\mu-p^0)}{p^2-m^2}\left[\frac{a^{\mu\nu}+bg^{\mu\nu}}{4|\mathbf{p}\,\|\,\mathbf{k}|}\ln\left(\frac{b+2|\mathbf{p}\,\|\,\mathbf{k}|}{b-2|\mathbf{p}\,\|\,\mathbf{k}|}\right)-g^{\mu\nu}\right],\\ \Pi_{LR,+}^{\mu\nu} &= i\int_{-i\infty+\mu+\varepsilon}^{i\infty+\mu+\varepsilon}\frac{dp^0}{2\pi}\int_0^\infty\frac{d|\mathbf{p}\,\|\,\mathbf{p}|^2}{(2\pi)^2}\frac{2\tilde{f}(p^0-\mu)}{p^2-m^2}\frac{N_{LR}^{\mu\nu}}{4|\mathbf{p}\,\|\,\mathbf{k}|}\ln\left(\frac{b+2|\mathbf{p}\,\|\,\mathbf{k}|}{b-2|\mathbf{p}\,\|\,\mathbf{k}|}\right)\\ &\quad + i\int_{-i\infty+\mu-\varepsilon}^{i\infty+\mu-\varepsilon}\frac{dp^0}{2\pi}\int_0^\infty\frac{d|\mathbf{p}\,\|\,\mathbf{p}|^2}{(2\pi)^2}\frac{2\tilde{f}(\mu-p^0)}{p^2-m^2}\frac{N_{LR}^{\mu\nu}}{4|\mathbf{p}\,\|\,\mathbf{k}|}\ln\left(\frac{b+2|\mathbf{p}\,\|\,\mathbf{k}|}{b-2|\mathbf{p}\,\|\,\mathbf{k}|}\right),\end{aligned}$$

where

$$a^{\mu\nu}=2p^\mu(p^\nu+k^\nu)+2p^\nu(p^\mu+k^\mu)-2p^0(p^0+k^0)g^{\mu\nu}+2|\mathbf{p}|^2g^{\mu\nu}.$$

Evaluating the integrals in p^0 by closing the contours at infinity gives

$$\begin{aligned}\Pi_{LL,+}^{\mu\nu} &= -2\int_0^\infty\frac{d|\mathbf{p}\,\|\,\mathbf{p}|^2}{(2\pi)^2}\frac{\tilde{f}(E_\mathbf{p}-\mu)+\tilde{f}(E_\mathbf{p}+\mu)}{E_\mathbf{p}}\,\mathrm{Re}\left[\frac{a^{\mu\nu}+bg^{\mu\nu}}{4|\mathbf{p}\,\|\,\mathbf{k}|}\ln\left(\frac{b+2|\mathbf{p}\,\|\,\mathbf{k}|}{b-2|\mathbf{p}\,\|\,\mathbf{k}|}\right)-g^{\mu\nu}\right]_{p^0=E_\mathbf{p}},\\ \Pi_{LR,+}^{\mu\nu} &= -2\int_0^\infty\frac{d|\mathbf{p}\,\|\,\mathbf{p}|^2}{(2\pi)^2}\frac{\tilde{f}(E_\mathbf{p}-\mu)+\tilde{f}(E_\mathbf{p}+\mu)}{E_\mathbf{p}}\,\mathrm{Re}\left[\frac{N_{LR}^{\mu\nu}}{4|\mathbf{p}\,\|\,\mathbf{k}|}\ln\left(\frac{b+2|\mathbf{p}\,\|\,\mathbf{k}|}{b-2|\mathbf{p}\,\|\,\mathbf{k}|}\right)\right]_{p^0=E_\mathbf{p}}.\end{aligned}$$

In the above expression we have

$$\mathrm{Re}\,f(k^0)=\frac{1}{2}[f(k^0)+f(-k^0)],\qquad E_\mathbf{p}=\sqrt{|\mathbf{p}|^2+m^2}.$$

The computation was performed in the case where no poles reside in the interior of C. However it is straightforward to verify that this result holds also if some of the poles are located inside the contour C.

We are now ready to piece together the S-parameter from (B1) and the definition in Eqs. (3) and (5). We first write the expression for $\Pi_{3Y,+}$:

$$\begin{aligned}&\Pi_{3Y,+}^{\mu\nu}(k^0,\mathbf{k},m_u,m_d)\\ &\quad=\frac{y}{2}\,\mathrm{Re}\int_0^\infty\frac{d|\mathbf{p}\,\|\,\mathbf{p}|^2}{(2\pi)^2}\left\{\frac{\tilde{f}(E_{\mathbf{p},d}-\mu)+\tilde{f}(E_{\mathbf{p},d}+\mu)}{E_{\mathbf{p},d}}\cdot\left[\frac{a^{\mu\nu}+b_dg^{\mu\nu}+(1-\frac{1}{y})N_{LR,d}^{\mu\nu}}{4|\mathbf{p}\,\|\,\mathbf{k}|}\ln\left(\frac{b_d+2|\mathbf{p}\,\|\,\mathbf{k}|}{b_d-2|\mathbf{p}\,\|\,\mathbf{k}|}\right)-g^{\mu\nu}\right]_{p^0=E_{\mathbf{p},d}}\right.\\ &\quad\left.-\frac{\tilde{f}(E_{\mathbf{p},u}-\mu)+\tilde{f}(E_{\mathbf{p},u}+\mu)}{E_{\mathbf{p},u}}\cdot\left[\frac{a^{\mu\nu}+b_ug^{\mu\nu}+(1+\frac{1}{y})N_{LR,u}^{\mu\nu}}{4|\mathbf{p}\,\|\,\mathbf{k}|}\ln\left(\frac{b_u+2|\mathbf{p}\,\|\,\mathbf{k}|}{b_u-2|\mathbf{p}\,\|\,\mathbf{k}|}\right)-g^{\mu\nu}\right]_{p^0=E_{\mathbf{p},u}}\right\},\end{aligned}$$

where the subscript u, d denotes which mass is used. To write down the explicit expression for the S-parameter in Eq. (3), we now take the limit $k\longrightarrow 0$ keeping $k^0=\cosh(\eta)k$, $|\mathbf{k}|=\sinh(\eta)k$:

$$\begin{aligned}&\lim_{k\to 0}\Pi_{3Y,+}^{\mu\nu}(\cosh(\eta)k,\sinh(\eta)k,m_u,m_d)\\ &\quad=\frac{y}{4}\int_0^\infty\frac{d|\mathbf{p}\,\|\,\mathbf{p}|^2}{(2\pi)^2}\left\{\frac{\tilde{f}(E_{\mathbf{p},d}-\mu)+\tilde{f}(E_{\mathbf{p},d}+\mu)}{E_{\mathbf{p},d}}\cdot\left[\frac{a^{\mu\nu}+(1-\frac{1}{y})N_{LR,d}^{\mu\nu}}{-2(m^2\cosh^2(\eta)+p^2)}-g^{\mu\nu}\right]_{p^0=E_{\mathbf{p},d},k=0}\right.\\ &\quad\left.-\frac{\tilde{f}(E_{\mathbf{p},u}-\mu)+\tilde{f}(E_{\mathbf{p},u}+\mu)}{E_{\mathbf{p},u}}\cdot\left[\frac{a^{\mu\nu}+(1+\frac{1}{y})N_{LR,u}^{\mu\nu}}{-2(m^2\cosh^2(\eta)+p^2)}-g^{\mu\nu}\right]_{p^0=E_{\mathbf{p},u},k=0}\right\}.\end{aligned}$$

The plasma contribution to the S-parameter S_+ can be computed from the explicit expressions for $\Pi_{3Y,+}$ and $\lim_{k\to 0}\Pi_{3Y,+}$ above

$$S_+(k^2, x, m_u, m_d) = -16\pi \frac{\Pi_{3Y,+} - \lim_{k\to 0}\Pi_{3Y,+}}{k^2},$$

where $x = \coth(\eta)$ and $\Pi_{3Y,+}$ is the coefficient of the $g^{\mu\nu}$ part of $\Pi^{\mu\nu}_{3Y,+}$.

[1] D. C. Kennedy and B. W. Lynn, Nucl. Phys. **B322**, 1 (1989); **B321**, 83 (1989).

[2] M. E. Peskin and T. Takeuchi, Phys. Rev. Lett. **65**, 964 (1990).

[3] M. E. Peskin and T. Takeuchi, Phys. Rev. D **46**, 381 (1992).

[4] G. Altarelli and R. Barbieri, Phys. Lett. B **253**, 161 (1991).

[5] T. Appelquist and F. Sannino, Phys. Rev. D **59**, 067702 (1999).

[6] M. Kurachi and R. Shrock, Phys. Rev. D **74**, 056003 (2006).

[7] M. Kurachi and R. Shrock, J. High Energy Phys. 12 (2006) 034.

[8] R. Sundrum and S. D. H. Hsu, Nucl. Phys. **B391**, 127 (1993).

[9] D. K. Hong and H. U. Yee, Phys. Rev. D **74**, 015011 (2006).

[10] J. Hirn and V. Sanz, Phys. Rev. Lett. **97**, 121803 (2006).

[11] K. Agashe, C. Csaki, C. Grojean, and M. Reece, J. High Energy Phys. 12 (2007) 003.

[12] F. Sannino, Phys. Rev. D **82**, 081701 (2010).

[13] F. Sannino, Phys. Rev. Lett. **105**, 232002 (2010).

[14] S. Di Chiara, C. Pica, and F. Sannino, Phys. Lett. B **700**, 229 (2011).

[15] M. Round, Phys. Rev. D **84**, 013012 (2011).

[16] D. D. Dietrich and C. Kouvaris, Phys. Rev. D **79**, 075004 (2009).

[17] L. Anguelova, P. Suranyi, and L. C. R. Wijewardhana, Nucl. Phys. **B852**, 39 (2011).

[18] E. Shintani *et al.* (JLQCD Collaboration), Phys. Rev. Lett. **101**, 242001 (2008).

[19] P. A. Boyle, L. Del Debbio, J. Wennekers, and J. M. Zanotti (RBC Collaborations and UKQCD Collaborations), Phys. Rev. D **81**, 014504 (2010).

[20] H. J. He, N. Polonsky, and S. f. Su, Phys. Rev. D **64**, 053004 (2001).

[21] J. I. Kapusta and C. Gale, *Finite Temperature Field Theory* (Cambridge University Press, Cambridge, UK, 2006), p. 428.

[22] T. Appelquist *et al.* (LSD Collaboration), Phys. Rev. Lett. **106**, 231601 (2011).

[23] T. DeGrand, arXiv:1006.3777.

[24] A. Djouadi and P. Gambino, Phys. Rev. D **49**, 3499 (1994).**53**, 4111(E) (1996).

[25] M. E. Peskin and D. V. Schroeder, *Reading* (Addison-Wesley, USA, 1995), p. 842.

PHYSICAL REVIEW D **87,** 034508 (2013)

Orthogonal technicolor with isotriplet dark matter on the lattice

Ari Hietanen,[*] Claudio Pica,[†] Francesco Sannino,[‡] and Ulrik Ishøj Søndergaard[§]
CP^3-Origins and the Danish Institute for Advanced Study DIAS, University of Southern Denmark,
Campusvej 55, DK-5230 Odense M, Denmark
(Received 6 December 2012; published 13 February 2013)

We study the gauge dynamics of an SO(4)-gauge theory with two Dirac Wilson fermions transforming according to the vector representation of the gauge group. We determine the lattice phase diagram by locating the strong coupling bulk phase transition line and the zero quark mass line. We present results for the spectrum of the theory obtained at a fixed value of the lattice spacing. In particular we measure the pseudoscalar, vector and axial meson masses. The data are consistent with a chiral symmetry breaking scenario rather than a conformal one. When used to break the electroweak symmetry dynamically the model leads to a natural dark matter candidate.

DOI: 10.1103/PhysRevD.87.034508 PACS numbers: 11.15.Ha, 11.30.Rd

I. INTRODUCTION

Understanding the phase diagram of strongly interacting theories will unveil a large number of theories of fundamental interactions useful to describe electroweak symmetry breaking, dark matter and even inflation [1–4]. To gain a coherent understanding of strong dynamics besides the SU(N) gauge groups [5,6], one should also investigate the orthogonal, symplectic and exceptional groups. SO(N) and SP(2N) phase diagrams were investigated with analytic methods in Ref. [7], while the exceptional ones together with orthogonal gauge groups featuring spinorial matter representationswere studied in Ref. [8]. So far lattice simulations have been mostly employed to explore the phase diagram of SU(N) gauge theories while a systematic lattice analysis of the smallest symplectic group was launched in Ref. [9].

Here we move forward by analyzing on the lattice the dynamics of the SO(4) gauge group with two Dirac fermions in the vector representation of the group. This choice is based on the following theoretical and phenomenological considerations. The theory is expected to be below or near the lower boundary of the conformal window [7,10], and therefore break chiral symmetry. The theory can be used as a technicolor [11,12] template similar, from the global symmetry point of view, to minimal walking technicolor (MWT) [5,13,14].

Although the chiral symmetry breaking pattern is identical to the one of MWT there are substantial differences in the massive spectrum of the theory with important phenomenological consequences. This is because for MWT the technifermions, like the technigluons, transform according to the adjoint representation of the underlying gauge group. Consequently, one can immediately construct technicolor gauge singlets, which are made from one technifermion and one techniglue. This forces model builders to choose nonstandard model hypercharge assignments for the technifermions in order to make sure that the composite fermonic states have integer electric charges. Furthermore, the Witten anomaly [15] of MWT is resolved by adding new leptonlike fermions that are doubly charged because of the hypercharge choice with interesting phenomenology. The theory we investigate here has the following features: Being an SO(4) gauge theory it has an even number of technifermions gauged under the electroweak avoiding the Witten anomaly; the technigluons belong to the two-index antisymmetric representation [the adjoint of SO(4)] while the technifermions to the vector representation, therefore forbidding the construction of a technifermion-technigluon bound state. These features renders *orthogonal technicolor* a simpler model than MWT.

Furthermore the orthogonal technicolor theory leads to a weak isotriplet with the neutral member being an ideal dark matter candidate [7,10], the isotriplet technicolor interactive massive particle (iTIMP). This state is a pseudo Goldstone and therefore can be light with respect to the electroweak scale making it a natural candidate to resolve some of the current experimental puzzles [10,16]. The first model featuring composite dark matter pions appeared in Refs. [17,18] and the first study of technipion dark matter on a lattice appeared in Ref. [9].

Due to the reality of the fermion representation the quantum global symmetry group is SU(4) expected to break spontaneously to SO(4), yielding nine Goldstone bosons. Once gauged under the electroweak theory three are eaten by the SM gauge bosons. Six additional Goldstone bosons form an electroweak complex triplet of technibaryon with the neutral isospin zero component to be identified with the iTIMP of Ref. [10].

SO(4) is a semisimple group, SO(4) ≅ SU(2) ⊗ SO(3), and it has a nontrivial center Z_2. The theory is asymptotically free and since the two-loop β-function for different number of flavors loses the infrared zero for $N_f = 2.3$

---

[*] hietanen@cp3-origins.net
[†] pica@cp3-origins.net
[‡] sannino@cp3.dias.sdu.dk
[§] sondergaard@cp3.sdu.dk

while the all-orders beta function [19,20] predicts the anomalous dimension of the mass to be unity for $N_f = 2.86$ we expect that chiral symmetry breaks for two Dirac flavors. However, we want to confirm here this result via first principle lattice simulations. Furthermore, there is also the possibility that the theory shows a certain degree of walking [9,10,21–23] unless the phase transition is of jumping type [24,25]. Jumping conformal phase transitions have been demonstrated to occur in a wide class of theories [26].

As a natural first step, we study the phase diagram in the (β, m_0)-plane to find the relevant region of parameter space to simulate. We then determine the zero partial conservation of the axial current (PCAC) mass line as well as the strong coupling bulk phase transition line. In addition, we report on the pseudoscalar, vector and axial vector meson masses. From the measured spectrum we infer that the theory breaks chiral symmetry dynamically. Part of these results appeared in Ref. [27].

In Sec. II we present the analytic expectations for the phase diagram of SO(N) as a function of the number of flavors. We also summarize the expected breaking pattern of the quantum global symmetries for theories below the conformal window. We also prove the spectral degeneracy between certain diquarks and ordinary mesonlike states. In Sec. III we recall the lattice formulation of the theory and summarize the physical observable studied here. The results of the simulations are reported in Sec. IV and conclude in Sec. V.

II. ORTHOGONAL CONFORMAL WINDOW AND CHIRAL SYMMETRY BREAKING PATTERN

The two loop β-function for an SO(N) theory with N_{f} Dirac fermions transforming according to the vector representation of the gauge group is

$$\beta(\alpha) = -\frac{\alpha^2}{2\pi}\left(b_0 + b_1\frac{\alpha}{2\pi}\right), \tag{1}$$

where

$$\begin{aligned} b_0 &= \frac{11}{3}N_{\mathrm{c}} - \frac{4}{3}N_{\mathrm{f}} - \frac{22}{3}, \\ b_1 &= -\frac{10}{3}(N_{\mathrm{c}}-2)N_{\mathrm{f}} - (N_{\mathrm{c}}-1)N_{\mathrm{f}} + \frac{17}{3}(N_{\mathrm{c}}-2)^2. \end{aligned} \tag{2}$$

A naive estimate of the lower bound of conformal window is given when the second coefficient b_1 changes sign. For SO(4) this happens when $N_f = \frac{68}{29} \simeq 2.3$. The corresponding values for three and four-loops in the $\overline{\mathrm{MS}}$-scheme are $N_f = 1.8$ and $N_f = 3.0$. The all-orders beta function predicts as lower boundary $N_f = 2.86$, see Fig. 1. Hence, perturbative and nonperturbative methods suggest that chiral symmetry breaks for two Dirac flavors. However, lattice simulations can seal this expectation. Since the vector representations of orthogonal groups are real the quantum global symmetry of the theory is, for a generic N_f SU($2N_{\mathrm{f}}$) which is larger than $\mathrm{SU}(N)_{\mathrm{f}}) \otimes \mathrm{SU}(N_{\mathrm{f}}) \otimes \mathrm{U}_V(1)$ valid for complex fermion representations. The reality property of the representation translates in the following property of the Dirac operator

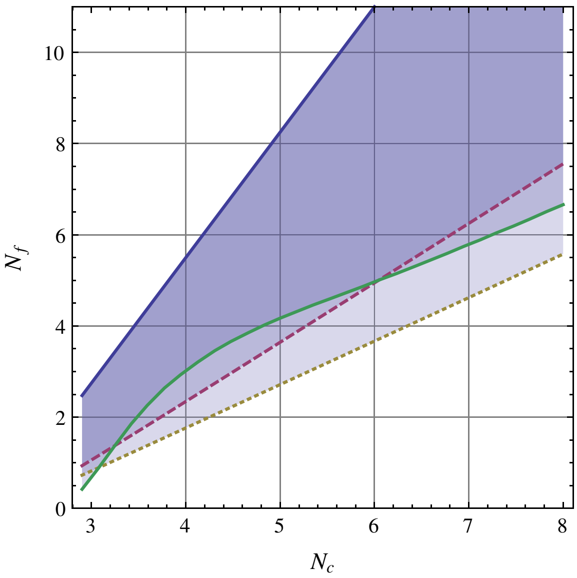

FIG. 1 (color online). Conformal window of SO(N_{c}) with N_{f} Dirac fermions in the fundamental representation. Upper bound is when asymptotic freedom is lost. Lower bounds are 2-loop (red, dashed), 3-loop (yellow, dotted) and 4-loop estimates (green, solid).

$$(\not{D} + m)C\gamma^5 = C\gamma^5(\not{D} + m)^*, \tag{3}$$

where $\not{D} = \gamma^\mu(\partial_\mu - igA^a_\mu\tau_a)$, $a = 1, \ldots, d[G]$ where $d[G]$ is the dimension of the adjoint representation of the gauge group and $C = i\gamma^0\gamma^2$ is the charge conjugation operator.

The global SU($2N_{\mathrm{f}}$) is assumed to break to the maximal diagonal subgroup

$$\mathrm{SU}(2N_{\mathrm{f}}) \longrightarrow \mathrm{SO}(2N_{\mathrm{f}}), \tag{4}$$

for the massless theory and for N_f below the conformal window. A common mass for the Dirac fermions leads to the same pattern of explicit symmetry breaking. The explicit interpolating operators for the Goldstones can be naturally divided in three independent antifermion-fermion bilinears

$$\bar{\psi}_f\gamma^5\psi_{f'}, \tag{5}$$

with f and f' the flavor indices $f = 1, 2$ and six *difermion* operators

$$\psi^T_f C\gamma^5\psi_{f'} \quad \text{and} \quad \bar{\psi}_f\gamma^5 C\bar{\psi}^T_{f'}. \tag{6}$$

The reader can find a useful summary of the global symmetry breaking patterns tailored for lattice computations in

Ref. [28], while applications to beyond standard model physics for similar patterns appeared in Refs. [17,29]. Notice that whereas the usual pions have odd parity, the corresponding diquarks are parity even. It was noticed in Ref. [9] that when fermions are in a pseudoreal representation, the diquark correlator is exactly identical to the corresponding mesonic correlator. In the Appendix we give a similar proof for fermions in real representations. The proof uses the symmetry (3) of the Dirac operator along with the γ^5-hermiticity $\gamma^5(\not{D}+m)\gamma^5 = (\not{D}+m)^\dagger$ property. The result can be stated as

$$c^{(\Gamma)}_{\bar\psi_f\bar\psi_{f'}}(x-y) = c^{(\Gamma)}_{\bar\psi_f\psi_{f'}}(x-y) = c^{(\Gamma)}_{\psi_f\psi_{f'}}(x-y), \qquad (7)$$

where $c^{(\Gamma)}_{\bar\psi_f\psi_{f'}}$ is the correlator for the operator $\bar\psi_f\Gamma\psi_{f'}$ and $c^{(\Gamma)}_{\psi_f\psi_{f'}}$ is the correlator for the corresponding diquark operator $\psi_f^T\Gamma C\psi_{f'}$. Γ can be any of the matrices $\mathbf{1}$, γ^5, γ^μ, $\gamma^\mu\gamma^5$.

Having discussed the generic features expected for orthogonal groups we now turn to the lattice formulation and results for the relevant case of SO(4) with two Dirac flavors.

III. LATTICE FORMULATION

In this work we have used the Wilson prescription for the lattice action

$$S = S_{\mathrm{F}} + S_{\mathrm{G}}, \qquad (8)$$

where

$$S_{\mathrm{G}} = \beta\sum_x \sum_{\mu,\nu<\mu}\left[1 - \frac{1}{N_{\mathrm{c}}}\mathrm{Tr}\,\mathcal{U}_{\mu\nu}(x)\right], \qquad (9)$$

is the Yang-Mills gauge action. We have normalized the lattice spacing to $a = 1$. $\mathcal{U}_{\mu\nu}(x)$ is the plaquette defined in terms of the link variables as

$$\mathcal{U}_{\mu\nu}(x) = \mathcal{U}_\mu(x)\mathcal{U}_\nu(x+\hat\mu)\mathcal{U}^T_\mu(x+\hat\mu+\hat\nu)\mathcal{U}^T_\nu(x+\hat\nu). \qquad (10)$$

The Wilson fermion action is

$$S_{\mathrm{F}} = \sum_f\sum_{x,y}\bar\psi_f(x)M(x,y)\psi_f(y), \qquad (11)$$

with f running over fermion flavors and the Wilson-Dirac matrix $M(x,y)$ given by

$$\begin{aligned}\sum_y M(x,y)\psi(y) = {}& (4+m_0)\psi(x) \\ & -\frac{1}{2}\sum_\mu\Big[(1+\gamma_\mu)\mathcal{U}^T_\mu(x-\hat\mu)\psi(x-\hat\mu) \\ & + (1-\gamma_\mu)\mathcal{U}_\mu(x)\psi(x+\hat\mu)\Big]. \end{aligned} \qquad (12)$$

Here the gauge and spinor indices have been suppressed. The bare parameters are the inverse of the bare coupling $\beta = 2N_{\mathrm{c}}/g_0^2$ appearing in the gauge action and the bare mass m_0 of the Wilson fermions.

We employ the PCAC relation to define the physical quark mass

$$m_{\mathrm{PCAC}} = \lim_{t\to\infty}\frac{1}{2}\frac{\partial_t V_{\mathrm{PS}}}{V_{\mathrm{PP}}}, \qquad (13)$$

where the currents are

$$\begin{aligned} V_{\mathrm{PS}}(x_0) &= a^3\sum_{x_1,x_2,x_3}\langle\bar\psi_1(x)\gamma_0\gamma_5\psi_2(x)\bar\psi_1(0)\gamma_5\psi_2(0)\rangle, \\ V_{\mathrm{PP}}(x_0) &= a^3\sum_{x_1,x_2,x_3}\langle\bar\psi_1(x)\gamma_5\psi_2(x)\bar\psi_1(0)\gamma_5\psi_2(0)\rangle. \end{aligned} \qquad (14)$$

The meson masses are estimated using time slice averaged zero momentum correlators

$$C^{(\Gamma)}_{\bar\psi_1\psi_2}(x_0) = a^3\sum_{x_1,x_2,x_3}\mathrm{Tr}([\bar\psi_1(x)\Gamma\psi_2(x)]^\dagger\bar\psi_1(0)\Gamma\psi_2(0)), \qquad (15)$$

where $\Gamma = \gamma_5$ for pseudoscalar, $\Gamma = \gamma_k$ ($k = 1, 2,3$) for vector, and $\gamma_5\gamma_k$ for axial vector meson.

IV. RESULTS

The simulations were performed on three different lattices $8^3\times 16$, $12^3\times 64$ and $24^3\times 64$ where in all cases the larger dimension is the temporal one. All the simulations were started from a random configuration and the first 500–2000 iterations were discarded. This is enough to thermalize the system for the quantities we measured. For a complete list of the simulations see Table I where we have omitted the values of the bare masses.

The smallest lattice was used for exploration of the parameter space spanned by the bare mass m_0 and the coupling β. Figure 2 shows an outline of the lattice phase structure measured on this $8^3\times 16$ lattice. For small values of β the system is in a bulk phase not connected to continuum physics. The bulk phase is separated from the small coupling (large β) phase by a first order phase transition. Figure 3 shows the discontinuous behavior of

TABLE I. Simulation parameters and thermalization times. For each coupling we performed multiple simulations with appropriate bare masses. The thermalization column refers to the number of discarded initial configurations.

Volume	β	Iterations	Thermalization
$8^3\times 16$	4.1, 4.2, ..., 4.9, 5.2, 5.4, 5.6	2000	500
	44.55, 5.5, 6, 7	5000	2000
$12^3\times 64$	5.5, 7	5000	1500
$24^3\times 64$	7	850–2000	600

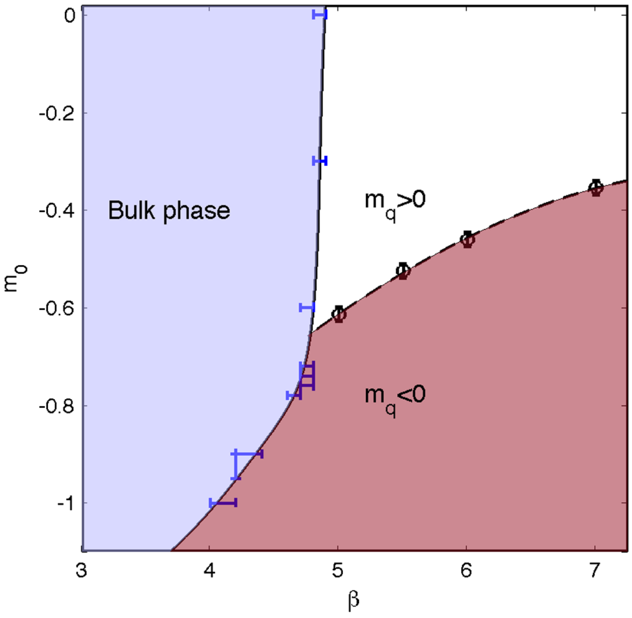

FIG. 2 (color online). Lattice phase structure outlined on an $8^3 \times 16$ lattice. Circles represent points of critical bare mass where $m_{\mathrm{PCAC}} = 0$. The transition between the bulk phase is of first order. The error bars represent the interval over which the measured average plaquette jumps.

the average plaquette when crossing the bulk phase transition, for three different values of m_0. The uncertainty on the location of the bulk phase transition shown in Fig. 2 is due to taking discrete values of β between simulation points.

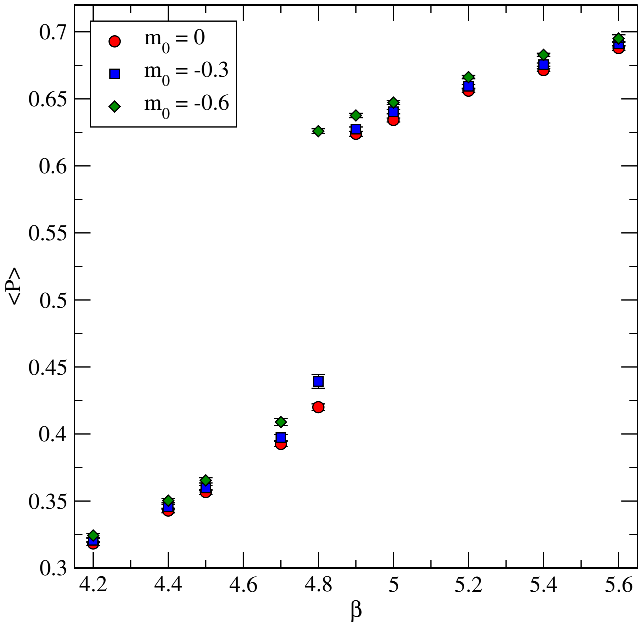

FIG. 3 (color online). Average plaquette $\langle P \rangle$ vs β on an $8^3 \times 16$ lattice at three different values of the bare mass.

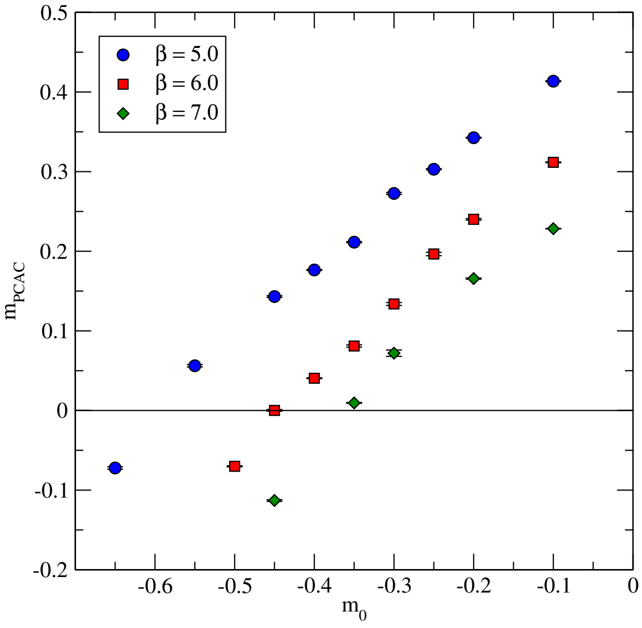

FIG. 4 (color online). m_{PCAC} in units of inverse lattice spacing at three different couplings. The measurements are performed on a $8^3 \times 16$.

We can compare our result for the location of the bulk transition to previous studies of SO(N) pure gauge theories. Earlier simulations focused mainly on the SO(3) gauge group [30] with the exception of Ref. [31] where also other values of N were considered. For SO(4) the authors of Ref. [31] find that the bulk phase transition happens for $4.62(3) < \beta < 4.87(3)$, which is in agreement with our result in Fig. 3.

The critical line where the physical quark mass vanishes is determined from the PCAC relation (13). The critical line of $m_q = 0$ in the phase diagram (Fig. 2) is constructed by linear fits to the PCAC mass. Figure 4 shows the bare mass dependency of the PCAC mass at three different couplings on the $8^3 \times 16$ lattice.

A. Finite size effects

According to the perturbative estimates discussed in Sec. II the running of the gauge coupling is expected to be slow. This also suggests that attention should be paid to finite size effects, which need to be estimated nonperturbatively by measuring physical observables as a function of lattice size.

In the case of SO(N) pure gauge theories [30,31] the bulk phase transition occurs at such a weak coupling that extremely large lattices are required for simulations in the confined phase, the one connected to the continuum physics. However, in the presence of dynamical quarks, we find that somewhat smaller volumes ($24^3 \times 64$) are enough to probe the chiral regime of the system.

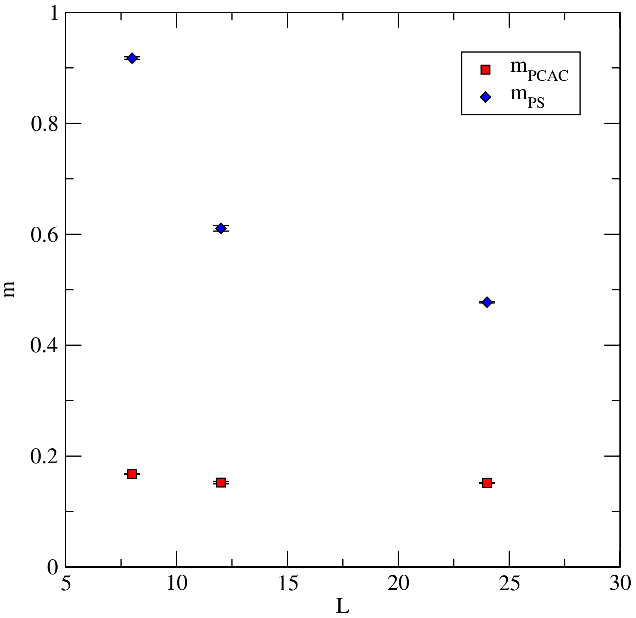

FIG. 5 (color online). Finite size effects on m_{PS} and m_{PCAC} in units of inverse lattice spacing. The measurements are performed on a $24^3 \times 64$ lattice at $\beta = 7$ and $m_0 = -0.2$.

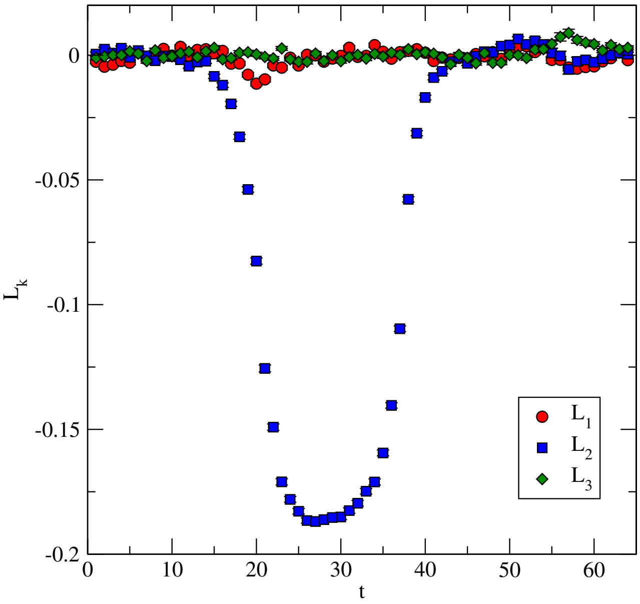

FIG. 6 (color online). Average Polyakov loops wound around the three spatial dimensions computed at each time slice of the lattice. This measurement was performed on a $12^3 \times 64$ lattice at $\beta = 7$ and $m_0 = -0.3$. The values are averages over 700 configurations starting at 1800 where the system does not appear to thermalize further.

In Fig. 5 the mass of the pseudoscalar meson m_{PS} and the PCAC quark mass m_{PCAC} is plotted for different lattice sizes. The PCAC mass has little dependence on the lattice size being a UV quantity. The pseudoscalar meson mass, on the contrary, is very sensitive to finite size effects even if it is still somewhat heavy at the bare mass used in Fig. 5.

Another interesting property which seems to occur at small volumes is a phase separation characterized by the existence of domain walls. As explained below, this would be different from what happens in simulations of SU(N) gauge models in the so-called femto-world regime [32–34].

We observe the coexistence, inside the same 4-volume, of two distinct phases which can be characterized by the spatial average of Polyakov loops wrapping around the three spatial directions taken on each time slice separately. In detail, the operators we consider are defined as

$$L_k(t) = \left\langle \frac{1}{N_i N_j} \sum_{x_i, x_j} \frac{1}{N} \mathrm{Tr} \prod_{x_k} \mathcal{U}_k(t, \mathbf{x}) \right\rangle, \qquad (16)$$

where $i \neq j \neq k$ are spatial directions. The two phases are separated by domain walls which are stable for the whole length of our simulations, of the order of ~5000 hybrid Monte Carlo updates. As an illustration of this phenomenon, Fig. 6 shows the time resolved Polyakov loops on a $12^3 \times 64$ lattice at $\beta = 7$ and $m_0 = -0.3$. Given that the two phases are long-lived and do not move inside the 4-volume of the lattice during the simulation, we show the average of the time-resolved Polyakov loops over 700 consecutive, thermalized configurations. The coexistence of two phases with different values of L_2 is clear from the figure. The phenomenon appears in all simulations performed on small lattices. The location of the phase boundaries and the direction in which the Polyakov loop has nonzero average is random. In some cases more than two phase boundaries appear in the same system. Notice also that in one of the two phases the average value of the Polyakov loop vanishes.

The behavior just described for this model is in contrast with what is normally observed in simulations done with SU(N) gauge groups in a small boxes. In the so-called femto-world regime of SU(N) gauge theories, one also expects the Polyakov loops to spontaneously generate a nonvanishing expectation value, but stable domain walls inside the lattice volume are not observed.

The coexistence of two phases is also reflected in an anomalous behavior of mesonic correlators measured for volumes smaller than $24^3 \times 64$. An example is shown in Fig. 7 where the effective mass plateaux of the pseudoscalar meson shows a visible rise at large separations, consistent with the two phases having different pseudoscalar correlation lengths.

In order to understand whether these phase separations are related to the presence of dynamical fermions we have also performed pure gauge simulations on $12^3 \times 64$ lattices. The phase separation occurs also for the pure gauge. Thus the phenomenon seems to be a feature stemming from the pure gauge sector.

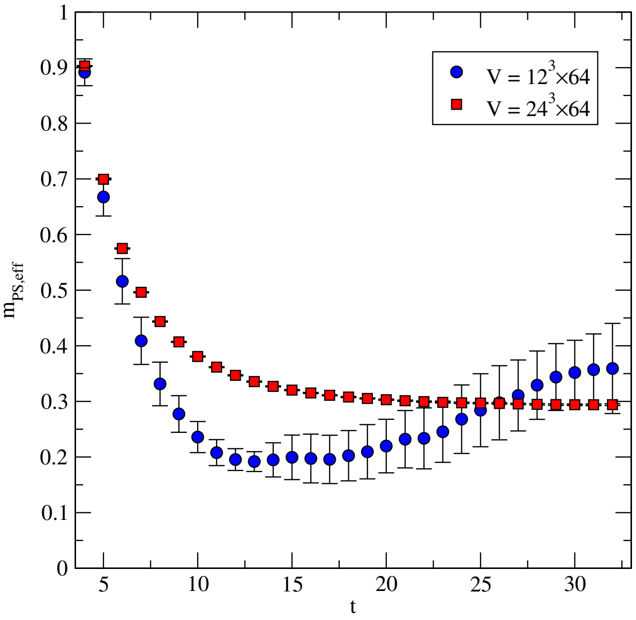

FIG. 7 (color online). Effective mass of pseudoscalar meson for two different volumes.

We will not explore this feature further in this work, but it would be interesting to continue its investigation in the future.

In order to avoid the complications stemming from the phase separation described above we use $24^3 \times 64$ lattices for the rest of the paper.

B. Spectrum and chiral symmetry breaking

We address the dynamical fate of the chiral symmetries of the theory by determining the pseudoscalars and (axial) vectors spectrum.

Figure 8 shows the pseudoscalar, vector, and axial vector meson masses measured on a $24^3 \times 64$ lattice at $\beta = 7$ as the bare quark mass is decreased towards the critical value. At the lightest quark mass the pseudoscalar meson has a mass of about $m_{\mathrm{PS}} \simeq 0.15$ in lattice units corresponding to about $m_{\mathrm{PS}}L \simeq 3.6$. Since two of the three volumes used in this study are affected by the presence of the phase separation phenomenon discussed above, it is difficult to estimate the finite volume effect on the light states. However, we will take the values of the pseudoscalar and vector masses obtained here as reasonable first estimates and leave a more systematic investigation of the finite volume effects for the future. The reader should also be aware that in previous studies of non-QCD models such as the so-called sextet model [35] or MWT [36] it was found that larger values of $m_{\mathrm{PS}}L$ than in QCD are needed to accurately measure the light states.

At large quark masses the vector and pseudoscalar are degenerate with the common mass increasing linearly with the quark mass. At smaller masses the vector meson becomes heavier than the pseudosclar. This is consistent with dynamical generation of a chiral scale. To see this more clearly the ratio of the vector and the pseudoscalar masses have been plotted in Fig. 9. Indeed the mass ratio approaches unity for large quark masses. However, when approaching the chiral limit the ratio increases signaling chiral symmetry breaking. In fact this result is consistent with the expectation that if spontaneous

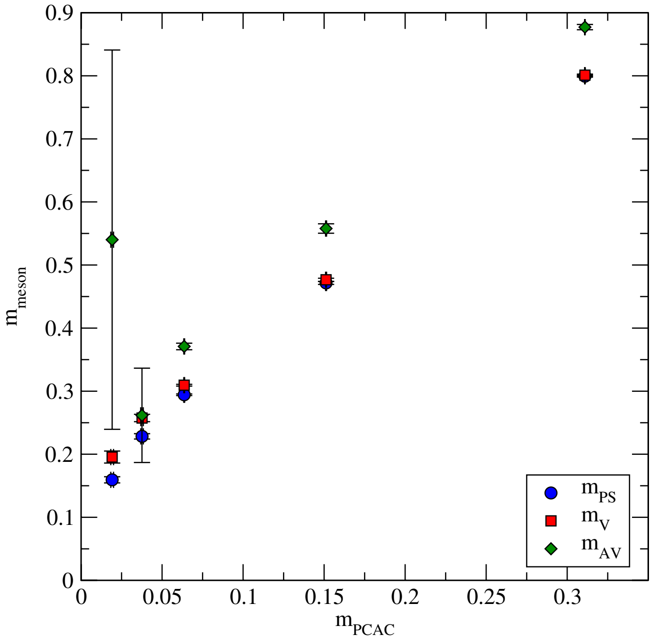

FIG. 8 (color online). Pseudoscalar, vector, and axial vector meson masses measured on a $24^3 \times 64$ lattice at $\beta = 7$.

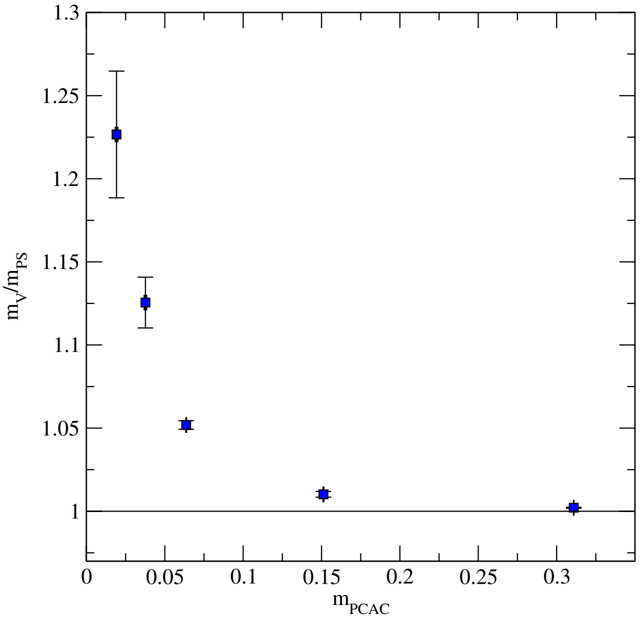

FIG. 9 (color online). Ratio between pseudoscalar and vector meson masses measured on a $24^3 \times 64$ lattice at $\beta = 7$.

symmetry breaking occurs, the vector meson remains massive whereas the pseudoscalar meson is massless. A diverging ratio m_V/m_{PS} therefore indicates chiral symmetry breaking. This is the trend we observe in Fig. 9. However to nail this conclusion more studies have to be performed.

The axial mass in the chiral limit is poorly determined Fig. 8. In the future we plan on improving its determination. We will then be able to use it to infer interesting properties of the chiral transition. For example one can investigate whether the axial remains (near) degenerate with the vector in the chiral regime which could signify the onset of walking dynamics [29,37].

To extract further properties of the theory we analyze in more detail the functional dependence of the pseudocalar mass on the quark mass. It is well known that, for these kinds of theories, spontaneously broken chiral symmetry leads to the Gell-Mann-Oakes-Renner relation [38]

$$m_{PS}^2 \simeq \Lambda m_{PCAC}, \tag{17}$$

valid in the chiral limit, where $\Lambda = -2\langle\bar{\psi}\psi\rangle/f_{PS}^2$ is a dynamically generated scale. For conformal theories the behavior is different [39,40]. In Ref. [40] it was also shown that the instanton contributions to conformal chiral dynamics can be neglected when the anomalous dimension of the mass operator is less than one. This property has been investigated and confirmed via lattice simulations in Ref. [41]. A clever separation of the ultraviolet and infrared modes presented in Refs. [42,43] led to a better understanding of the conformal chiral scenario but without discussing the instanton contributions [40]. Building upon these results, an interesting method to determine the anomalous dimension of the fermion masses was put forward in Ref. [44]. To sum up, for a conformal scenario the dynamical scale Λ mutates into a fermion-mass dependent quantity [40] and therefore m_{PS}^2 must vanish as m_{PCAC}^2. In Fig. 10 we plot the ratio m_{PS}^2/m_{PCAC} for decreasing fermion mass. We see that the ratio approaches a constant for vanishing fermion masses which is consistent with the chiral symmetry breaking scenario (17).

TABLE II. Different types of fit functions in the chiral regime for the data with m identified with the m_{PCAC}.

Meson fit	Fit function	Best parameter	χ^2/dof
ps chiral	$a\sqrt{m}$	$a = 1.167(6)$	0.43/2
ps conformal	am	$a = 4.69(3)$	364/2
ps alternative 1	$a + bm$	$a = 0.111(6)$ $b = 2.9(1)$	6.4/1
ps alternative 2	$a + b\sqrt{m}$	$a = -0.001(10)$ $b = 1.17(4)$	0.41/1
Vector chiral	$a + bm$	$a = 0.16(1)$ $b = 2.3(2)$	3.3/1
Vector conformal	am	$a = 4.91(3)$	273/2
Vector alternative 1	$a\sqrt{m}$	$a = 1.231(6)$	18/2
Vector alternative 2	$a + b\sqrt{m}$	$a = 0.07(2)$ $b = 0.96(7)$	0.69/1

In Table II we report the fit to the data for the dependence of the pseudoscalar mass as well as the vector mass as a function of the m_{PCAC} within the believed chiral regime of the theory. This corresponds to the three lowest values of m_{PCAC} where the ratio m_{PS}^2/m_{PCAC} becomes roughly constant as shown in Fig. 10. The data points used for the chiral fits in the table are shown in Fig. 11.

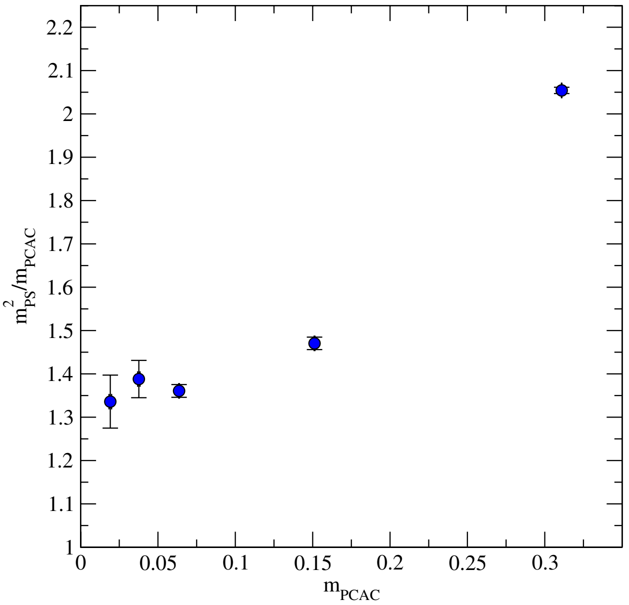

FIG. 10 (color online). Psudoscalar mass squared divided by the quark mass measured on a $24^3 \times 64$ lattice at $\beta = 7$.

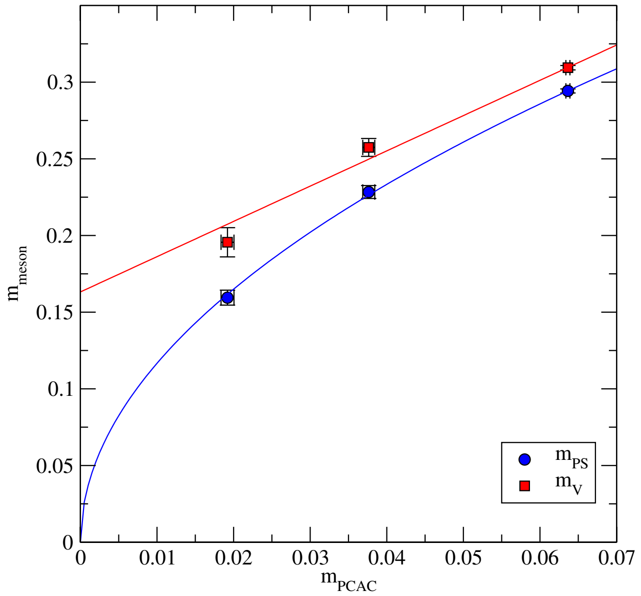

FIG. 11 (color online). The chiral fits to the pseudo scalar and vector meson masses on a $24^3 \times 64$ lattice at $\beta = 7$.

For these three points we have $f_{\mathrm{PS}}L \approx 0.8$–$0.9$. The best fit curve, determined by the lowest χ^2/dof, for the pseudoscalar mass corresponds to the first line of the table which is in agreement with the GMOR expectation. It is remarkable that by even allowing for an offset of the mass value in the chiral limit the best fit demands the offset to vanish, see the last line of the table. We have tried also to test the possibility that the pseudoscalar mass vanishes linearly with the fermion mass and found that this is highly disfavored. If the theory would have been conformal we would have expected this case to fit much better.

Similarly, by fitting the vector masses dependence on the fermion mass, in the lower part of Table II, we observe a reasonable agreement with the expected chiral behavior of the theory. The two best fits correspond to the first and last line of the lower part of the table. We would have expected the first line to yield a better fit if chiral symmetry breaks like in ordinary quantum chromodynamics. We believe that for this case more statistics is needed to resolve which of the two cases is actually realized given that the data cannot yet differentiate between the two. As for the pseudoscalar case the would-be conformal case is highly disfavored (see second line of the lower part of the table).

Using the identity for the hadronic correlators (8) we can immediately infer the baryonic diquark masses.

V. CONCLUSIONS

Orthogonal lattice gauge theories with dynamical fermions have so far been *terra incognita*. However, as explained in the introduction, these theories can be relevant for models of dynamical electroweak symmetry breaking as well as for the construction of interesting dark matter candidates. Furthermore to have a deeper understanding of strong dynamics it is essential to gain information on different gauge theories. We have chosen to start investigating the orthogonal gauge groups dynamics with a phenomenologically relevant example, i.e., the SO(4) gauge theory with two Dirac flavors transforming according to the vector representation of the group.

We have uncovered the lattice phase diagram and shown that there is a novel phase separation phenomenon at small volumes which persists even in the pure gauge case. We have shown that the phase separation can be circumvented and the chiral regime of the theory studied using large but still feasible lattices.

Finally we investigated the spectrum of the theory for the pseudoscalar, vectors and axial vectors. The results for the spectrum are consistent with chiral symmetry breaking and strongly disfavor a conformal behavior. The spectrum was obtained using lattices with a fixed value of the UV cutoff, corresponding to $\beta = 7$. Further investigations will be needed using different values of the cutoff to better address the continuum limit.

APPENDIX: DIQUARK CORRELATORS

A generic mesonic correlator will have the form

$$c^{(\Gamma)}_{\bar{\psi}\psi'}(x-y) = \mathrm{Tr}([\bar{\psi}(x)\Gamma\psi'(x)]^\dagger \bar{\psi}(y)\Gamma\psi'(y)), \quad \text{(A1)}$$

and the baryonic diquark correlator will have the form

$$c^{(\Gamma)}_{\psi\psi'}(x-y) = \mathrm{Tr}([\psi^T(x)C\Gamma\psi'(x)]^\dagger \psi^T(y)C\Gamma\psi'(y)). \quad \text{(A2)}$$

Rewriting the diquark correlator slightly gives

$$\begin{aligned} c^{(\Gamma)}_{\psi\psi'}(x-y) = {} & \mathrm{Tr}(\Gamma\psi'(y)\bar{\psi}'(x)\gamma^0\Gamma^\dagger C^\dagger(\gamma^0)^T \\ & \times[\psi(y)\bar{\psi}(x)]^T C). \end{aligned} \quad \text{(A3)}$$

Now we can invoke two identities

$$(\gamma^\mu)^T = -C\gamma^\mu C^\dagger, \quad \text{(A4)}$$

$$\psi(x)\bar{\psi}(y) = C^\dagger[\psi(y)\bar{\psi}(x)]^T C. \quad \text{(A5)}$$

The latter identity follows from the symmetry of the Dirac matrix given in (3) along with γ^5-hermiticity $\gamma^5(\not{D} + m)\gamma^5 = (\not{D} + m)^\dagger$. The identity (A5) extend to the Wilson lattice formulation of the Dirac matrix. This is demonstrated for pseudoreal representations in the Appendix of Ref. [9]. Invoking the identities in the expression for the diquark correlator (A3) we have

$$\begin{aligned} c^{(\Gamma)}_{\psi\psi'}(x-y) &= \mathrm{Tr}(\Gamma\psi'(y)\bar{\psi}'(x)\gamma^0\Gamma^\dagger\gamma^0\psi(x)\bar{\psi}(y)) \\ &= c^{(\Gamma)}_{\bar{\psi}\psi'}(x-y). \end{aligned} \quad \text{(A6)}$$

A similar derivation holds for the antiparticles leading to the identity (8).

[1] F. Sannino, arXiv:0804.0182.
[2] P. Channuie, J. J. Joergensen, and F. Sannino, J. Cosmol. Astropart. Phys. 05 (2011) 007.
[3] F. Bezrukov, P. Channuie, J. J. Joergensen, and F. Sannino, Phys. Rev. D **86**, 063513 (2012).
[4] P. Channuie, J. J. Joergensen, and F. Sannino, Phys. Rev. D **86**, 125035 (2012).
[5] F. Sannino and K. Tuominen, Phys. Rev. D **71**, 051901 (2005).
[6] D. D. Dietrich and F. Sannino, Phys. Rev. D **75**, 085018 (2007).
[7] F. Sannino, Phys. Rev. D **79**, 096007 (2009).
[8] M. Mojaza, C. Pica, T. A. Ryttov, and F. Sannino, Phys. Rev. D **86**, 076012 (2012).

[9] R. Lewis, C. Pica, and F. Sannino, Phys. Rev. D **85**, 014504 (2012).
[10] M. T. Frandsen and F. Sannino, Phys. Rev. D **81**, 097704 (2010).
[11] S. Weinberg, Phys. Rev. D **19**, 1277 (1979).
[12] L. Susskind, Phys. Rev. D **20**, 2619 (1979).
[13] D. D. Dietrich, F. Sannino, and K. Tuominen, Phys. Rev. D **72**, 055001 (2005).
[14] R. Foadi, M. T. Frandsen, T. A. Ryttov, and F. Sannino, Phys. Rev. D **76**, 055005 (2007).
[15] E. Witten, Phys. Lett. **117B**, 324 (1982).
[16] E. Del Nobile, C. Kouvaris, and F. Sannino, Phys. Rev. D **84**, 027301 (2011).
[17] S. B. Gudnason, C. Kouvaris, and F. Sannino, Phys. Rev. D **73**, 115003 (2006).
[18] T. A. Ryttov and F. Sannino, Phys. Rev. D **78**, 115010 (2008).
[19] T. A. Ryttov and F. Sannino, Phys. Rev. D **78**, 065001 (2008).
[20] C. Pica and F. Sannino, Phys. Rev. D **83**, 116001 (2011).
[21] B. Holdom, Phys. Rev. D **24**, 1441 (1981).
[22] K. Yamawaki, M. Bando, and K. i. Matumoto, Phys. Rev. Lett. **56**, 1335 (1986).
[23] T. W. Appelquist, D. Karabali, and L. C. R. Wijewardhana, Phys. Rev. Lett. **57**, 957 (1986).
[24] F. Sannino, arXiv:1205.4246.
[25] P. de Forcrand, S. Kim, and W. Unger, arXiv:1208.2148.
[26] O. Antipin, M. Mojaza, and F. Sannino, arXiv:1208.0987.
[27] A. Hietanen, C. Pica, F. Sannino, and U. I. Sondergaard, Proc. Sci. LATTICE2012 (2012) 065.
[28] J. B. Kogut, M. A. Stephanov, D. Toublan, J. J. M. Verbaarschot, and A. Zhitnitsky, Nucl. Phys. **B582**, 477 (2000).
[29] T. Appelquist, P. S. Rodrigues da Silva, and F. Sannino, Phys. Rev. D **60**, 116007 (1999).
[30] P. de Forcrand and O. Jahn, Nucl. Phys. **B651**, 125 (2003).
[31] F. Bursa, R. Lau, and M. Teper, arXiv:1208.4547.
[32] M. Luscher, Nucl. Phys. **B219**, 233 (1983).
[33] P. van Baal, Commun. Math. Phys. **94**, 397 (1984).
[34] J. Koller and P. van Baal, Nucl. Phys. **B302**, 1 (1988).
[35] Z. Fodor, K. Holland, J. Kuti, D. Nogradi, and C. Schroeder, arXiv:1103.5998.
[36] A. Patella, L. Del Debbio, B. Lucini, C. Pica, and A. Rago, Proc. Sci. LATTICE2011 (2011) 084.
[37] T. Appelquist and F. Sannino, Phys. Rev. D **59**, 067702 (1999).
[38] M. Gell-Mann, R. J. Oakes, and B. Renner, Phys. Rev. **175**, 2195 (1968).
[39] F. Sannino and R. Zwicky, Phys. Rev. D **79**, 015016 (2009).
[40] F. Sannino, Phys. Rev. D **80**, 017901 (2009).L. Del Debbio, B. Lucini, A. Patella, C. Pica, and A. Rago, Phys. Rev. D **80**, 074507 (2009).
[41] E. Bennett and B. Lucini, arXiv:1209.5579.
[42] L. Del Debbio and R. Zwicky, Phys. Rev. D **82**, 014502 (2010).
[43] L. Del Debbio and R. Zwicky, Phys. Lett. B **700**, 217 (2011).
[44] A. Patella, Phys. Rev. D **84**, 125033 (2011).